

UNCLASSIFIED

AD NUMBER
ADB064202
NEW LIMITATION CHANGE
TO Approved for public release, distribution unlimited
FROM Distribution authorized to U.S. Gov't. agencies only; Test and Evaluation; MAR 1982. Other requests shall be referred to Air Force Rocket Propulsion Laboratory, ATTN: TSPR/STINFO, Edwards AFB, CA 93523.
AUTHORITY
AFRPL ltr dtd 6 Dec 1985

THIS PAGE IS UNCLASSIFIED

AD B064202

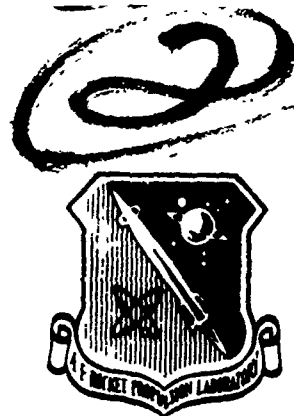
AUTHORITY:

AFRPL H 6 Dec 85



L

AFRPL-TR-82-13



RETRIEVAL OF FLOW-FIELD GAS TEMPERATURE AND
CONCENTRATION IN LOW-VISIBILITY PROPELLANT
ROCKET EXHAUST PLUMES

Author: Stephen J. Young

The Aerospace Corporation
El Segundo, California 90245

March 1982

Interim Report for the period October 1980 through September 1981

SUBJECT TO EXPORT CONTROL LAWS

This document contains information for manufacturing or using munitions of war. Exporting this information or releasing it to foreign nationals living in the United States without first obtaining an export license violates the International Traffic in Arms Regulations. Under 22 USC 2778, such a violation is punishable by up to 2 years in prison and by a fine of \$100,000.

Distribution limited to U.S. Government agencies only; Test and Evaluation, Mar 82. Other requests for this document must be referred to AFRPL/TSPR (Stop 24), Edwards AFB, CA 93523.

Prepared for
AIR FORCE ROCKET PROPULSION LABORATORY
DIRECTOR OF SCIENCE AND TECHNOLOGY
AIR FORCE SYSTEMS COMMAND
EDWARDS AFB, CALIFORNIA 93523

DTIC
ELECTE
MAY 4 1982

S D

82 05 03 121


AD B064202

DTIC FILE COPY

FOREWARD

This report was submitted by the Aerospace Corporation, P.O. Box 92957, Los Angeles, California, 90009, under Procurement Directive AFRPL/SD 81-2 Job Order No. 573010CU with the Air Force Rocket Propulsion Laboratory, Edwards AFB, CA 93523.

This report has been reviewed by the Technical Information Office (STINFO)/TSPR and is releasable to the National Technical Information Service (NTIS). At NTIS it will be available to the general public, including foreign nations. This technical report has been reviewed and is approved for publication; it is unclassified and suitable for general public release.


MICHAEL NOONAN, 2Lt, USAF
Project Manager


WILBUR C. ANDREPONT
Chief, Plume Technology Branch


EDWARD E. STEIN
Deputy Chief, Propulsion Analysis Division

UNCLASSIFIED

SECURITY CLASSIFICATION OF THIS PAGE (When Data Entered)

REPORT DOCUMENTATION PAGE		READ INSTRUCTIONS BEFORE COMPLETING FORM
1. REPORT NUMBER AFRPL-TR-82-13	2. GOVT ACCESSION NO. AD-B064201	3. RECIPIENT'S CATALOG NUMBER
4. TITLE (and Subtitle) RETRIEVAL OF FLOW-FIELD GAS TEMPERATURE AND CONCENTRATION IN LOW-VISIBILITY PROPELLANT ROCKET EXHAUST PLUMES	5. TYPE OF REPORT & PERIOD COVERED Interim Oct 1980 - Sep 1981	
	6. PERFORMING ORG. REPORT NUMBER	
7. AUTHOR(s) Stephen J. Young	8. CONTRACT OR GRANT NUMBER(s) F04701-81-C-0082	
9. PERFORMING ORGANIZATION NAME AND ADDRESS The Aerospace Corporation El Segundo, CA 90245	10. PROGRAM ELEMENT, PROJECT, TASK AREA & WORK UNIT NUMBERS	
11. CONTROLLING OFFICE NAME AND ADDRESS Air Force Rocket Propulsion Laboratory/DYP Edwards AFB, CA 93523	12. REPORT DATE March 1982	
	13. NUMBER OF PAGES 127	
14. MONITORING AGENCY NAME & ADDRESS (if different from Controlling Office) Space Division Air Force Systems Command Los Angeles, CA 90009	15. SECURITY CLASS. (of this report) UNCLASSIFIED	
	15a. DECLASSIFICATION/DOWNGRADING SCHEDULE	
16. DISTRIBUTION STATEMENT (of this Report) Distribution limited to U.S. Government agencies only; Test and Evaluation, Mar 1982. Other requests for this document must be referred to AFRPL/TSPR (STINFO), Edwards AFB, CA 93523.		
17. DISTRIBUTION STATEMENT (of the abstract entered in Block 20, if different from Report)		
18. SUPPLEMENTARY NOTES		
19. KEY WORDS (Continue on reverse side if necessary and identify by block number) Plume Diagnostics Rocket Plume Radiation Two-Phase Plumes		
20. ABSTRACT (Continue on reverse side if necessary and identify by block number) Estimates have been obtained for the maximum loading level of particles in two-phase rocket exhaust plumes that still allows a reliable determination of flow-field temperature and active gas distribution using gas-only plume retrieval diagnostics. Spatial profiles of emission and absorption transverse to the plume axis and close to the nozzle exit plane were computed for various plume models using a single-scattering band model that correctly couples gas and particle radiation. Retrieval of radial gas temperature and concentration profiles from these transverse profiles were performed with an iterative Abel		

DD FORM 1 JAN 73 1473

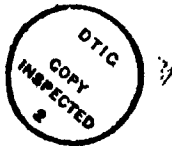
EDITION OF 1 NOV 65 IS OBSOLETE

UNCLASSIFIED

SECURITY CLASSIFICATION OF THIS PAGE (When Data Entered)

inversion algorithm designed for purely gaseous plumes. The retrieved profiles were compared with the model profiles to determine the error introduced by ignoring particle effects in inversion. A first-order method for accounting for particle effects was also examined. Results are presented for modeled tactical rocket plumes for candidate low-visibility propellants containing Al_2O_3/H_2O , Carbon/HCl and ZrO_2/H_2O as the particulate/gas pairs.

Accession For	
NTIS GRA&I	<input type="checkbox"/>
DTIC TAB	<input checked="" type="checkbox"/>
Unannounced	<input type="checkbox"/>
Justification	
By	
Distribution/	
Availability Codes	
Dist	Avail and/or Special
B	



CONTENTS

1.	INTRODUCTION	9
1.1	Background	9
1.2	Scope of Present Study	11
2.	PLUME RADIATION CALCULATION	13
2.1	Single-Scattering Band Model	13
2.2	Calculation Procedures	19
3.	GAS AND PARTICLE OPTICAL PARAMETERS	29
3.1	Gas Band Model Parameters	29
3.2	Particle Optical Parameters	31
3.2.1	Refractive Index	37
3.2.2	Size Distributions	39
3.2.3	Scattering Cross Sections	43
4.	EXAMPLE APPLICATIONS	53
4.1	Minimum Smoke Propellant (H_2O/Al_2O_3)	53
4.1.1	Preliminary Analysis	53
4.1.2	Final Analysis	65
4.2	Advanced Liquid Propellant (HCl/Carbon) Plume	83
4.3	Reduced Smoke Propellant ($H_2O, CO_2, CO, HCl/ZrO_2$) Plume	103
5.	SUMMARY AND CONCLUSIONS	121
	REFERENCES	125
	APPENDIX. CONVERSION BETWEEN NUMBER DENSITY, MASS LOADING, AND MOLE FRACTION	127

THIS PAGE LEFT INTENTIONALLY BLANK

FIGURES

1.	General Scattering Geometry	14
2.	Plume Scattering Geometry	21
3.	Line-of-Sight Integration Grid	23
4.	Plume Scattering Geometry	25
5.	Band Model Parameters for H ₂ O	32
6.	Band Model Parameters for CO ₂	33
7.	Band Model Parameters for CO	34
8.	Band Model Parameters for HCl	35
9.	Bimodal Particle Size Distribution for Al ₂ O ₃ and ZrO ₂	42
10.	Particle Size Distribution for Carbon	44
11.	Differential Scattering Cross Section for Al ₂ O ₃	46
12.	Differential Scattering Cross Section for Carbon	48
13.	Differential Scattering Cross Section for 1300K ZrO ₂	50
14.	Differential Scatting Cross Section for 2000K ZrO ₂	51
15.	Radial pTc Profiles for the Preliminary MSP Plume Model . . .	54
16.	Coverage of the Scattering Integral Weighting Function by the 11-Point Scattering Angle Grid	56
17.	Convergence of Scattered Radiance with Angle Integration Grid Resolution	58
18.	Plume Radiance Contributions for the Preliminary MSP Plume Model	62
19.	Plume Extinctance Contributions for the Preliminary MSP Plume Model	63

FIGURES (Continued)

20.	Temperature Convergence for Inversion of E/A Profiles Generated with EMABIC and EAPROF for the Preliminary MSP Plume Model	66
21.	Concentration Convergence for Inversion of E/A Profiles Generated with EMABIC and EAPROF for the Preliminary MSP Plume Model	67
22.	Convergence Residuals for Inversion of E/A Profiles Generated with EMABIC and EAPROF for the Preliminary MSP Plume Model	69
23.	Radial pTc Profiles for the MSP Plume Model	70
24.	Transverse Radiance Profiles for the MSP Plume Model	72
25.	Transverse Extinctance Profiles for the MSP Plume Model	73
26.	Variation of Radiance and Extinctance at $z = 0$ with Particle Density for the MSP Plume Model	74
27.	Temperature Retrieval for the MSP Plume Model	76
28.	Concentration Retrieval for the MSP Plume Model	77
29.	Temperature Retrieval Error on the Plume Axis for the MSP Plume Model	79
30.	Concentration Retrieval Error on the Plume Axis for the MSP Plume Model	80
31.	Transverse Radiance Profiles for Gas and Particle Phases for the MSP Plume Model	81
32.	Transverse Extinctance Profiles for Gas and Particle Phases for the MSP Plume Model	82
33.	Residual Errors in Radiance after First-Order, Off-Band Correction for the MSP Plume Model	84
34.	Retrieval Error Profiles for the MSP Plume Model	85
35.	Radial pTc Profiles for the ALP Plume Model	89

FIGURES (Continued)

36.	Transverse Radiance Profiles for the ALP Plume Model	91
37.	Transverse Extinctance Profiles for the ALP Plume Model . . .	92
38.	Variation of Radiance and Extinctance at $z = 0$ with Particle Density for the ALP Plume Model	93
39.	Transverse Radiance Profiles for the ALP Plume Model Computed with and without Scattering	95
40.	Transverse Extinctance Profiles for the ALP Plume Model Computed with and without Scattering	96
41.	Temperature Retrieval Results for the ALP Plume Model	98
42.	Concentration Retrieval Results for the ALP Plume Model . . .	99
43.	Temperature Retrieval Error on the Plume Axis for the ALP Plume Model	100
44.	Concentration Retrieval Error on the Plume Axis for the ALP Plume Model	101
45.	Radial pTc Profiles for the Low-Temperature RSP Plume Model	104
46.	Radial pTc Profiles for the High-Temperature RSP Plume Model	105
47.	Gaussian Spatial Distribution of Particle Concentration	108
48.	Transverse E/A Profiles for CO	111
49.	Transverse E/A Profiles for CO ₂	112
50.	Transverse E/A Profiles for HCl	113
51.	Transverse E/A Profiles for H ₂ O	114
52.	Transverse Radiance Profiles for H ₂ O/ZrO ₂ in the Low- Temperature RSP Plume Model with Bimodal Size and Gaussian Spatial Distributions	116

FIGURES (Continued)

53. Transverse Extinctance Profiles for H_2O/ZrO_2 in the Low-Temperature RSP Plume Model with Bimodal Size and Gaussian Spatial Distributions 117
54. Temperature and Concentration Retrieval Results for the Low-Temperature H_2O/ZrO_2 RSP Plume Model with Bimodal Size and Gaussian Spatial Distributions 120

TABLES

1.	Spectral Bandpass Parameters	30
2.	Linewidth Band Model Parameter	36
3.	Particle Indices of Refraction	40
4.	Al ₂ O ₃ Scattering Cross Sections	45
5.	ZrO ₂ Scattering Cross Sections	49
6.	Plume Radiance Contributions for the Preliminary MSP Plume Model	60
7.	Plume Extinctance Contributions for the Preliminary MSP Plume Model	61
8.	Comparison of E/A Profiles Generated with EMABIC and EAPROF for the Preliminary MSP Plume Model	64
9.	Comparison of Retrieved and True Radial Profiles for the MSP Plume Model	68
10.	Variation of Radiance and Extinctance at z = 0 with Particle Density for the MSP Plume Model	75
11.	Temperature and Gas Concentration Retrieval Results on the Plume Axis for the MSP Plume Model	78
12.	Temperature and Gas Concentration Retrieval Results on Plume Axis with and without First-Order, Off-Band Correction Procedure	86
13.	Maximum Al ₂ O ₃ Loading Levels for Various Retrieval and Calculation Conditions	87
14.	Species Concentrations for the ALP Plume Model	88
15.	Variation of Radiance and Extinctance at z = 0 with Particle Density for the ALP Plume Model	94
16.	Temperature and Gas Concentration Retrieval Results on Plume Axis for the ALP Plume Model	102

TABLES (Continued)

17.	Species Concentrations for RSP Plume Model	106
18.	Effective Plume Lengths for RSP Plume Model	110
19.	E/A Results at $z = 0$ for the RSP Plume Models	115
20.	Temperature Retrieval Results for RSP Plume Model	118
21.	H ₂ O Concentration Retrieval Results RSP Plume Model	119
22.	Summary of Critical Loading Levels	123
A1.	Particle Loading Conversion Formulas	129
A2.	Density, Mass, and Volume Parameters for Solid-Phase Species	130

1. INTRODUCTION

1.1 Background

For the past few years, the Air Force Rocket Propulsion Laboratory (AFRPL) has sponsored a series of theoretical and experimental programs on the retrieval of plume flow-field properties by analysis of the infrared radiative and absorptive properties of plumes. This report covers the third phase of study in these programs by The Aerospace Corporation. The first phase¹ was a study of the classic problem of retrieving radial profiles of gas temperature and concentration in cylindrically-symmetric, gaseous plumes from transverse profiles of emission and absorption (E/A profiles) obtained in a fixed spectral bandpass. The E/A profiles are defined in terms of the radial profiles of pressure, temperature, and concentration (pTc profiles) by integral equations of radiative transfer. Retrieval of the pTc profiles from the E/A profiles involves a numerical inversion of these integral equations. In this study, an inversion procedure was developed and incorporated into the computer code EMABIC. This code was used extensively in the present study. The inversion algorithm is an iterative Abel inversion. The well-known Abel inversion procedure is valid for optically thin sources; for the general case of optical thickness, an iterative procedure is required. The code has been applied to several synthetic and experimental data and performs satisfactorily as a diagnostic for most gas-only plume problems. Some problems occur when the temperature profile has a deep minimum on the plume axis or when the input E/A profiles are particularly noisy, even if they are adequately smoothed. This is an inherent feature of inversion, however, and is not

1. S. J. Young, Inversion of Plume Radiance and Absorption Data for Temperature and Concentration, AFRPL-TR-78-60, U.S. Air Force Rocket Propulsion Laboratory, Edwards Air Force Base, Calif., 29 September 1978.

restricted to the method of inversion. A similar inversion code has been developed at AEDC.² Recently, a random error propagation routine was added to EMABIC so that retrieval error could be estimated automatically from E/A measurement error.³

The second phase of study was to consider multispectral inversion and the effects of particle loading in tactical motor plumes. In multispectral inversion, retrieval is made on the basis of how E/A spectra vary in wavelength for a fixed measurement line of sight. It was found that this inversion scheme is not applicable in the infrared on either a monochromatic or wide band spectral scale near the exit plane for small plumes with mild temperature gradients such as those characteristic of tactical rocket motor. Even under the most ideal circumstances, temperature and concentration retrieval errors up to 30% were encountered. The failure of the method is caused by the lack of spatial resolution inherent in the inversion weighting functions. Results of this study are reported in Ref. 4. Because this method failed for purely gaseous plumes, it was never applied to two-phase plumes. The decision was made to revert to the multiposition inversion diagnostic of the first study phase and to pursue its application to two-phase, tactical rocket motor plumes.

-
2. C. C. Limbaugh, W. T. Bertrand, E. L. Kiech and T. G. McRae, Nozzle Exit Plane Radiation Diagnostics Measurements of the Improved Transtage Liquid Rocket Injector Program, AEDC-TR-79-29, ARO Inc., Arnold Engineering Development Center, Arnold Air Force Station, Tenn., March 1980.
 3. S. J. Young, Random Error Propagation Analysis in the Plume Diagnostic Code EMABIC, AFRPL Technical Report, to be published.
 4. S. J. Young, Multicolor Inversion Diagnostic for Tactical Motor Plumes, AFRPL-TR-80-30, U.S. Air Force Rocket Propulsion Laboratory, Edwards Air Force Base, Calif., May 1980.

1.2 Scope of Present Study

The concern of the present work was to determine how applicable the gas-only, multiposition inversion diagnostic code EMABIC is to plumes containing particles. The work focused on tactical rocket motors where the particle loading level is small, that is, to motors where the particulate material is added to the fuel only as a stabilizer (e. g., Al_2O_3), or to motors where the plume particulate results from chemical reactions (e. g., Carbon) but not to motors in which the major fuel is itself a metal.

The general procedure of the study was to: (1) assume reasonable pTc profiles and particle loading levels for plumes of interest, (2) generate E/A profiles taking account of particle emission/absorption/scattering, (3) invert these E/A profiles with the inversion code EMABIC as though they were for a purely gaseous plume, and (4) compare the retrieved profiles with the known input profiles. The results, presented later, will show that the method cannot tolerate much particulate loading without introducing appreciable error into the retrieved gas concentration profile. Temperature retrieval is less sensitive to particle loading. A correction procedure was derived that substantially increases the ability to retrieve the correct profiles. In an actual experiment, E/A data would be obtained in a bandpass appropriate to the gas species of interest. This data would reflect both gas and particle effects. By collecting data off the gas absorption band, one could obtain data that primarily reflects just the particle effects. This off-band data could be used to "correct" the on-band data to give E/A profiles closer to the gas-only profiles needed by the inversion program. In this work, the off-band data was approximated by the E/A profiles caused by the particles alone, and only the first-order correction of subtracting the off-band radiance from the on-band radiance, and dividing the on-band transmittance by the off-band transmittance was employed. This procedure is valid only if the plume is optically thin to both gas and particle absorption.

The most restricting feature of the present work was the use of the single-scattering approximation in the calculation of E/A profiles. The use of this approximation is partly justified by the low loading levels considered. These calculations are considered in Section 2. In Section 3, the optical properties of all the gases (H_2O , CO_2 , CO and HCl) and particles (Al_2O_3 , Carbon, and ZrO_2) considered in the work are discussed, and in Section 4 specific plume models are considered.

2. PLUME RADIATION CALCULATION

2.1 Single-Scattering Band Model

In this section, the band model equations for radiative transfer in a general, nonuniform, two-phase (gas and particles) medium are derived. The formulation considers only single scattering, but allows different temperatures for the gas and particle phases and treats the scattering of external source radiation (e.g., nozzle exit plane radiation) incident on the medium. The geometry of the problem is shown in Fig. 1. The monochromatic transfer equation for the radiance along the primary line of sight (LOS) s directed toward the sensor is

$$\begin{aligned} -\frac{dN(\nu, s)}{ds} = & -[\alpha(s) + \beta(s) + \kappa(\nu, s)] N(\nu, s) + \alpha(s) B_p(s) + \kappa(\nu, s) B_g(s) \\ & + \frac{\beta(s)}{4\pi} \int_{4\pi} p(s, \Omega) N(\nu, s, \Omega) d\Omega \end{aligned} \quad (1)$$

where

ν = wavenumber,

Ω = shorthand notation for direction described by scattering angle θ and azimuthal angle ϕ ,

$N(\nu, s, \Omega)$ = radiance directed along $-\Omega$ direction,

$B_g(s)$ = Planck function evaluated at gas temperature $T_g(s)$,

$B_p(s)$ = Planck function evaluated at particle temperature $T_p(s)$,

$\alpha(s)$ = particle absorption parameter,

$\beta(s)$ = particle scattering parameter,

$p(s, \Omega)$ = scattering phase function for scattering from $-\Omega$,
direction to $-s$ direction,

and $\kappa(\nu, s)$ = gas absorption parameter.

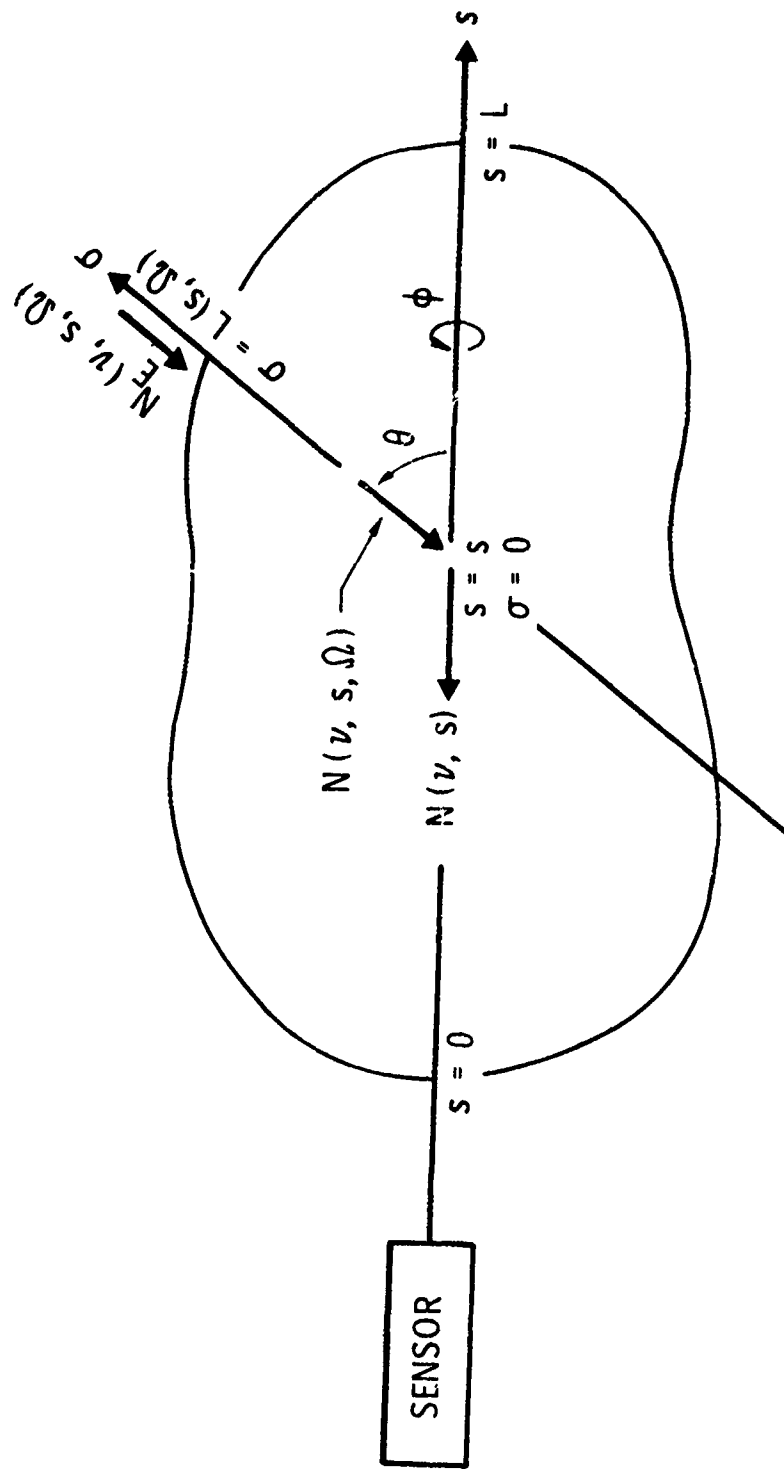


Fig. 1. General Scattering Geometry.

The parameters $\alpha(s)$, $\beta(s)$, and $p(s, \Omega)$ are defined by

$$\begin{aligned}\alpha(s) &= \sigma_a(s) N_p(s) \\ \beta(s) &= \sigma_s(s) N_p(s) \\ p(s, \Omega) &= \frac{4\pi}{\sigma_s(s)} \frac{d\sigma(s, \theta)}{d\Omega}\end{aligned}$$

where $\sigma_a(s)$, $\sigma_s(s)$, and $d\sigma_s(\theta)/d\Omega$ are, respectively, the absorption, total scattering, and differential scattering cross sections for the particles (scattering by gas molecules is neglected). The scattering phase function $p(s, \Omega)$ is normalized by

$$\frac{1}{4\pi} \int_{4\pi} p(s, \Omega) d\Omega = \frac{1}{2} \int_0^\pi p(s, \Omega) \sin\theta d\theta = 1.$$

$N_p(s)$ is the particle number density. The gas absorption parameter is defined by

$$\kappa(\nu, s) = c(s) p(s) k(\nu, s)$$

where $c(s)$ is the gas concentration (mole fraction), $p(s)$ is the total gas pressure, and $k(\nu, s)$ is the monochromatic absorption coefficient. Equation (1) is written for a small spectral interval $\Delta\nu$ within which all parameters are independent of ν except for $\kappa(\nu, s)$ and, of course, $N(\nu, s)$ and $N(\nu, s, \Omega)$.

The single-scattering approximation results by replacing $N(\nu, s, \Omega)$ with the value it would obtain in the absence of scattering, i. e., with $\beta \equiv 0$. Specifically, $N(\nu, s, \Omega)$ is approximated as the solution of

$$\begin{aligned}
-\frac{dN(\nu, s, \sigma, \Omega)}{d\sigma} &= -[\alpha(\sigma) + \kappa(\nu, \sigma)]N(\nu, s, \sigma, \Omega) \\
&+ \alpha(\sigma)B_p(\sigma) + \kappa(\nu, \sigma)B_g(\sigma)
\end{aligned}
\tag{2}$$

evaluated at $\sigma=0$ and with the imposed boundary condition $N(\nu, s, \sigma, \Omega) = N_E(\nu, s, \Omega)$ at $\sigma=L(s, \Omega)$. The result is

$$\begin{aligned}
N(\nu, s, \Omega) &= \int_0^{L(s, \Omega)} [\alpha(\sigma)B_p(\sigma) + \kappa(\nu, \sigma)B_g(\sigma)] \tau_\alpha(\sigma) \tau_\kappa(\nu, \sigma) d\sigma \\
&+ N_E(\nu, s, \Omega) \tau_\alpha[L(s, \Omega)] \tau_\kappa[\nu, L(s, \Omega)]
\end{aligned}
\tag{3}$$

where

$$\tau_\alpha(\sigma) = \exp \left\{ - \int_0^\sigma \alpha(\sigma') d\sigma' \right\}
\tag{4}$$

$$\tau_\kappa(\nu, \sigma) = \exp \left\{ - \int_0^\sigma \kappa(\nu, \sigma') d\sigma' \right\}.
\tag{5}$$

Substitution of Eq. (3) into (1) and carrying out the solution of the first order differential equation subject to the boundary condition $N(\nu, s) = 0$ at $s = L$ yields the following solution for the emergent radiance $N(\nu) = N(\nu, s=0)$

$$\begin{aligned}
N(\nu) = & \int_0^L \left[\alpha(s) B_p(s) \tau_\alpha(s) \tau_\beta(s) \tau_K(\nu, s) - B_g(s) \tau_\alpha(s) \tau_\beta(s) \frac{d\tau_K(\nu, s)}{ds} \right. \\
& + \tau_\alpha(s) \tau_\beta(s) \frac{\beta(s)}{4\pi} \int_{4\pi} p(s, \Omega) \left\{ \int_0^{L(s, \Omega)} \left[\alpha(\sigma) B_p(\sigma) \tau_\alpha(\sigma) \tau_K(\nu, s + \sigma) \right. \right. \\
& \left. \left. - B_g(\sigma) \tau_\alpha(\sigma) \frac{d\tau_K(\nu, s + \sigma)}{d\sigma} \right] d\sigma \right. \\
& \left. \left. + N_E(\nu, s, \Omega) \tau_\alpha[L(s, \Omega)] \tau_K[\nu, s + L(s, \Omega)] \right\} d\Omega \right] ds \quad (6)
\end{aligned}$$

where

$$\tau_\beta(s) = \exp \left\{ - \int_0^s \beta(s') ds' \right\} \quad (7)$$

and

$$\tau_K(\nu, s + L) = \tau_K(\nu, s) \tau_K(\nu, L). \quad (8)$$

In this form, there are no products of spectrally correlated functions, and the solution for the mean radiance

$$\bar{N} = \frac{1}{\Delta \nu} \int_{\Delta \nu} N(\nu) d\nu \quad (9)$$

can be obtained immediately by replacing all references to $\tau_K(\nu, s)$ and $d\tau_K(\nu, s)/ds$ in Eq. (6) by $\bar{\tau}(s)$ and $d\bar{\tau}(s)/ds$, respectively, where $\bar{\tau}(s)$ is an appropriate band model transmittance function. Also, we assume $N_E(\nu)$ independent of ν and replace it with \bar{N}_E . In the statistical band model, the transmittance derivative can be written as¹

$$\frac{d\bar{\tau}(s)}{ds} = - \bar{\tau}(s) \bar{\kappa}(s) y(s) \quad (10)$$

where $\bar{\kappa}(s)$ is the mean absorption coefficient

$$\bar{\kappa}(s) = \frac{1}{\Delta\nu} \int_{\Delta\nu} \kappa(\nu, s) d\nu \quad (11)$$

and $y(s)$ is an equivalent width derivative function whose explicit form depends on the absorption line shape and the approximation used to account for nonuniformities along the optical path. In effect, this function accounts for the deviation of band absorptance from Beer's and Lambert's laws. Lambert's law obtains for $y=1$. Use of Eq. (10) in the mean radiance version of (6) allows the final solution to be written in the more usable form

$$\begin{aligned} \bar{N} &= \int_0^L \tau_\alpha(s) \tau_\beta(s) \bar{\tau}(s) \left\{ Q_T(s) + Q_S(s) \right\} ds \\ Q_T(s) &= \alpha(s) B_p(s) + \bar{\kappa}(s) y(s) B_g(s) \\ Q_S(s) &= \frac{\beta(s)}{4\pi} \int_{4\pi} p(s, \Omega) \left[\tau_\alpha[L(s, \Omega)] \frac{\bar{\tau}[s+L(s, \Omega)]}{\bar{\tau}(s)} \bar{N}_E(s, \Omega) \right. \\ &\quad \left. + \int_0^{L(s, \Omega)} \tau_\alpha(\sigma) \frac{\bar{\tau}(s+\sigma)}{\bar{\tau}(s)} \left\{ \alpha(\sigma) B_p(\sigma) + \bar{\kappa}(\sigma) y(\sigma+s) B_g(\sigma) \right\} d\sigma \right] d\Omega. \end{aligned} \quad (12)$$

$Q_T(s)$ is a thermal source term and $Q_S(s)$ is a scattering source term. The transmittance through the medium along the primary LOS is

$$\bar{\tau}_T = \tau_\alpha(L) \tau_\beta(L) \bar{\tau}(L) \quad (13)$$

Equations (12) and (13) are the general formulas used to compute plume E/A profiles. Their application to the plume problem is considered in the next section.

The gas band model formulations used to compute the mean transmittance $\bar{\tau}$ and the derivative function y are described in detail in Ref. 1. Briefly, the formulation employs the Malkmus random band model with provisions for Lorentz, Doppler, or Voigt line profiles. Nonuniformities in the plume are handled with either the Curtis-Godson (CG) or derivative (DR) approximations.

A significant feature of the result for radiance, Eq. (12), is that it correctly accounts for the nonmultiplicative nature of band model transmittances. This account is made in three places: First, radiation that is emitted at position σ on the scattering LOS and will eventually be scattered into the primary LOS is not simply multiplied by $\bar{\tau}(\sigma)$ to get its contribution to the scattering source function at s . Rather, its contribution is correctly computed by multiplication with $\bar{\tau}(s+\sigma)/\bar{\tau}(s)$ where $\bar{\tau}(s+\sigma)$ is the transmittance for the path $s=0$ to $s=s(\sigma=0)$ and then on to $\sigma=\sigma$ treated as a single, coupled LOS. Note that for monochromatic radiation, where the multiplicative property does hold, this procedure would yield $\tau(\nu, s+\sigma)/\tau(\nu, s) \equiv \tau(\nu, \sigma)$ as expected. Second, this same account is made for the scattering of external source radiation into the primary LOS. The third account is the use of $y(s+\sigma)$ instead of just $y(\sigma)$ in the expression for $Q_S(s)$.

2.2 Calculation Procedures

Calculation procedures and the application of the results of Section 2.1 to plumes are described here. The final results have been incorporated into a computer code which is described in a separate publication.⁵

5. S. J. Young, User's Manual for the Plume Signature Code EAPROF, AFRPL-TR-81-08, U.S. Air Force Rocket Propulsion Laboratory, Edwards Air Force Base, Calif., January 1981.

The geometry of the problem is shown in Fig. 2. The plume is assumed to be cylindrically symmetric and axially uniform. The observation plane is located a distance L_1 downstream of the nozzle exit plane and the plume extends a distance L_2 beyond the observation plane. In gas-only radiation prediction and inversion, no consideration has to be given to plume length because all radiation observed originates in the observation plane. In two-phase plumes, account has to be made of radiation scattered into the observation line of sight from other parts of the plume. In order to assign a length L_2 to the model plume, the following procedure was used. First, realistic flow-field calculations were performed (by AFRPL) for plumes of interest. From these results, the decay of pressure, temperature, and gas concentration down the plume axis were determined. Second, for these pTc variations (or approximations to them) the gas-only radiance at the observation station directed along the plume axis toward the exit plane was computed. Finally, a similar calculation was made for the axially uniform model (with pressure, temperature, and gas concentration on axis equal to the flow-field calculation results on axis at the observation station) with L_2 adjusted until the radiance was equal to the previous result. Specific values for L_1 and L_2 , are indicated later for actual cases considered. L_1 was generally 2 to 3 cm and L_2 40 to 60 cm.

The s-axis is the primary LOS. In Fig. 2, the LOS through a full plume diameter is shown, but as the LOS is scanned across the lateral extent of the plume, it becomes increasingly shorter. The σ -axis is the scattering LOS and is described by the value of s at which it branches off the primary LOS, the scattering angle θ , and the azimuthal angle ϕ . The length of the scattering LOS is $L(s, \theta, \phi)$ and reflects the termination of the LOS either on the plume boundary, the nozzle exit plane, or the plume end plane. If the scattering LOS terminates on the nozzle exit plane, account is made of thermal motor radiation scattered into the primary LOS. This radiation is modeled as arising from a disc at the exit plane with uniform temperature T_E and emissivity ϵ .

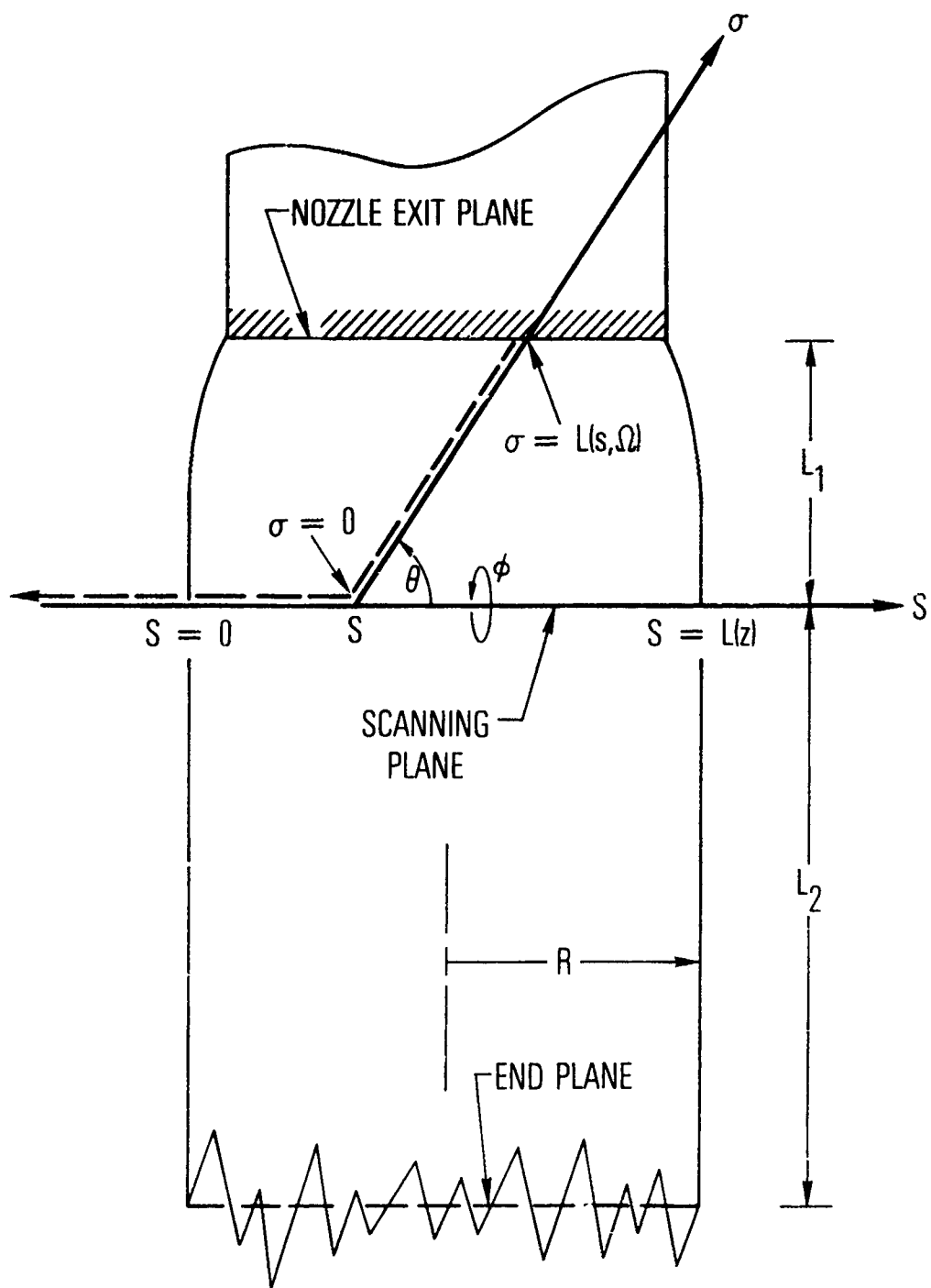


Fig. 2. Plume Scattering Geometry.

Four integrations are explicitly indicated in Eq. (12). The first is over the line of sight s . In the original form of EMABIC, this integration was transformed into a radial integration. With the inclusion of scattering, it is more convenient to retain s as the integration variable. The integration grid for s is taken as the set of points defined by the intersection of a given transverse LOS with the radial zone boundaries (as is illustrated in Fig. 3). The LOS integration is performed for each transverse position d of the grid. The number of transverse and radial zones used in the numerical routines is indicated by N . Values of $N = 7$ and 10 were used in this study. In the example of Fig. 3, $N = 6$. The radial coordinate index is i , the transverse coordinate index is j , and the primary LOS coordinate index is k . This last index runs from 1 to $2(N+1-j)+1$. The midpoint value for k is $k_m = N+2-j$. The radial index for a given value of k is

$$i = \begin{cases} N+2-k & k \leq k_m \\ 2(j-1)-N+k & k \geq k_m \end{cases}$$

The radial index is used to compute the actual radial coordinate $r=(i-1) R/N$ for each k so that an interpolation on tables of radial functions can be made to get the function value appropriate to k . The coordinate value s for each k is

$$s = \frac{R}{N} \left\{ \left[N^2 - (j-1)^2 \right]^{1/2} \pm \left[(i-1)^2 - (j-1)^2 \right]^{1/2} \right\}$$

where the $+$ sign is used for $k \leq k_m$ and the $-$ sign for $k \geq k_m$. A trapezoidal quadrature routine is used for the s -axis integration.

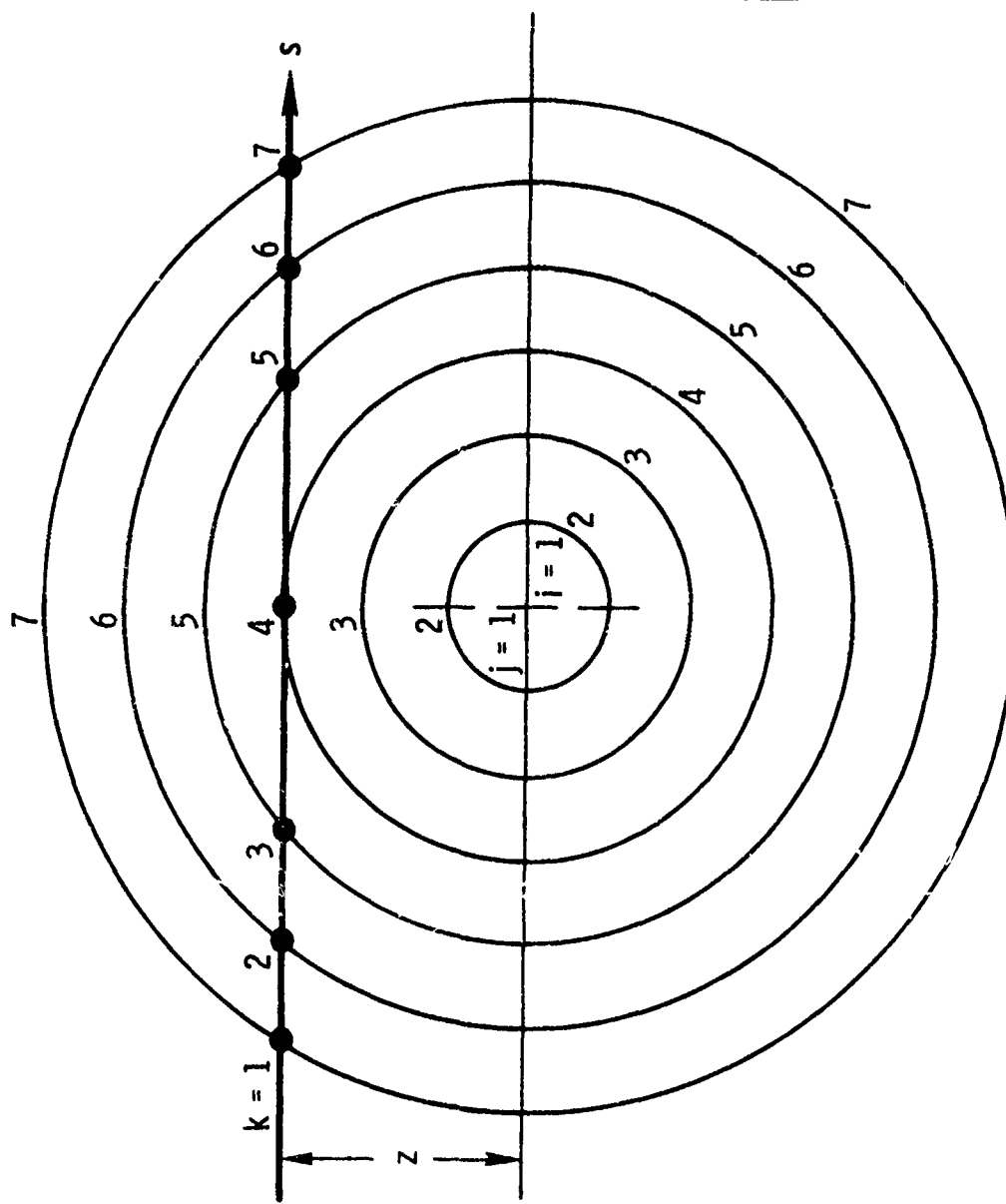


Fig. 3. Line-of-Sight Integration Grid.

At each grid point along a given transverse LOS, several calculations for the integrand of the s -integral must be made. The calculations for $\tau_\alpha(s)$, $\tau_\beta(s)$, $\bar{\tau}(s)$, and $Q_T(s)$ are straightforward. The calculation for $Q_S(s)$ involves three more integrations. Two of these integrations are over the scattering angle θ and azimuthal angle ϕ . In Eq. 12, these integrations are indicated by the single integral over Ω . The integration ranges are $0 \leq \theta \leq \pi$ and $0 \leq \phi \leq 2\pi$. A Simpson quadrature is used for θ near zero and trapezoidal quadrature is used for large θ and for the ϕ integration. The 2π range for ϕ is divided into N_ϕ equal size segments. Most of the work reported here was done with $N_\phi=16$. The θ integration grid is selected on the basis of how the phase function $p(\theta)$ varies with θ . If $p(\theta)$ peaks sharply around $\theta=0$, the density of grid points around $\theta \sim 0$ is made large. If $p(\theta)$ is relatively flat, a more uniform grid is used. For most of the work performed here, the following grid was used:

$$\theta_i = 0, 5, 15, 25, 35, 45, 60, 90, 120, 150 \text{ and } 180^\circ. \quad (14)$$

Further details on the selection of these ϕ and θ grids are given in Section 4.1.1.

The fourth integration is over the scattering LOS σ . Before this integration is performed, an analysis of the geometry is carried out to determine where the scattering LOS terminates, and how long it is. The relevant geometry for the analysis is shown in Fig. 4. A scattering LOS is defined by the distance s along the primary LOS where it branches off, the transverse distance z , and the angles θ and ϕ . The cylindrical coordinates for a point σ along the scattering LOS are

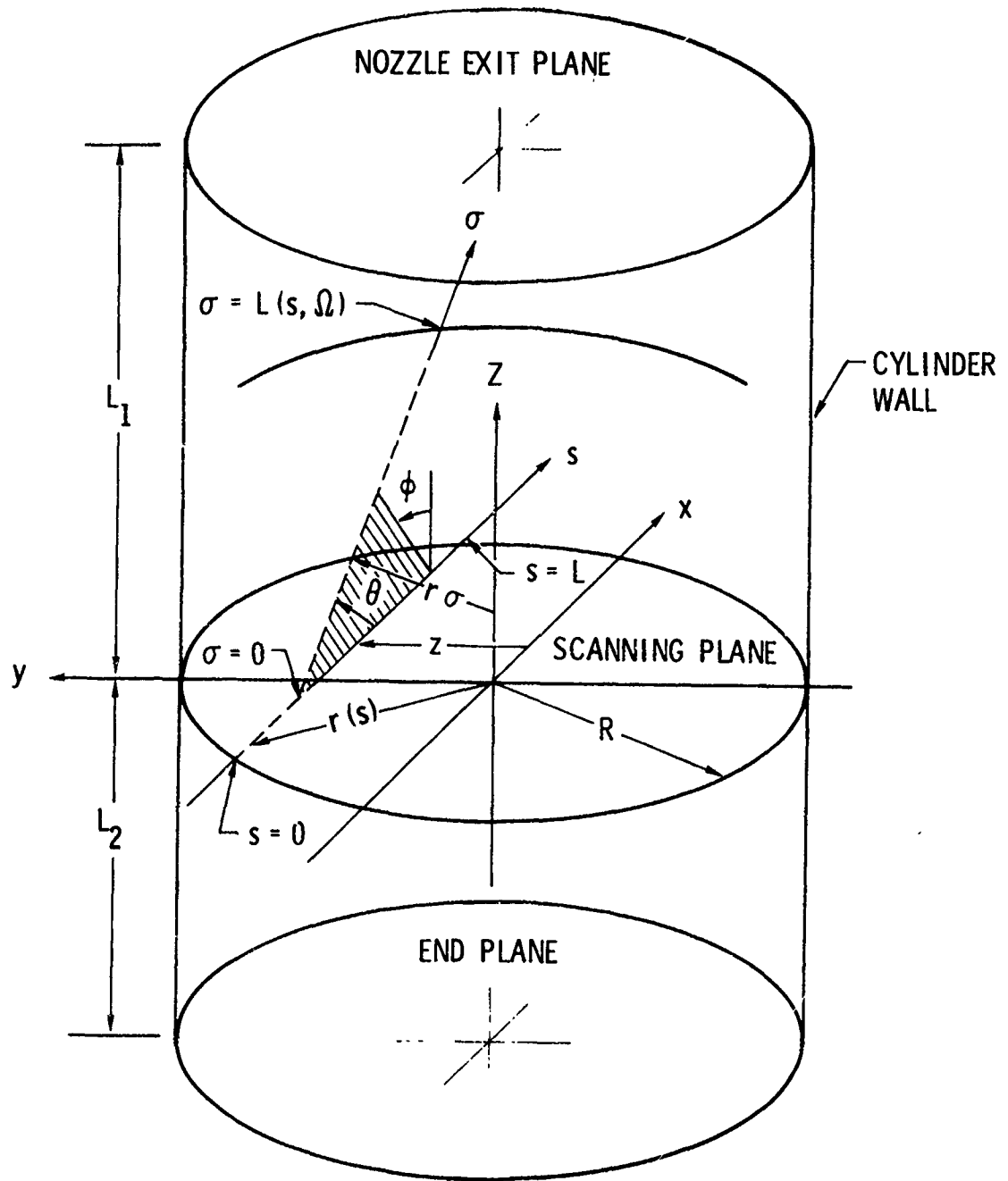


Fig. 4. Plume Scattering Geometry.

$$r(\sigma) = \left[(x_0 + \sigma \cos\theta)^2 + (y_0 + \sigma \sin\theta \sin\phi)^2 \right]^{1/2} \quad (15)$$

$$Z(\sigma) = \sigma \sin\theta \cos\phi \quad (16)$$

where

$$x_0 = s - \frac{s_m}{2}$$

$$y_0 = z$$

$$\frac{s_m}{2} = (R^2 - z^2)^{1/2}$$

For $0 \leq \phi \leq \pi/2$ or $3\pi/2 \leq \phi \leq 2\pi$, the scattering LOS is directed upward and intersects either the nozzle exit plane or the cylinder wall above the scanning plane. In order to test this, Eq. (16) is solved for σ with $Z(\sigma)$ set equal to L_1 . This value for σ is then substituted into Eq. (15) and solved for the value r_e that the scattering LOS would have at the exit plane. If r_e is less than R , the LOS ends on the exit plane and the length of the LOS is

$$L = \frac{L_1}{\sin\theta \cos\phi}$$

If r_e is greater than R , the LOS ends on the cylinder wall and the length is the solution of Eq. (15) with $r(\sigma)$ replaced with R , that is

$$L = \frac{1}{2a} \left[(b^2 + 4ac)^{1/2} - b \right]$$

where

$$a = \cos^2 \theta + \sin^2 \theta \sin^2 \phi = 1 - \sin^2 \theta \cos^2 \phi,$$

$$b = 2(x_0 \cos \theta + y_0 \sin \theta \sin \phi),$$

$$c = R^2 - x_0^2 - y_0^2 = R^2 - r_0^2.$$

For $\pi/2 \leq \phi \leq 3\pi/2$, the scattering LOS is directed downward. An analysis similar to that above is made to determine whether the LOS ends on the end plane or the cylinder wall. In this case, Eq. (16) is solved for σ with $Z(\sigma) = L_2$ and used to compute r_e . If $r_e < R$, the LOS ends on the end plane, and

$$L = \frac{-L_2}{\sin \theta \cos \phi}.$$

If $r_e > R$, the LOS ends on the cylinder wall, and its length is

$$L = \frac{1}{2a} \left[(b^2 + 4ac)^{1/2} + b \right]$$

where a, b , and c are the same as before.

When the length of the scattering LOS has been found, it is divided into N_s equal sized intervals, and the $N_s + 1$ radii of the interval boundaries computed from Eq. 15. These radii are then used to interpolate on tables of radial functions to get the integrands of the σ integral at the $N_s + 1$ points. A trapezoidal quadrature routine is used for the σ integration. All of the work reported here used $N_s = 10$.

Although the formulation procedure discussed so far does not require it, a significant simplification has been made in all of the work reported here -- it has been assumed that the particle size distribution and index of refraction are constants throughout the plume. In fact, this simplification is not very realistic in many cases, and more accurate account of the variability of these parameters throughout the plume is planned. Then $p(s, \Omega)$, $\alpha(s)$, $\beta(s)$, and $\alpha(\sigma)$ are independent of s or σ .

3. GAS AND PARTICLE OPTICAL PARAMETERS

All of the gas and particle data used in the analyses of Section 4 are considered here. Four gas species and three particle species were considered, but not all possible gas/particle pairings were analyzed.

3.1 Gas Band Model Parameters

The four gas species considered are H₂O, CO₂, CO, and HCl. The spectral bandpasses and resolution used for each species are listed in Table 1. The H₂O bandpass is one of those used in the recent AEDC E/A measurements program.² The HCl bandpass is simply located at the center of the emission band. The CO₂ emission band is located on the steeply rising blue wing of the CO₂ emission band. This is the only spectral region that is free of both CO and H₂O emission contamination, while at the same time is not so strongly absorbing as to preclude seeing into the plume. The CO bandpass is located just beyond the red wing limit of the CO₂ emission band to preclude contamination from that species. Consideration on the spectral purity of the H₂O, CO₂, and CO bandpass is made in Ref. 4.

The HCl and CO band model parameters were taken from the NASA handbook;⁶ the H₂O and CO₂ parameters are those of the plume signature code ATLES.⁷⁻¹⁰ The absorption parameter \bar{k} and line density parameter

6. C. B. Ludwig, W. Malkmus, J. E. Reardon, and J. A. L. Thompson, Handbook of Infrared Radiation from Combustion Gases, eds. R. Goulard and J. A. L. Thompson, NASA SP-3080, Marshall Space Flight Center, Huntsville, Ala., 1973.
7. S. J. Young, Band Model Parameters for the 2.7- μ m Bands of H₂O and CO₂ in the 100-3000°K Temperature Range, TR-0076(6970)-4, The Aerospace Corporation, El Segundo, Calif., 31 July 1975.
8. S. J. Young, Band Model Parameters for the 4.3- μ m Fundamental Band of CO₂ in the 100-3000°K Temperature Range, TR-0076(6754-03)-1, The Aerospace Corporation, El Segundo, Calif., 19 Feb. 1976.
9. S. J. Young, "Evaluation of Nonisothermal Band Models for H₂O," J. Quant. Spectrosc. Radiat. Transfer **18**, 29-45 (1977).
10. S. J. Young, Description and Use of the Plume Radiation Code ATLES, TR-0077(2753-04)-3, The Aerospace Corporation, El Segundo, Calif. 13 May 1977.

Table 1. Spectral Bandpass Parameters.

Species	$\lambda(\mu\text{m})$	$\Delta\lambda(\mu\text{m})$
CO	5.00	0.06
CO ₂	4.18	0.009
HCl	3.38	0.06
H ₂ O	2.51	0.2

$\bar{\delta}$ for the four species are shown in Figs. 5-8. Line broadening includes pressure broadening and Doppler broadening. The model is the same as that used in the code EMABIC,¹ and the relevant parameters are given in Table 2.

3.2 Particle Optical Properties

Many problems are involved in modeling the absorption, emission, and scattering properties of plume particulates, and, at present, any method of modeling is open to criticism. The principal problems concern the chemical composition (and homogeneity of composition), shape, particle size distribution, and spatial distribution of plume particles.

The three species of concern in this work are alumina (Al_2O_3), carbon (C), and zirconium oxide (ZrO_2). The particles were assumed to be spherical (or compact in form and randomly oriented) and homogeneous so that Mie theory could be used to model their scattering properties. The index of refraction of the bulk material was used in the calculations even though some doubt exists as to whether or not this is the proper value to use for particles whose size is comparable to the wavelength of interest.¹¹ Neglect of this effect is to a large part justified by the inaccuracy with which we know even the bulk index. The index data used in the present work are considered in Section 3.2.1.

In addition to the index of refraction, Mie scattering calculations require the size or size distribution of the particles. Again, little quantitative data exists for size distributions occurring in plumes. The distributions used in this work are discussed in Section 3.2.2.

11. A. B. Pluchino, S. S. Goldberg, J. M. Dowling and C. M. Randall, "Refractive Index Measurements of Single Micron-Sized Carbon Particles," *Applied Optics* 19, 3370-3372 (1980).

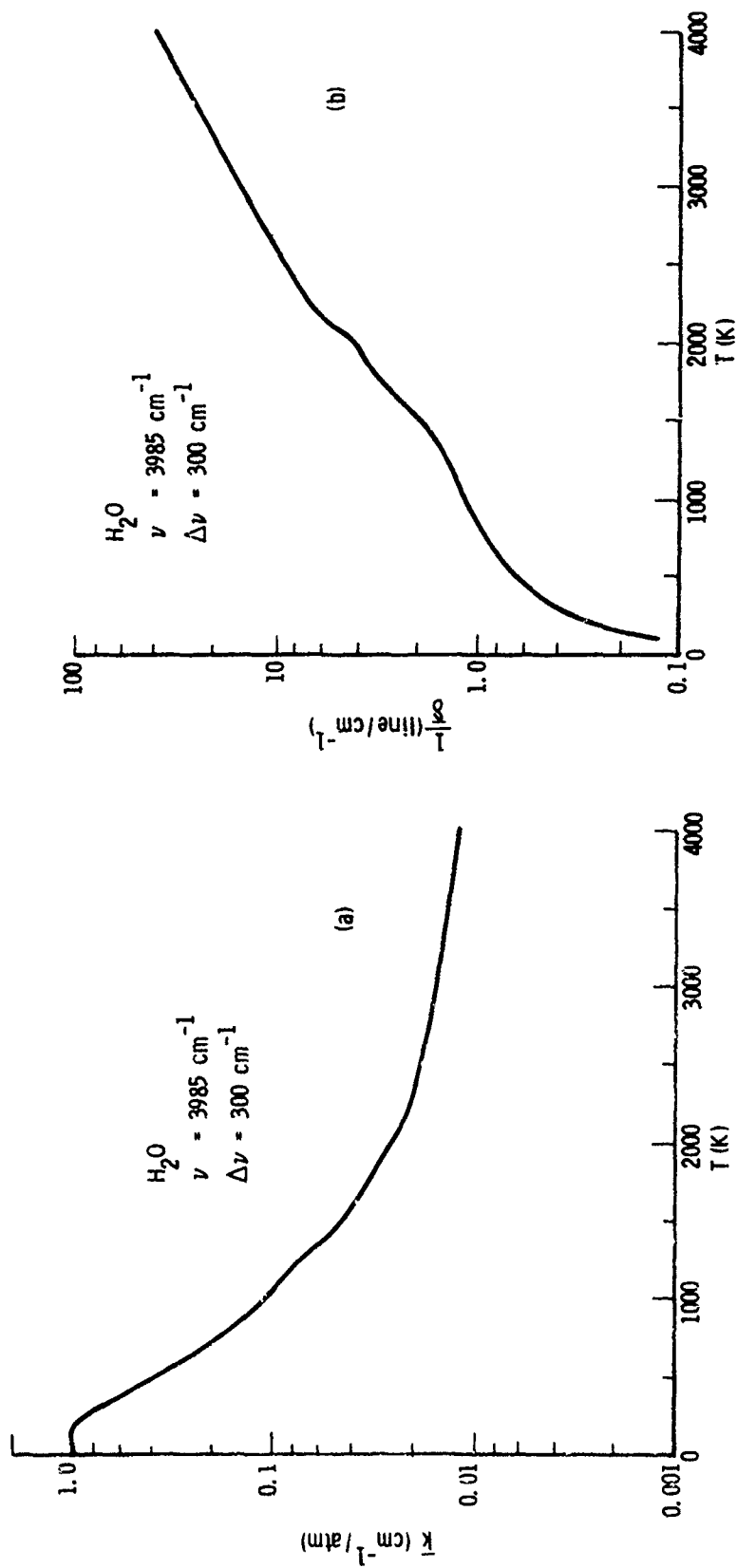


Fig. 5. Band Model Parameters for H_2O . (a) Absorption Parameter; (b) Line Density Parameter.

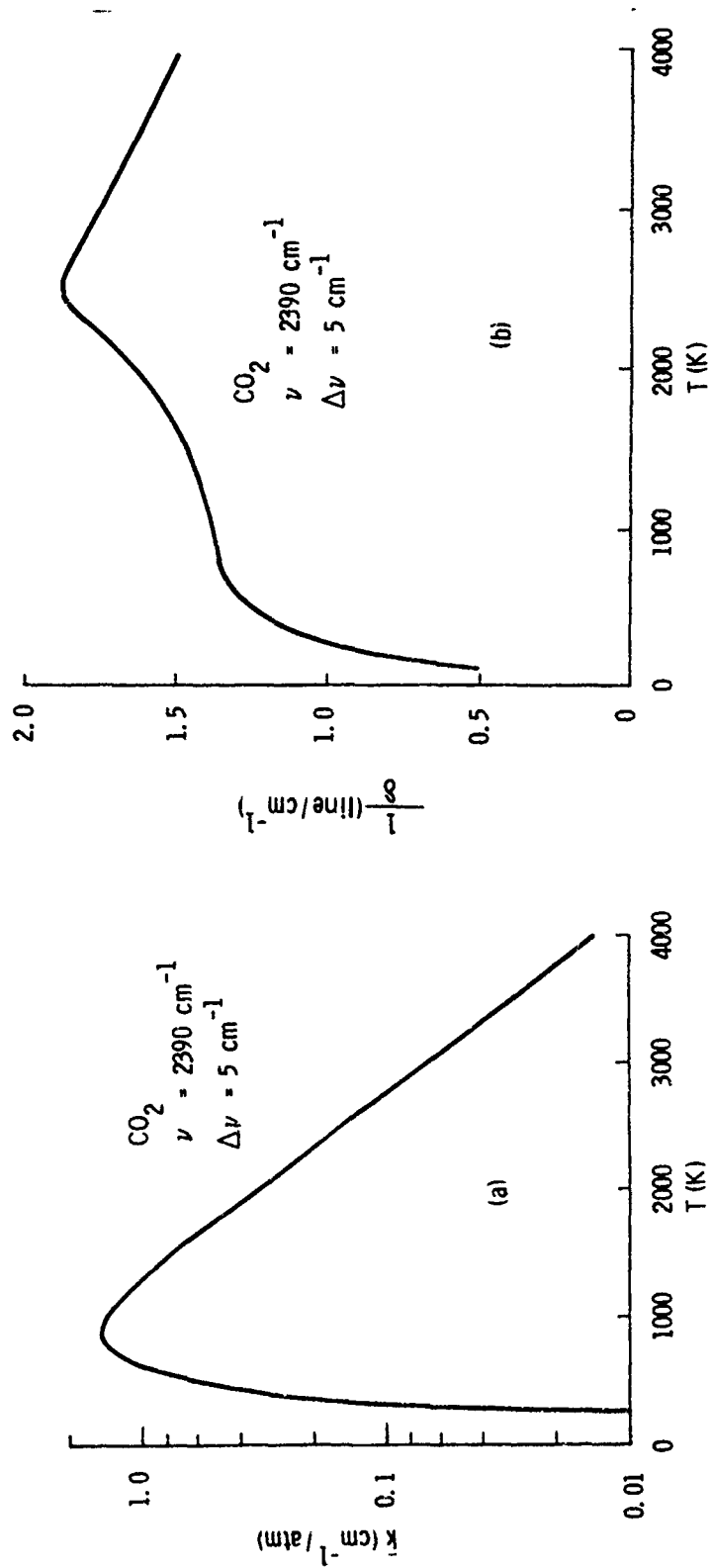


Fig. 6. Band Model Parameters for CO₂. (a) Absorption Parameter; (b) Line Density Parameter.

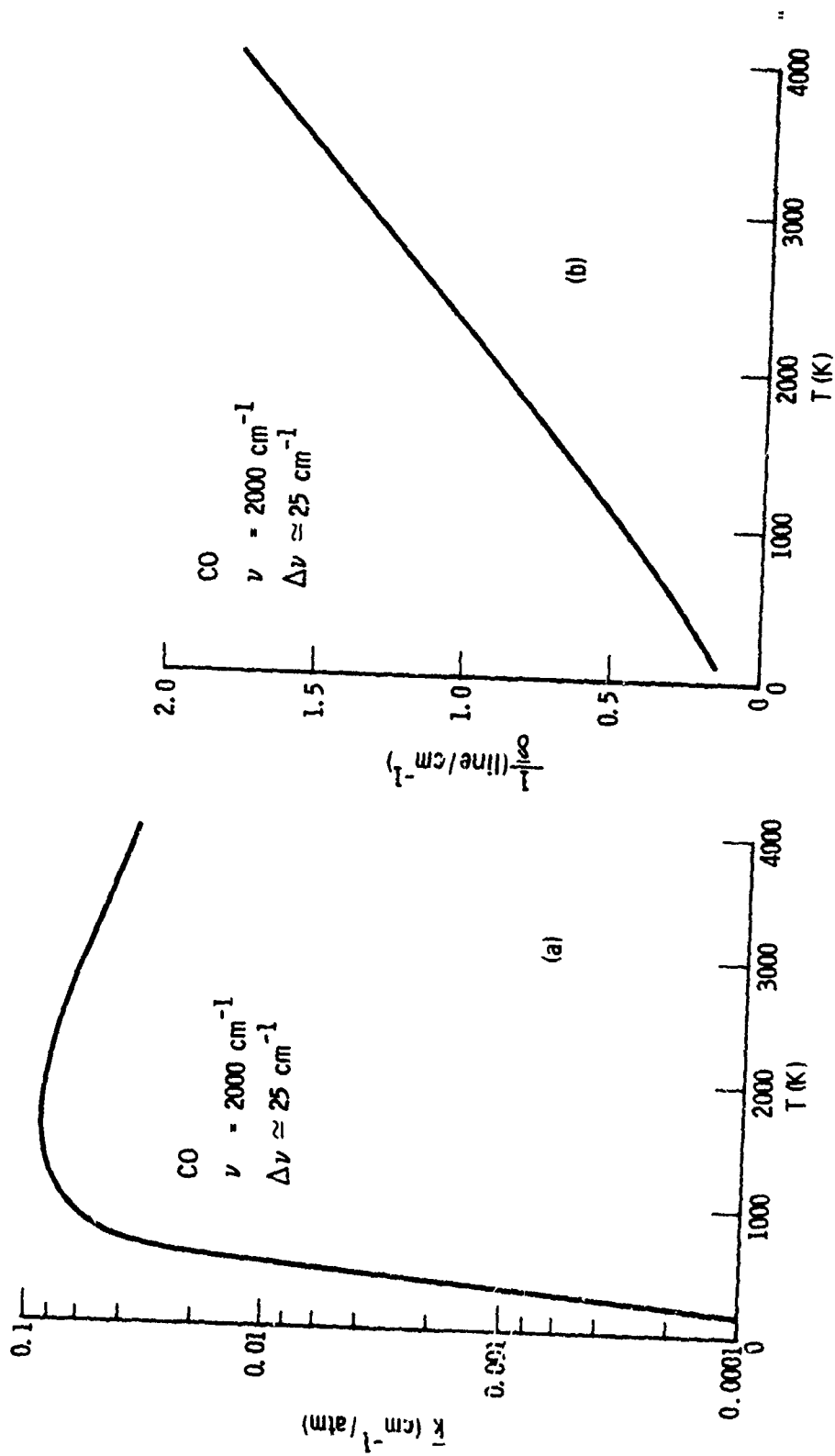


Fig. 7. Band Model Parameters for CO. (a) Absorption Parameter; (b) Line Density Parameter.

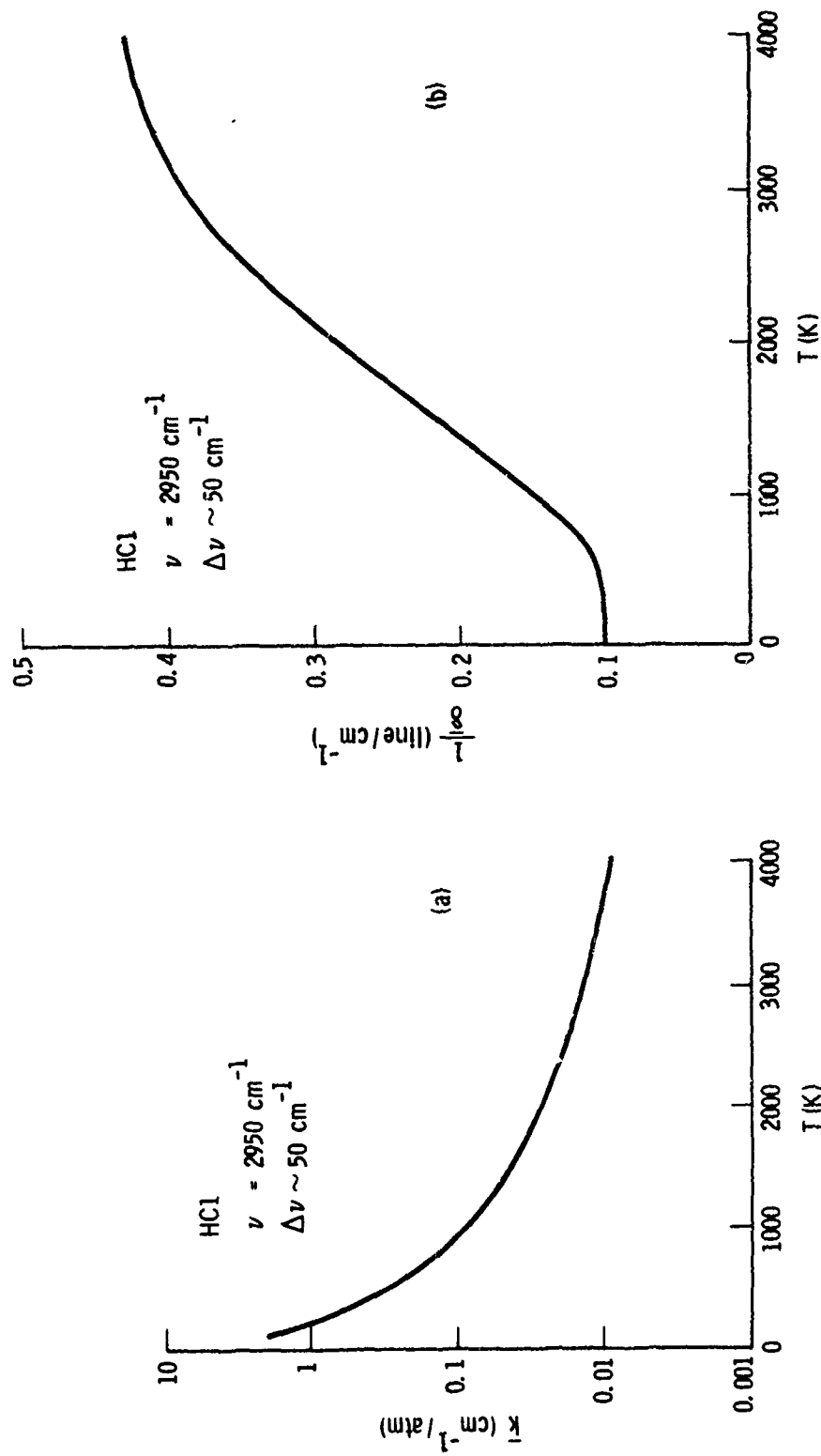


Fig. 8. Band Model Parameters for HCl. (a) Absorption Parameter; (b) Line Density Parameter.

Table 2. Linewidth Band Model Parameter.

Species	$\bar{\nu}(\text{cm}^{-1})$	$\gamma_0(\text{cm}^{-1}/\text{atm})$	α_1	α_2	α_3
CO	2000	0.06	0	1.00	28
CO ₂	2390	0.0876	0.111	0.778	44
HCl	2950	0.05	3.0	1.00	36.5
H ₂ O	3985	0.0739	6.53	1.00	18

Pressure Broadened Line Width

$$\bar{\gamma}_L = \gamma_0 P \left[\alpha_1 c \left(\frac{273}{T} \right) + c \sqrt{\frac{273}{T}} + \alpha_2 (1 - c) \sqrt{\frac{273}{T}} \right]$$

Doppler Line Width

$$\bar{\gamma}_D = 3.56817 \times 10^{-7} \bar{\nu} \sqrt{\frac{T}{\alpha_3}}$$

With the index of refraction and size distribution data, standard Mie theory algorithms were used to generate the absorption cross section σ_a , the total scattering cross section σ_s , and the differential scattering cross section $d\sigma_s(\theta)/d\Omega$. These results are given in Section 3.2.3. The absorption parameter α , the total scattering parameter β , and the scattering phase function $p(\Omega)$ required by the single-scattering band model were then obtained according to the formulas of Section 2.1. The total particle density N_p required for this calculation was either treated as a parametric variable, or computed from typical mass or mole fraction loading levels. These levels are discussed later in Section 4. The Appendix treats the conversion from one measure of particle loading to another.

3.2.1 Refractive Index

The application example of Section 4.1 required the index of refraction of Al_2O_3 at $2.51 \mu\text{m}$ and at a characteristic plume temperature of $\sim 1000\text{K}$. According to the data compilation of Whitson,¹² the index for these conditions for pure Al_2O_3 is $n \approx 1.7$ and $\kappa \approx 6 \times 10^{-7}$ (the complex index is $m = n - i\kappa$). The imaginary component of this index (κ) is much too small to explain the observed optical effects of Al_2O_3 in plumes. A tentative value of $m = 2.0 - 0.0018i$ is used here. This value was obtained for samples of Al_2O_3 actually used as burn stability additives in propellant mixtures.¹³ The increased value of κ provides an improved correlation with the observed radiation of Al_2O_3 in plumes, but is still judged somewhat low. In the present analysis, arbitrary imaginary values of 0.01 and 0.05 were also used. These increased values can be rationalized by noting that even a slight amount of contamination coating a small particle can dramatically increase its

12. M. E. Whitson, Handbook of the Infrared Optical Properties of Al_2O_3 , Carbon, M_2O_3 , and ZrO_2 , TR-0075(5548)-2, The Aerospace Corporation, El Segundo, Calif., 4 June 1975.

13. T. D. McCay, U. S. Air Force Rocket Propulsion Laboratory, Edwards Air Force Base, Calif., private communication, 1980.

emissivity (by increasing the effective value of κ).¹⁴

The example application involving carbon (Section 4.2) requires the refractive index at $3.39\mu\text{m}$ and $\sim 2000\text{K}$. The value used here is $n = 2$ and $\kappa = 1.0$.^{12, 15} Owing to experimental uncertainty and ignorance of the type of carbon, the imaginary part of this index may range from ~ 0.4 to 1.5 .

The optical constants for ZrO_2 are not well known in the spectral region of interest and for the characteristic temperatures of plumes. The principle data available are those of Dowling and Randall¹⁶ where n and κ were determined between 4.55 and $25\mu\text{m}$ at 300 and 573K . The data between 4.55 and $5.00\mu\text{m}$ were averaged to obtain

$n \approx 1.45$	$\kappa \approx .144$	at 300K
$n \approx 1.39$	$\kappa \approx .074$	at 573K .

By linear extrapolation on the n -data, the values

$n \approx 1.2$	at 1300K
$n \approx 1.0$	at 2000K

-
14. A. B. Pluchino, "Emissivity Spectra of Composite Microscopic Particles," *Applied Optics*, 20, 531-533 (1981).
 15. G. N. Freeman, C. B. Ludwig, W. Malkmus, and R. Reed, Development and Validation of Standardized Infrared Radiation Model (SIRRM): Gas/Particle Radiation Transfer Model, AFRPL-TR-79-55, U.S. Air Force Rocket Propulsion Laboratory, Edwards Air Force Base, Calif., October 1979.
 16. Particles of C, MgO, Al₂O₃, and ZrO₂ at Elevated Temperatures, AFRPL-TR-77-4, U. S. Air Force Rocket Propulsion Edwards Air Force Base, Calif., April 1977.

were obtained. These temperature values are the characteristic temperatures of the plumes for two cases considered in Section 4.3. A semilog extrapolation was made to obtain

$$\begin{aligned} \kappa &\approx .01 && \text{at } 1300\text{K} \\ \kappa &\approx .0025 && \text{at } 2000\text{K} \end{aligned}$$

These n and κ were used for all the spectral bandpasses. This assumption is partly justified by the fact that the emissivity and absorptance data compiled by Whitson¹² are reasonably constant between 2 and 5 μm .

A summary of the refractive index data used in this work is given in Table 3. All told, the quality of these data is quite crude and they should not be taken as definitive values. They are, however, judged adequate to display the qualitative features desired in this work. The index for ZrO_2 , for example, represents a particle type in which the primary optical property is scattering. Little absorption or emission is effected. The index for Al_2C_3 also represents a scattering particle, although with the increased values for κ , it can contribute significantly to absorption and emission. The index for carbon, on the other hand, represents a particle type in which absorption and emission are at least as important as scattering.

3.2.2 Size Distributions

The size distribution used for Al_2O_3 and ZrO_2 is a bimodal, modified gamma function distribution described by

$$f(r) = a_1 r^{\alpha_1} e^{-\beta_1 r^{\gamma_1}} + a_2 r^{\alpha_2} e^{-\beta_2 r^{\gamma_2}}$$

Table 3. Particle Index of Refraction.

Particle	λ (μm)	T(K)	n	κ	Reference
Al_2O_3	2.51	2000	2.0	0.0018 0.01 0.05	12, 13
Carbon	3.39	2000	2.6	1.0	12
ZrO_2	2-5	1300	1.2	0.01	12, 16
		2000	1.0	0.0025	

$$\begin{array}{ll}
 a_1 = 4.45 \times 10^9 & a_2 = 20.8 \\
 \alpha_1 = 4 & \alpha_2 = 3 \\
 \beta_1 = 35.92 & \beta_2 = 6 \\
 \gamma_1 = 1/2 & \gamma_2 = 1
 \end{array}$$

The unit of r is μm and the unit of $f(r)$ is μm^{-1} . $f(r)$ is normalized by $\int_0^\infty f(r) dr = 1$. The distribution is shown in Fig. 9. The distribution is based on data obtained from "small" rocket motors¹⁷ and is characterized by a large submicron peak about $r = 0.05 \mu\text{m}$ and a smaller micron-size peak about $r = 0.5 \mu\text{m}$. Although the submicron peak is an order of magnitude larger than the micron-size peak, the scattering parameters are completely dominated by the large-particle distribution. This result is discussed in the next section.

The large peak of this distribution is reasonably consistent with the mean size of Al_2O_3 particles deduced by McCay et al¹⁸ from visible laser scattering and attenuation measurements. They obtained radii values of 0.30 to 0.35 μm . The distribution is also consistent with some of their results for ZrO_2 . In two of their tests, they obtained mean radii of $\sim 0.5 \mu\text{m}$. In a third test, they obtained results which could be interpreted as indicating particle radii of 0.9 to 1.5 μm . In order to simulate this latter size, a monodisperse distribution with $r = 1.0 \mu\text{m}$ was also used in the present work.

-
17. R. Dawbarn, Aluminum Oxide Produced by Solid Rocket Motors, Proc. USAF/NASA Int. Spacecraft Contamination Conf., USAF Academy, Colorado Springs, March 1978.
 18. T. D. McCay, W. C. Mundy, D. M. Mann, and G. S. Meserve, Laser Mie Scattering Measurements of Particle Size in Solid Rocket Motor Exhausts, JANNAF 12th Plume Technology Meeting, USAF Academy, Colorado Springs, 18-20 November 1980.

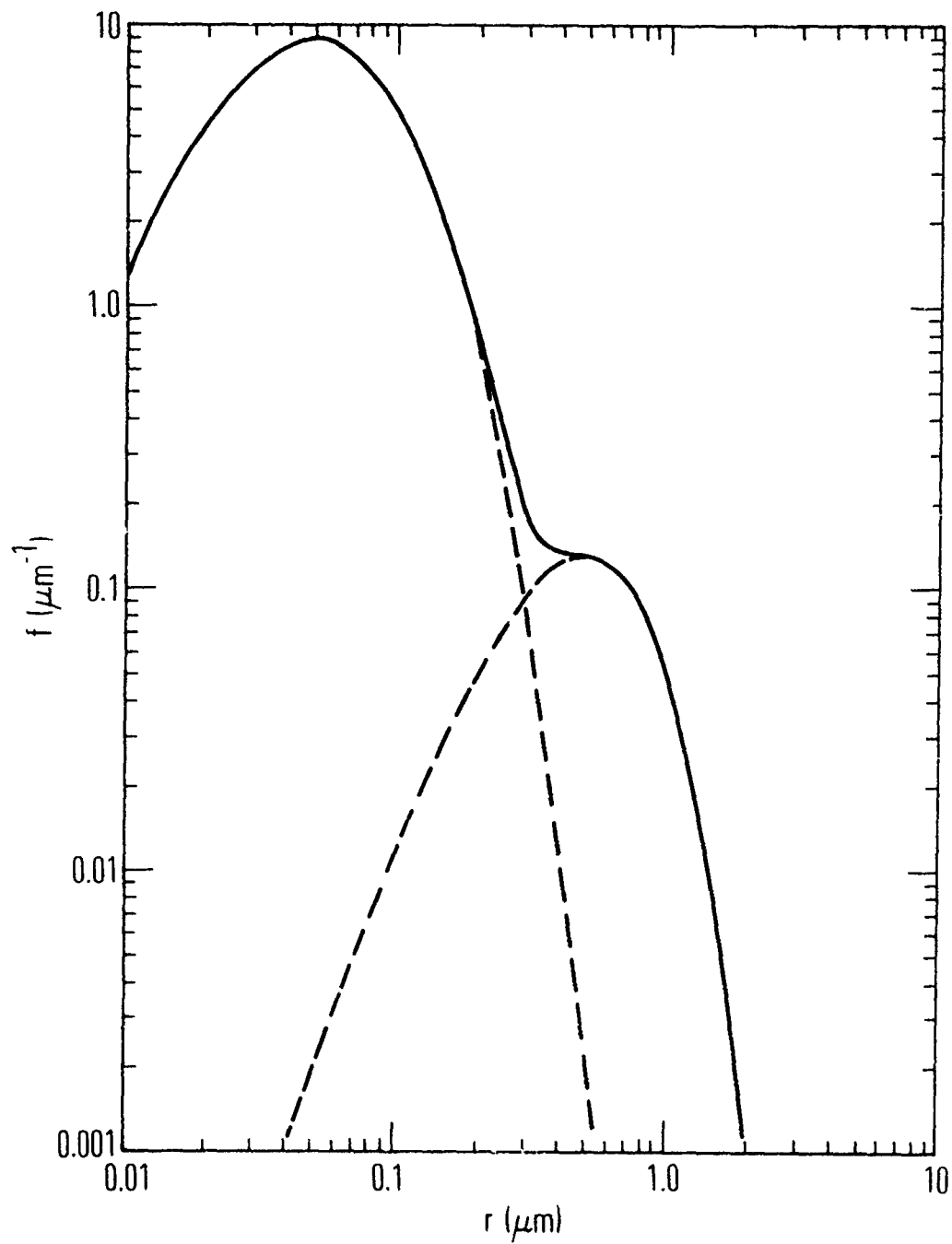


Fig. 9. Bimodal Particle Size Distribution for Al_2O_3 and ZrO_2 .

The particle size distribution used for carbon is described by the modified gamma function

$$f(r) = a r^{\alpha} e^{-\beta r^{\gamma}}$$

with $a = 1.89 \times 10^{11}$, $\alpha = 4$, $\beta = 32.57$ and $\gamma = 1/3$. The unit of r is μm and of f is μm^{-1} . The distribution peaks at $r = 0.05 \mu\text{m}$ and falls to a value more than two orders of magnitude smaller than the peak value at $r = 0.5 \mu\text{m}$. The function is shown in Fig. 10.

3.2.3 Scattering Cross Sections

Standard Mie scattering calculations¹⁹ were made for the index of refractions and size distributions just discussed. The results for Al_2O_3 are shown in Table 4 and Fig. 11. These results are the sum of the results for each mode of the distribution of Fig. 9 taken separately, but, for all practical purposes, are essentially equal to the results for the large size mode alone. The small size mode, although roughly two orders of magnitude larger in peak number density, contributes only about one percent to the total. The total cross sections are tabulated in Table 4 for the three assumed values of the imaginary part of the refractive index. The variation of κ has little effect on the total scattering cross section σ_s and almost no effect on the extinction cross section $\sigma_e = \sigma_s + \sigma_a$. The absorption cross section σ_a is, as would be expected, quite sensitive to variation in κ . Except possibly for the largest κ , σ_s is much larger than σ_a and indicates that particle scattering should be more important than particle emission and absorption in determining the role of particles in the plume. The differential scattering cross section $d\sigma_s(\theta)/d\Omega$ is shown in Fig. 11. In the important forward diffraction peak, the cross section is relatively insensitive to the magnitude of κ .

19. D. Deirmendjian, Electromagnetic Scattering on Spherical Polydispersions, Elsevier Publishing Co., Inc., New York, N. Y., 1969.

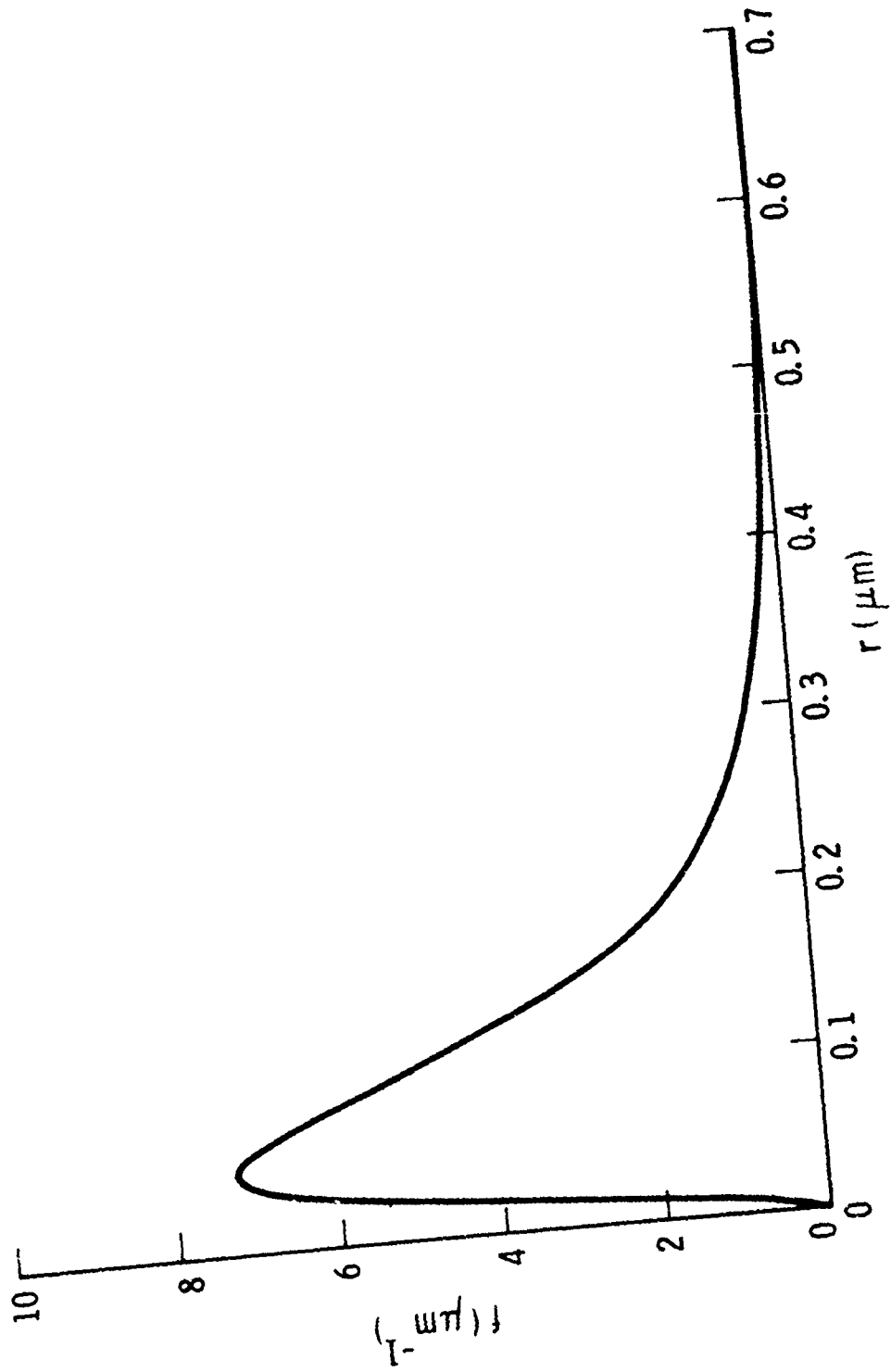


Fig. 10. Particle Size Distribution for Carbon.

Table 4. Al_2O_3 Scattering Cross Sections.

κ	$\sigma_a(\text{cm}^2)$	$\sigma_s(\text{cm}^2)$	$\sigma_e(\text{cm}^2)$	ω
0.0018	6.39(-10)	5.86(-8)	5.92(-8)	0.989
0.01	3.20(-9)	5.58(-8)	5.90(-8)	0.946
0.05	1.16(-8)	4.62(-8)	5.78(-8)	0.799

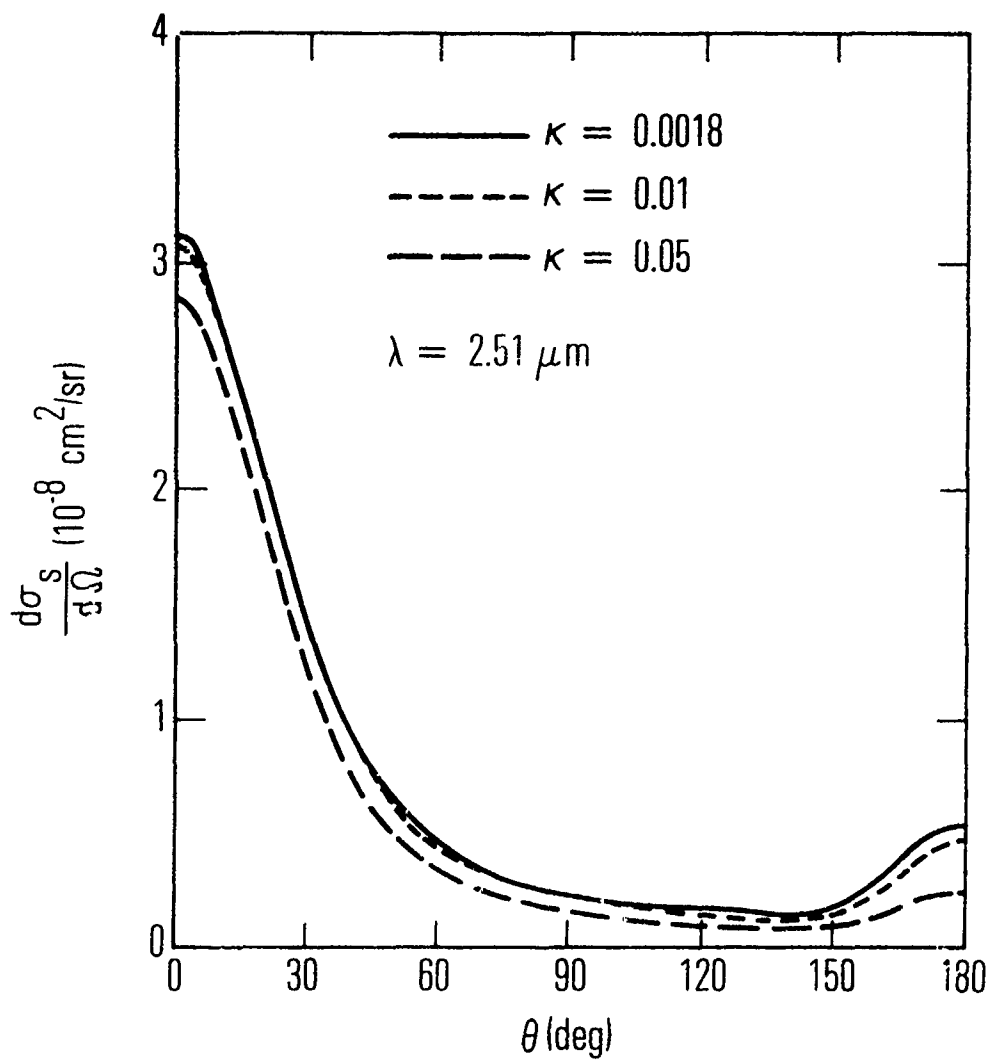


Fig. 11. Differential Scattering Cross Section for Al_2O_3 .

The results for carbon are shown in Fig. 12. The scattering is not as sharply peaked in the forward direction as it is for Al_2O_3 because the mean size of the particles (Fig. 10) is much smaller. The result $\sigma_s \approx \sigma_a$ indicates that scattering should be comparable with emission and absorption in determining radiation transfer in carbon bearing plumes.

The total scattering cross sections derived for the selected n and κ and for the two size distributions for ZrO_2 are tabulated in Table 5. The differential scattering cross sections are plotted in Figs. 13 and 14. The principle features of these results are: 1) the increasing forward scattering as λ decreases; 2) the strong minima between 100 and 130° scattering angle for the monodisperse distribution at $\lambda = 2.51 \mu\text{m}$; and 3) most importantly, the extreme smallness of σ_s and $d\sigma_s/d\Omega$ for the high temperature case. This latter result (Fig. 14) is a consequence of using $n \approx 1$ for this case. Consequently, at 2000K , radiation transport is dominated by the emission and absorption properties of the particulates and is essentially independent of their scattering effects.

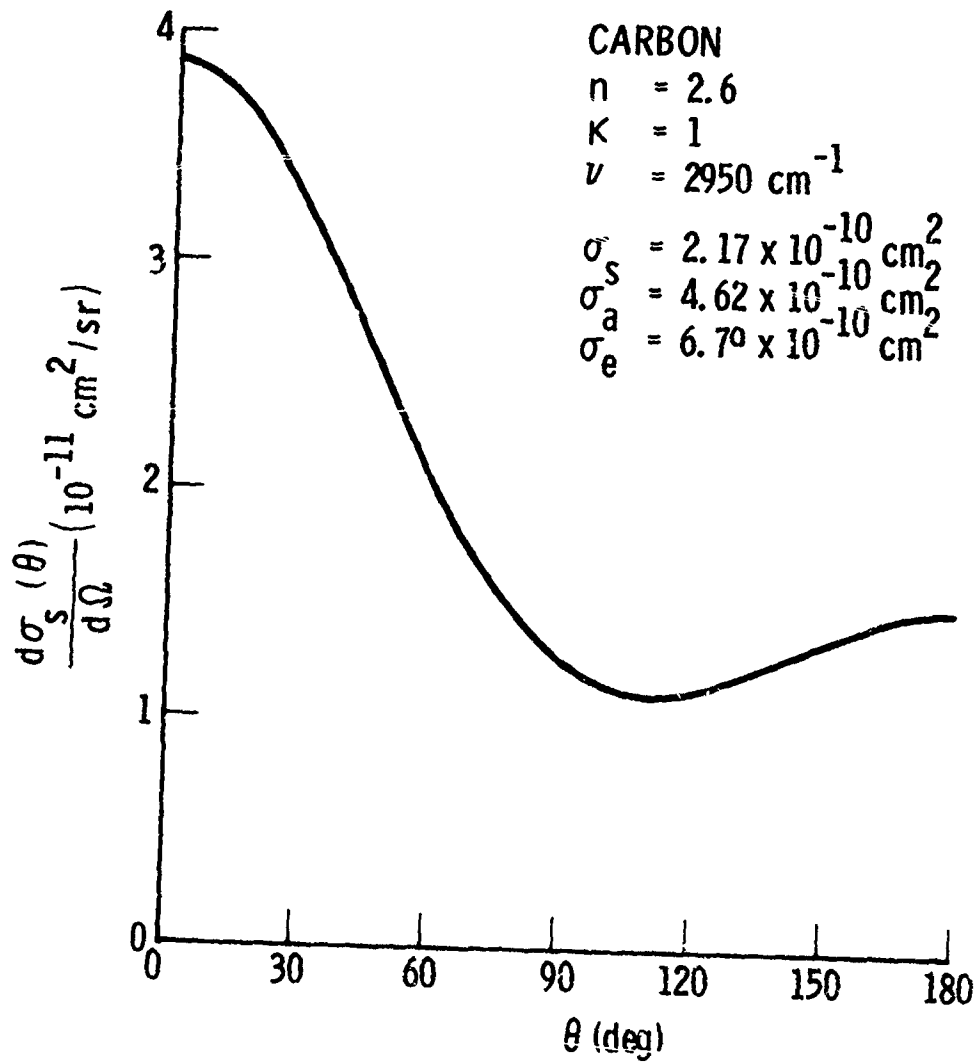


Fig. 12. Differential Scattering Cross Section for Carbon.

Table 5. ZrO_2 Scattering Cross Sections. Upper entries are for bimodal distribution; lower entries are for monodisperse distribution.

λ (μm)	Low-Temperature Model				High-Temperature Model			
	σ_a (cm^2)	σ_s (cm^2)	σ_e (cm^2)	ω	σ_a (cm^2)	σ_s (cm^2)	σ_e (cm^2)	ω
5.00	6.44(-10)	1.62(-9)	2.27(-9)	.714	1.46(-10)	2.36(-13)	1.46(-10)	.00162
	1.14(-9)	2.21(-9)	3.35(-9)	.660	2.63(-10)	3.23(-13)	2.63(-10)	.00123
4.18	7.9 (-10)	2.58(-9)	3.37(-9)	.766	1.74(-10)	3.72(-13)	1.74(-10)	.00213
	1.39(-9)	3.60(-9)	5.00(-9)	.720	3.13(-10)	5.30(-13)	3.14(-10)	.00169
3.38	-	-	-	-	2.14(-10)	6.23(-13)	2.15(-10)	.00290
	-	-	-	-	3.86(-10)	8.97(-13)	3.87(-10)	.00232
2.51	1.41(-9)	8.41(-9)	9.82(-9)	.856	2.90(-10)	1.27(-12)	2.91(-10)	.00440
	2.56(-9)	1.34(-8)	1.59(-8)	.843	5.23(-10)	1.84(-12)	5.25(-10)	.00350

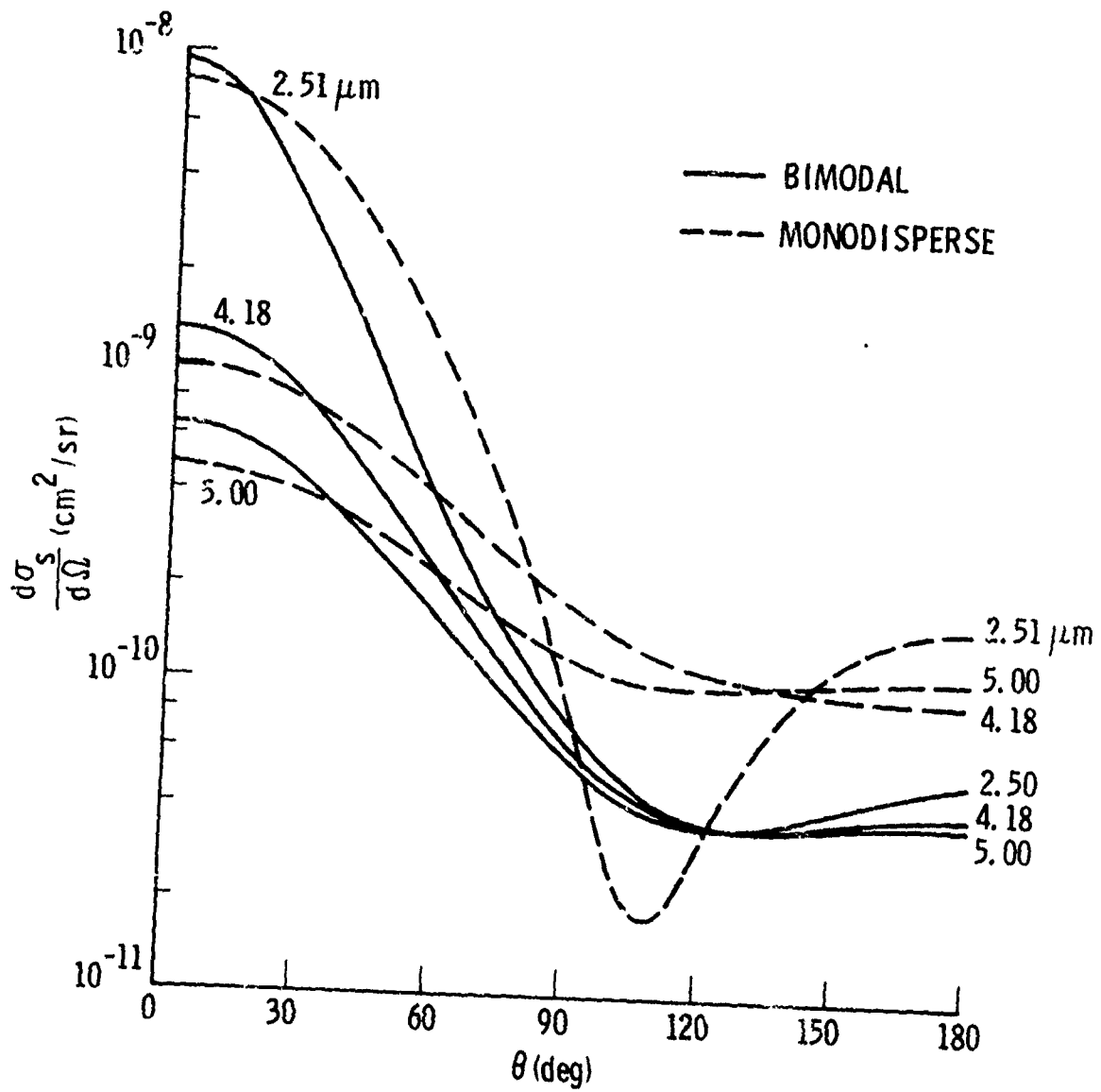


Fig. 13. Differential Scattering Cross Section for 1300K ZrO_2 .

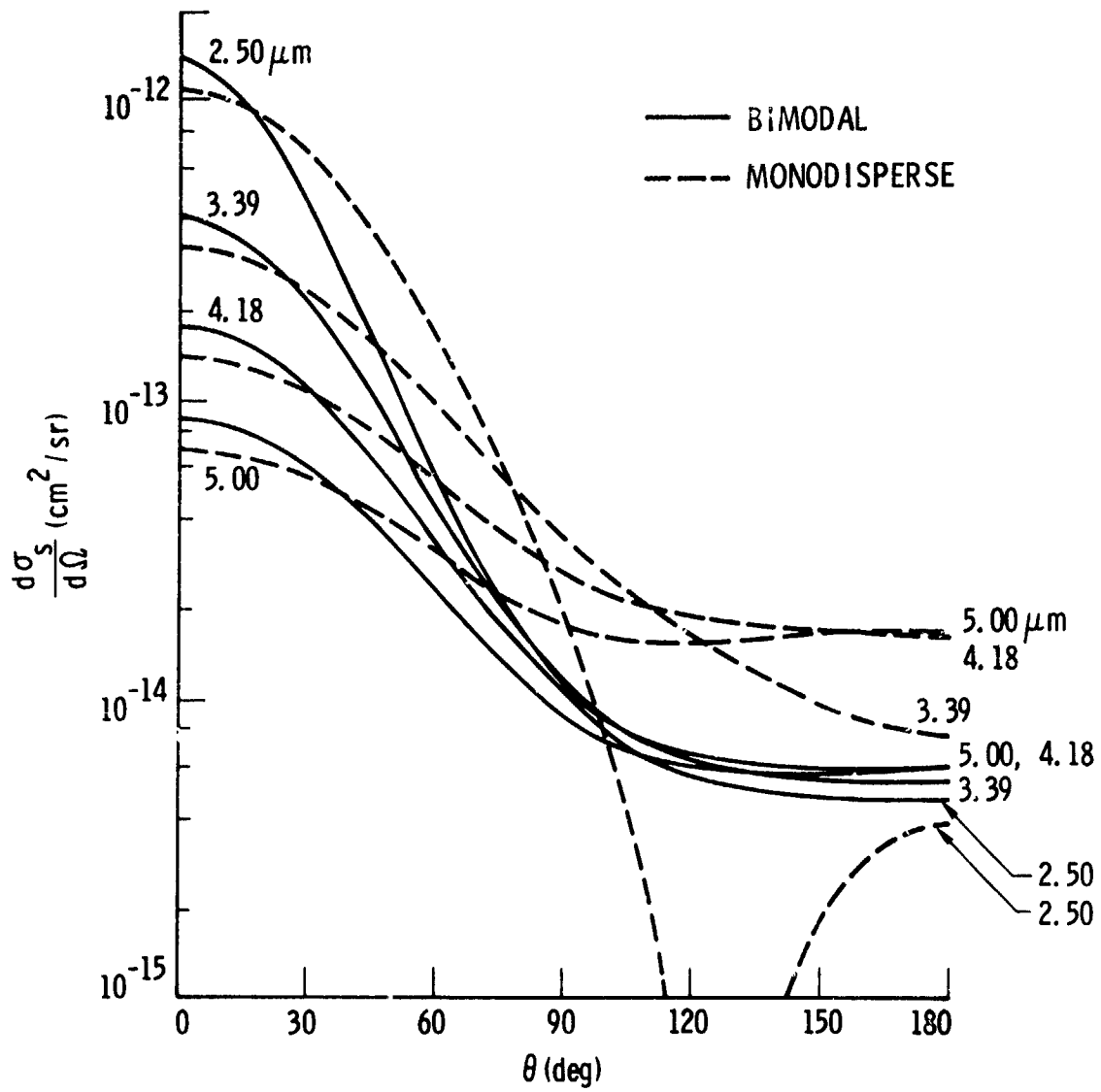


Fig. 14. Differential Scattering Cross Section for 2000K ZrO₂.

4. EXAMPLE APPLICATIONS

The analysis procedure outlined in Section 1.2 is here applied to the exhaust plumes of three model tactical motors. The first exhaust model is representative of a minimum smoke solid propellant (MSP) and considers H_2O/Al_2O_3 as the gas/particle phases. The second is representative of an advanced liquid propellant (ALP in which HCl/Carbon is the gas/particle pair. The third is representative of a reduced smoke propellant (RSP) and considers the pairing of ZrO_2 with several gas species.

4.1 Minimum Smoke Propellant (MSP) (H_2O/Al_2O_3) Plume

The analysis for this model is divided into two sections. In the first (Section 4.1.1), a preliminary MSP model is considered, and analyses are presented on numerical accuracy, relative magnitudes of various emission and extinction mechanisms to the total E/A profiles, and compatibility between the codes EAPROF and EMABIC. In the second (Section 4.1.2), the final analysis for this example is presented.

4.1.1 Preliminary Analysis

The active gas is H_2O and the particulate is Al_2O_3 . The optical properties of these species and the spectral band ($2.51 \mu m$) have been discussed in Section 3. For all of these preliminary analyses, the particle scattering data for $\kappa = 0.0018$ were used. The radial pTc data for the plume model are given in Fig. 15. The gas concentrations are constant in radius. The particles were assumed to be in thermal equilibrium with the gas so that the particle temperature profile was the same as the gas temperature profile. A flat concentration profile of $N_p = 10^5/cm^3$ was used. The total scattering cross section (Table 4) is $\sigma_s = 5.86 \times 10^{-8} cm^2$ and the plume diameter is $D = 20 cm$. The extinction by scattering through the plume is then

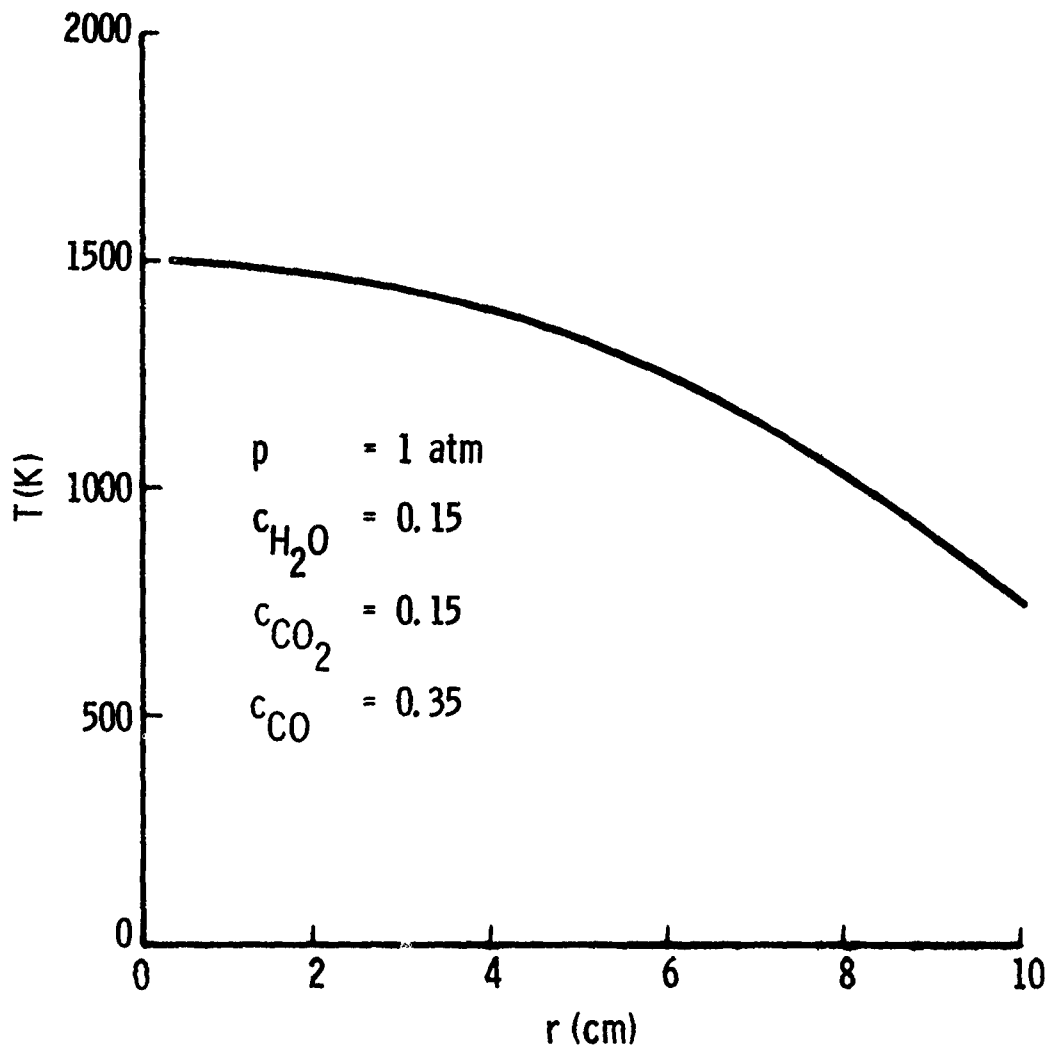


Fig. 15. Radial pTc Profiles for the Preliminary MSP Plume Model.

$1 - \tau = 1 - \exp(-N_p \sigma_e D) \approx 0.11$. This loading level is thus about the maximum that can be tolerated within the single-scattering assumption.

The nozzle exit plane was modeled as a flat disc at $T = 1500\text{K}$ and with emissivity $\epsilon = 1$. The scanning plane was 5cm below the exit plane, and the plume extended 30cm beyond the scanning plane. Except for the radial temperature profile, the plume was uniform. The Lorentz line profile and Curtis-Godson approximation were used. The number of radial and transverse zones was 10. Path integrations along scattering lines of sight were done with the path divided into 10 equal length segments (regardless of the length of the path).

With these input conditions, numerical experiments were carried out with the code EAPROF to determine how fine an angle integration grid is required to obtain accurate scattering results. The angle variables θ and ϕ are defined in Fig. 4. In the course of debugging the code, a heuristic grid of 11 points was used for the scattering angle θ . (See Eq. 14). This grid is illustrated in Fig. 16. The function plotted is the weighting function $\sin\theta p(\theta)$ that occurs in the scattering integral

$$\int_0^{2\pi} \int_0^{\pi} p(\theta) N(\theta, \phi) \sin\theta d\theta d\phi .$$

The 11 points were chosen to give a good coverage of this function with a higher concentration of points in the region where the function is largest. The results of the first numerical experiment confirmed the suitability of this grid, and, consequently, this grid is used throughout the remainder of the analyses. In this analysis, the azimuthal integration grid was held at $N_\phi = 4$ ($\phi = 0, 90^\circ, 180^\circ, 270^\circ$) while calculations were made with the following scattering angle grids

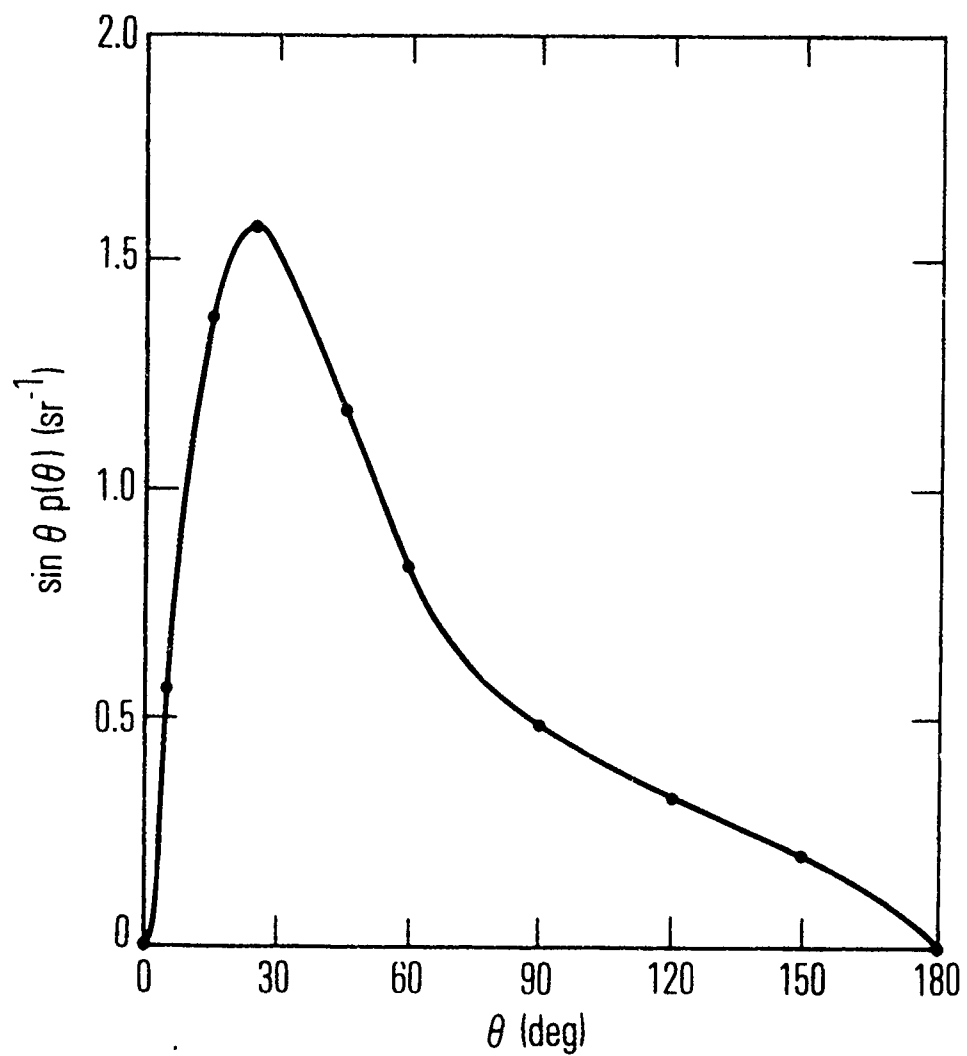


Fig. 16. Coverage of the Scattering Integral Weighting Function by the 11-Point Scattering Angle Grid.

θ (deg)	N_θ
0, 30, 60, ..., 180	7
0, 15, 30, ..., 180	13
0, 10, 20, ..., 180	19
0, 5, 10, ..., 180	37

The results are shown in Fig. 17a. \bar{N}_s is the scattering component of the total emission at the transverse position $z = 0$. That is, \bar{N}_s is the total radiance minus the radiance value that occurs for the gas-only case. The dashed lines show the bounds of the true value of \bar{N}_s , and the dot shows the result obtained with the 11-point scattering angle grid. The 11 point gives a value of \bar{N}_s that is only 1.7% higher than the most probable true value (the center of the dashed band). The corresponding value of total radiance is less than 1% too high.

In the second numerical experiment, the scattering angle integration was held constant at $N_\theta = 11$ while calculations were made with the azimuth angle grids

$$\phi = 0, \frac{2\pi}{N_\phi}, 2\left(\frac{2\pi}{N_\phi}\right), 3\left(\frac{2\pi}{N_\phi}\right), \dots, (N_\phi - 1)\left(\frac{2\pi}{N_\phi}\right)$$

$$N_\phi = 4, 8, 16, 32.$$

The results are shown in Fig. 17b. Again, the dashed lines indicate bounds on the true value of \bar{N}_s . The value obtained for $N_\phi = 16$ is 4.6% too low. Combined with the 1.7% too-high error obtained by using $N_\theta = 11$, the total error estimated for \bar{N}_s is $\sim 3\%$ too low. The error in the total radiance is about one half this value. This order of magnitude of error is adequate for this work, and $N_\phi = 16$ is employed in the remainder of the work.

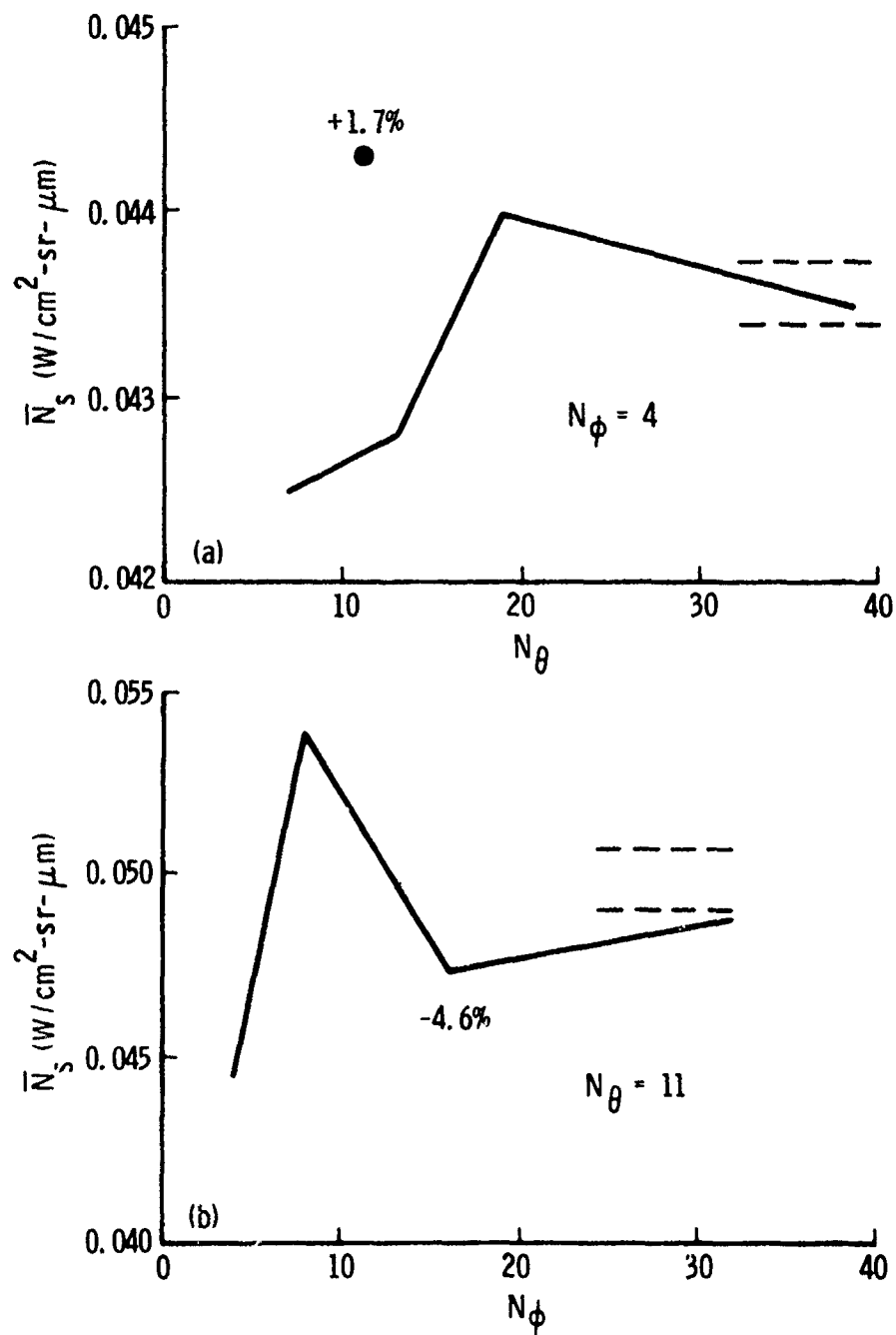


Fig. 17. Convergence of Scattered Radiance with Angle Integration Grid Resolution. (a) Convergence with Scattering Angle Increment; (b) Convergence with Azimuth Angle Increment.

In a second analysis, an investigation was made to determine the contributions of various effects to the total radiance and extintance of the plume. The results are shown in Tables 6 and 7 and Figs. 18 and 19. In the tables, z is the transverse position of the line of sight, the first column is the radiance (or, in Table 7, the extintance) for the gas-only case. In the second column, the particles are allowed to absorb and emit, but not scatter. The third column shows the full results for absorbing, emitting and scattering particles, but with the nozzle exit plane emission turned off. Finally, the column labeled TOTAL shows the result obtained from all effects. The last four columns show the contributions (obtained by various subtractions) of the gas, particle emission/absorption, particle scattering, and nozzle radiation, respectively.

For radiance, the principal contributors are emission from the gas, and scattering of exit plane radiation into the line of sight. Emission/absorption by the particles is only $\sim 1\%$ of that due to gas, and scattering of radiation other than nozzle radiation is even smaller. Note that the scattering contribution is negative for $z \leq 4$ cm. Presumably, the net effect along the longer lines of sight that obtain for small z is that more radiation is scattered out of the line of sight by particles than is scattered in.

For extintance, gas is again the major attenuator. Scattering of radiation out of the line of sight is the second most important effect and is essentially equal to the gas attenuation. Absorption by particles is two orders of magnitude down from the gas and scattering contributions.

The third major preliminary analysis was a check for consistency between the plume signature code EAPROF and the diagnostic code EMABIC for gas-only plumes. The gas and calculation conditions previously defined were used to predict gas only E/A spectra using both EAPROF and EMABIC. The results of the comparison are shown in Table 8. The percent difference between the radiance profiles varies from ~ 0.3 at $z = 0$ to ~ 13 at $z = 9$ cm (where the radiance is approaching zero). These differences can be attributed to the slightly different quadrature routines used in the two codes. The differences in transmittance are even smaller (less than ~ 0.2 percent).

Table 6. Plume Radiance Contributions for Preliminary Minimum Smoke Propellant Plume Model.

z (cm)	\bar{N} (W/cm^2 -sr- μm)				Partial Contributions (W/cm^2 -sr- μm)				
	(1)		(2)		(3)		(4)		Nozzle
	$e = 0$	$\beta = 0$	$e = 0$	$\beta = 0$	$e = 0$	$\beta = 0$	TOTAL	Gas	
0	0.1102	0.1119	0.1113	0.1113	0.1576	0.1102	0.0017	- 0.0006	0.0463
1	0.1085	0.1102	0.1096	0.1096	0.1558	0.1085	0.0017	- 0.0006	0.0462
2	0.1035	0.1050	0.1046	0.1046	0.1494	0.1035	0.0015	- 0.0004	0.0448
3	0.09513	0.09646	0.09616	0.09616	0.1407	0.09513	0.0013	- 0.0003	0.0445
4	0.08345	0.08454	0.08452	0.08452	0.1267	0.08345	0.0011	- 0.00002	0.0422
5	0.06887	0.06871	0.06995	0.06995	0.1061	0.06887	0.00084	0.0002	0.0362
6	0.05234	0.05292	0.05349	0.05349	0.08633	0.05234	0.00058	0.0006	0.0328
7	0.03544	0.03579	0.03649	0.03649	0.06517	0.03544	0.00035	0.0007	0.0287
8	0.02039	0.02057	0.02130	0.02130	0.04106	0.02039	0.00018	0.0007	0.0198
9	0.008871	0.008937	0.009508	0.009508	0.02266	0.008871	0.00007	0.0006	0.0132
10	0	0	0	0	0	0	0	0	0

- (1) Gas only
- (2) Gas plus particle absorbance
- (3) Gas plus particle absorbance and scattering
- (4) Gas plus particles plus nozzle

Table 7. Plume Extinctance Contributions for Preliminary Minimum
Smoke Propellant Plume Model.

z (cm)	Extinctance				TOTAL	Gas	Partial Contributions			
	$\epsilon = 0$ $\beta = 0$ $\alpha = 0$	$\epsilon = 0$ $\beta = 0$	$\epsilon = 0$	TOTAL			Particles			Nozzle
							Abs	Scat		
0	0.1245	0.1256	0.2223	0.2223	0.1245	0.0011	0.0967	0		
1	0.1243	0.1254	0.2217	0.2217	0.1243	0.0011	0.0963			
2	0.1235	0.1246	0.2196	0.2196	0.1235	0.0011	0.0950			
3	0.1221	0.1231	0.2159	0.2159	0.1221	0.0010	0.0928			
4	0.1198	0.1209	0.2104	0.2104	0.1198	0.0011	0.0895			
5	0.1165	0.1175	0.2027	0.2027	0.1165	0.0010	0.0852			
6	0.1118	0.1127	0.1921	0.1921	0.1118	0.0009	0.0794			
7	0.1049	0.1057	0.1775	0.1775	0.1049	0.0008	0.0718			
8	0.09467	0.09538	0.1568	0.1568	0.09467	0.0007	0.0614			
9	0.07717	0.07769	0.1236	0.1236	0.07717	0.0005	0.0459			
10	0	0	0	0	0	0	0	0		

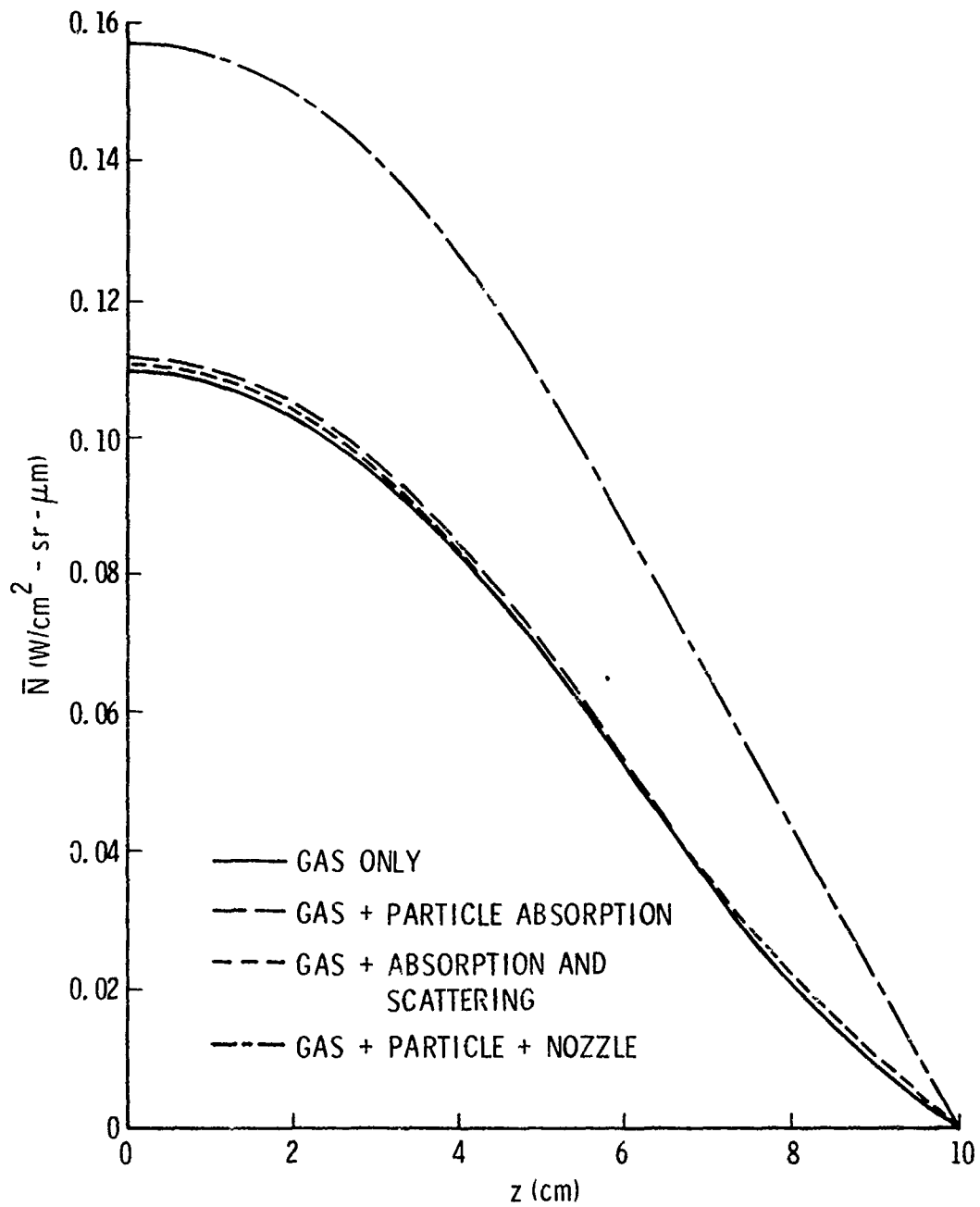


Fig. 18. Plume Radiance Contributions for the Preliminary MSP Plume Model.

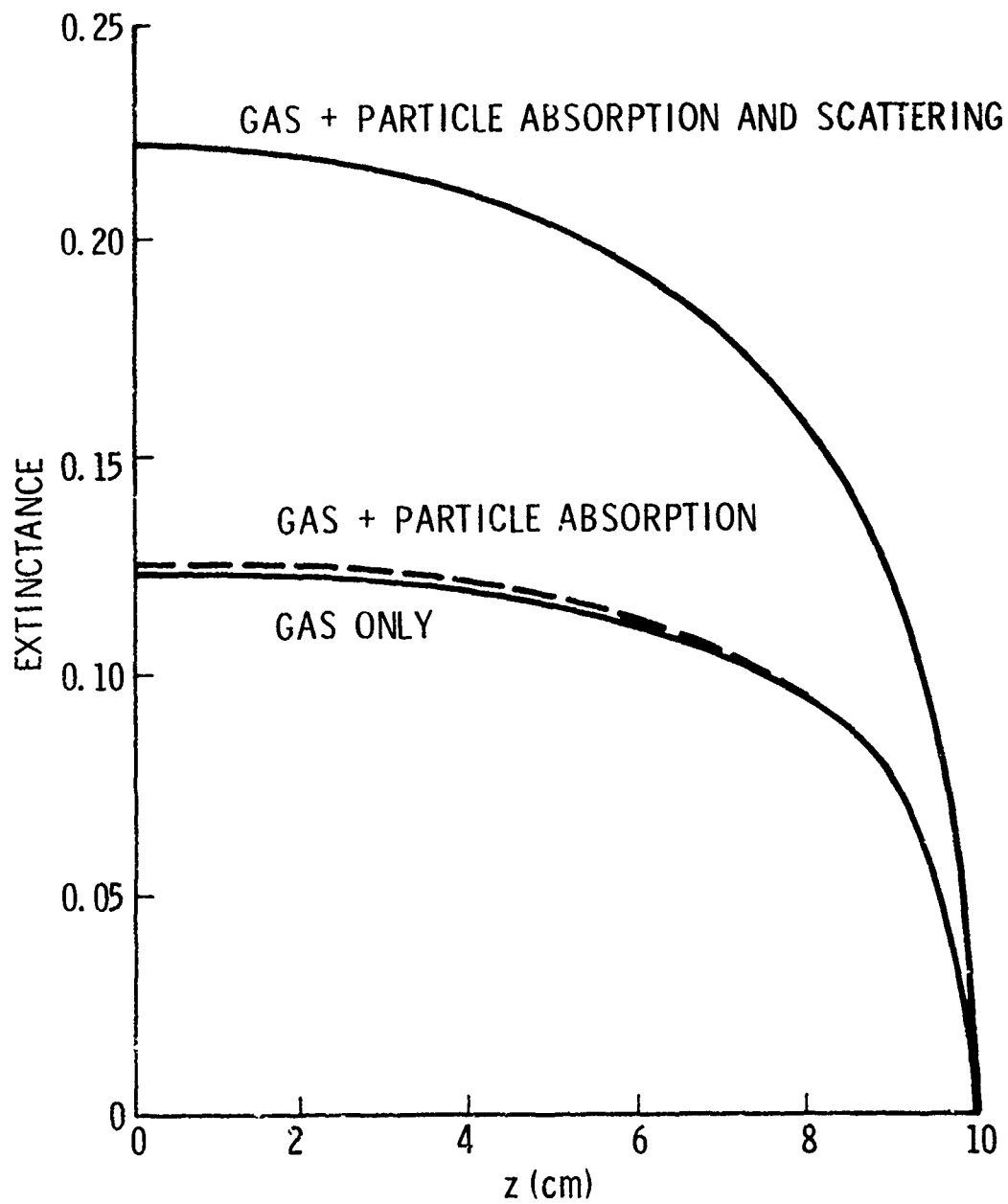


Fig. 19. Plume Extinctance Contributions for the Preliminary MSP Plume Model.

Table 8. Comparison of E/A Profiles Generated with EMABIC and EAPROF for the Preliminary Minimum Smoke Propellant Plume Model.

z(cm)	$\bar{N}(10^{-5}w/cm^2 \cdot sr \cdot cm^{-1})$			$\bar{\tau}$		
	EMABIC	EAPROF	%	EMABIC	EAPROF	%
0	7.574	7.551	.3	.9001	.9000	.01
1	7.457	7.426	.4	.9001	.8997	.02
2	7.103	7.060	.6	.9000	.8998	.02
3	6.516	6.453	1.0	.9000	.8997	.03
4	5.705	5.620	1.5	.9003	.8999	.04
5	4.707	4.596	2.4	.9012	.9007	.06
6	3.584	3.454	3.6	.9032	.9026	.07
7	2.447	2.309	5.6	.9070	.9063	.08
8	1.426	1.308	8.3	.9138	.9126	.13
9	0.647	0.560	13.4	.9273	.9255	.19
10	0	0	—	1	1	0

The transverse E/A profiles of Table 1 were then inverted using the iterative Abel inversion mode of EMABIC. Figures 20 and 21 show the convergence characteristics for the inversions. Figure 20 is the rms difference between successively retrieved temperature profiles as a function of number of iterations. Figure 21 shows the similar result for concentration. The significant feature of these curves is that EMABIC inverts the profiles generated by EAPROF as stably as it inverts its own transverse profiles. The accuracy of the retrievals is shown in Table 9 and Fig. 22. In Table 9, the retrieved temperature and concentration profiles from the 20th iteration are compared with the true values. The differences from the true values are plotted in Fig. 22. Except near the plume boundary, the accuracy of retrieval for either the EMABIC or EAPROF profiles is quite satisfactory. The inversion for the EMABIC profiles is somewhat better, as would be expected.

These results justify the procedure of generating E/A profiles with EAPROF and inverting with EMABIC. We can be assured that the difference of retrieved profiles from true profiles for cases involving particles are indeed caused only by particle effects.

4.1.2 Final Analysis

The final analysis for the MSP plume model employed the pTc profiles of Fig. 23. The only change from the preliminary analysis is in the temperature profile near $r = R$. The nozzle exit plane temperature and emissivity were changed from the preliminary analysis values to $T = 800\text{K}$ and $\epsilon = 0.75$. Particle concentration was treated as a parameter of the analysis and varied from zero up to the value used in the preliminary analysis ($N_p = 10^5/\text{cm}^3$). The scanning plane is $L_1 = 3\text{ cm}$ from the exit plane and the plume end plane is $L_2 = 57\text{ cm}$ beyond the scanning plane. This value for L_2 was determined as explained in Section 2.2 with an axial temperature fall-off of $d\tau/dz = -5\text{K/cm}$. All other conditions were the same as for the preliminary analysis.

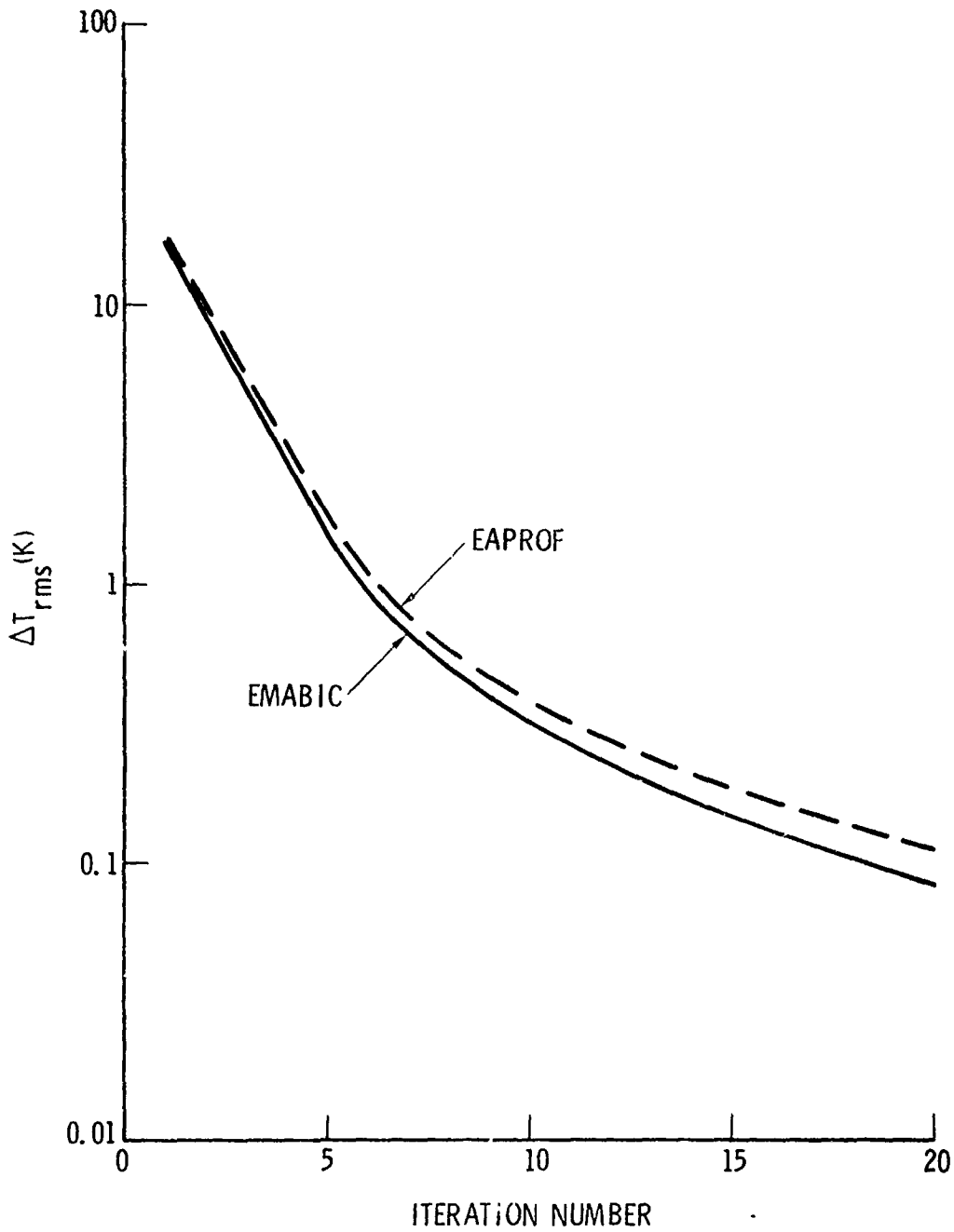


Fig. 20. Temperature Convergence for Inversion of E/A Profiles Generated with EMABIC and EAPROF for the Preliminary MSP Plume Model.

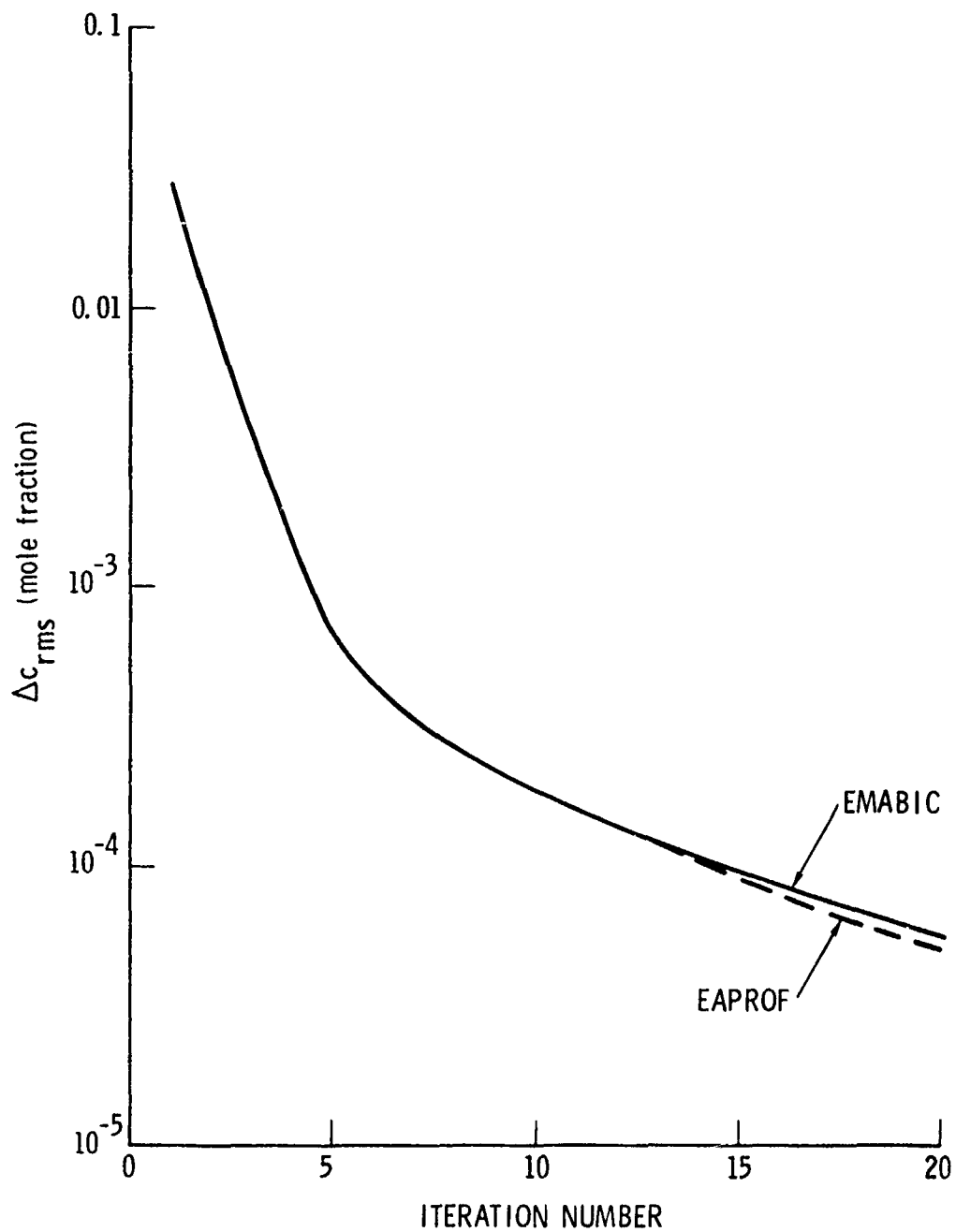


Fig. 21. Concentration Convergence for Inversion of E/A Profiles Generated with EMABIC and EAPROF for the Preliminary MSP Plume Model.

Table 9. Comparison of Retrieved and True Radial Profiles for the Preliminary Minimum Smoke Propellant Plume Model.

Temperature Retrieval (K)					
z(cm)	True	EMABIC	Δ	EAPROF	Δ
0	1500	1500	0	1513	13
1	1493	1493	0	1505	12
2	1470	1471	1	1480	10
3	1433	1432	-1	1440	7
4	1380	1379	-1	1383	3
5	1313	1313	0	1314	1
6	1230	1228	-2	1225	-5
7	1133	1133	0	1127	-6
8	1020	1022	2	1012	-8
9	893	878	-15	860	-33
10	750	788	38	758	8

Concentration Retrieval (mole fraction)					
z(cm)	True	EMABIC	Δ	EAPROF	Δ
0	0.1500	.1500	0	.1482	-.0018
1	↓	.1500	0	.1494	-.0006
2		.1498	-.0002	.1501	.0001
3		.1502	.0002	.1499	-.0001
4		.1501	.0001	.1500	0
5		.1500	.0	.1496	-.0004
6		.1507	.0007	.1503	.0003
7		.1495	-.0005	.1478	-.0022
8		.1497	-.0003	.1486	-.0014
9		.1538	.0038	.1548	.0018
10		.1465	-.0035	.1451	-.0019

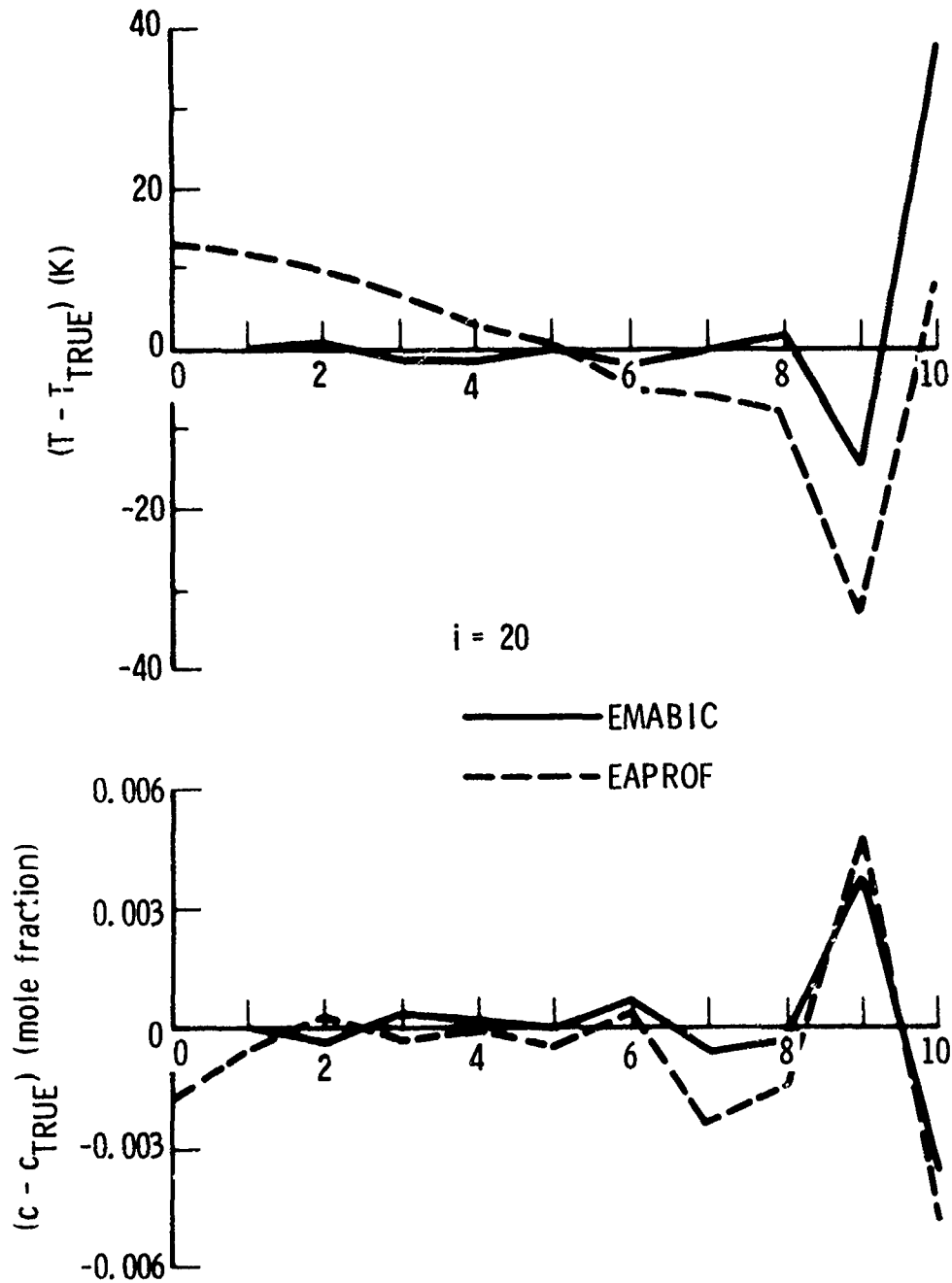


Fig. 22. Convergence Residuals for Inversion of c/A Profiles Generated with EMABIC and EAPROF for the Preliminary MSP Plume Model.

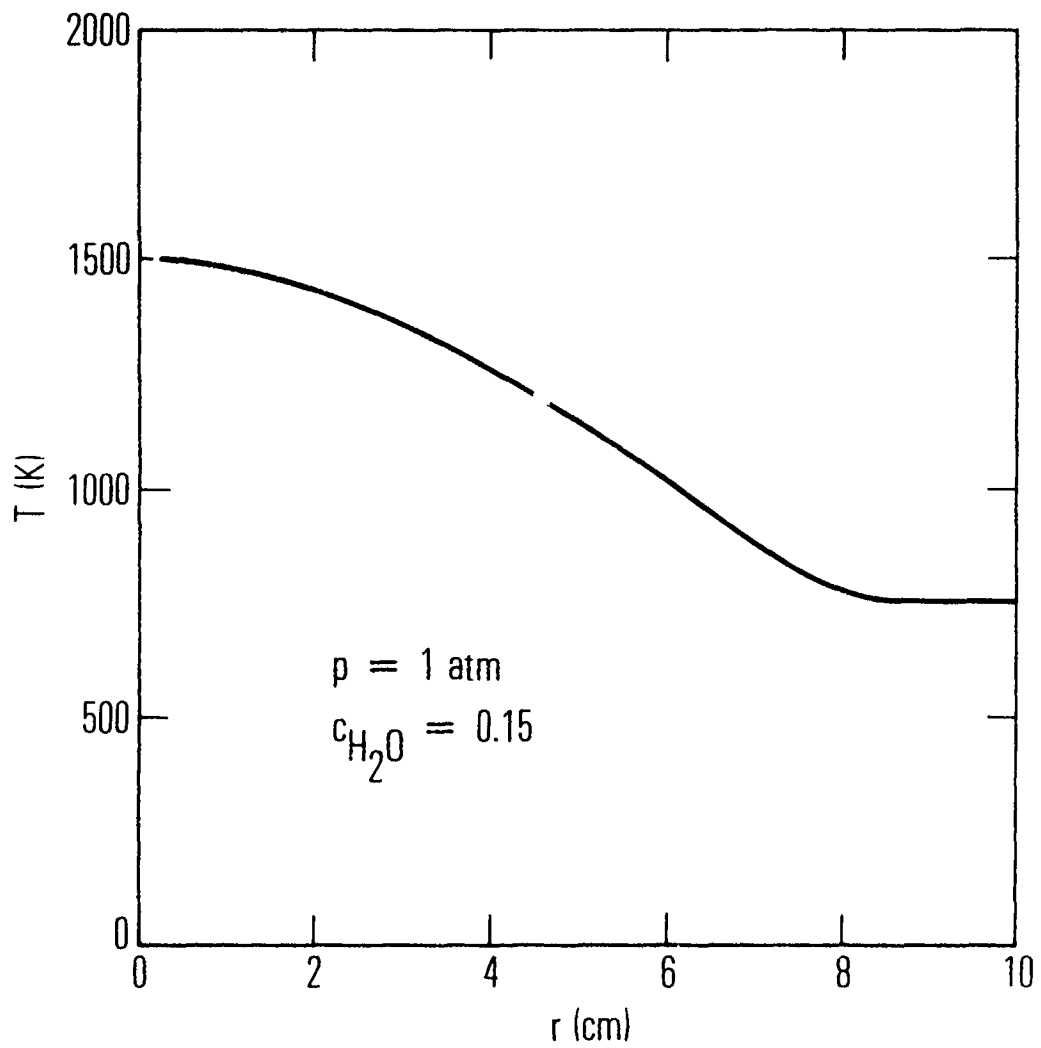


Fig. 23. Radial pTc Profiles for the MSP Plume Model.

For these conditions, transverse radiance/extinctance profiles were generated with κ and N_p as parameters. Example profiles for $\kappa = 0.01$ are shown in Figs. 24 and 25. It can be seen that the effect of particle concentration is much stronger on extinctance than on radiance. The variations of the centerline ($z = 0$) values of \bar{N} and $\bar{\tau}$ with particle concentration are shown in Fig. 26 and Table 10. The single curve for $1 - \bar{\tau}$ results for all three values of κ and is due to the near constancy of the total extinction cross section with κ . Radiance, on the other hand, displays a measurable variation with κ for N_p greater than $\sim 2 \times 10^4 / \text{cm}^3$.

A gas-only inversion of the transverse profiles was made with the code EMABIC. Where appropriate, all of the conditions used to compute the transverse profiles were carried over into the inversion (eg. line shape, number of zones, etc.). Inversion was performed in the iterative Abel inversion mode with no presmoothing. Convergence was deemed complete when the rms temperature and concentration differences between successively iterated profiles were less than 10K and 0.001, respectively. The number of iterations required to meet these criteria was 5 to 7. Example inversion results for $\kappa = 0.01$ are shown in Figs. 27 and 28. With increasing particle density, the temperature is increasingly underpredicted. The percentage errors of retrieval at the plume axis ($r = 0$) are shown in Table 11 and Figs. 29 and 30. Below $N_p \sim 10^3 / \text{cm}^3$, the error of retrieval is negligible. At the maximum loading level consistent with the single-scattering approximation (i.e., $N_p = 10^5 / \text{cm}^3$), the temperature is underpredicted by 15 to 20 percent ($\sim 250\text{K}$) and the retrieved concentration is more than 100 percent too high. These results are nearly independent of κ within the range of variation used. In order to keep the concentration error within acceptable bounds (say 10 percent), the particle loading level cannot exceed $\sim 10^4 / \text{cm}^3$.

The first-order, off-band correction procedure described in Section 1.2 was applied to the cases for $\kappa = 0.01$. The gas-only, particle-only, and gas-plus-particle radiance and transmittance profiles are shown in Figs. 31 and 32, respectively, for the loading value $N_p = 4 \times 10^4 / \text{cm}^3$.

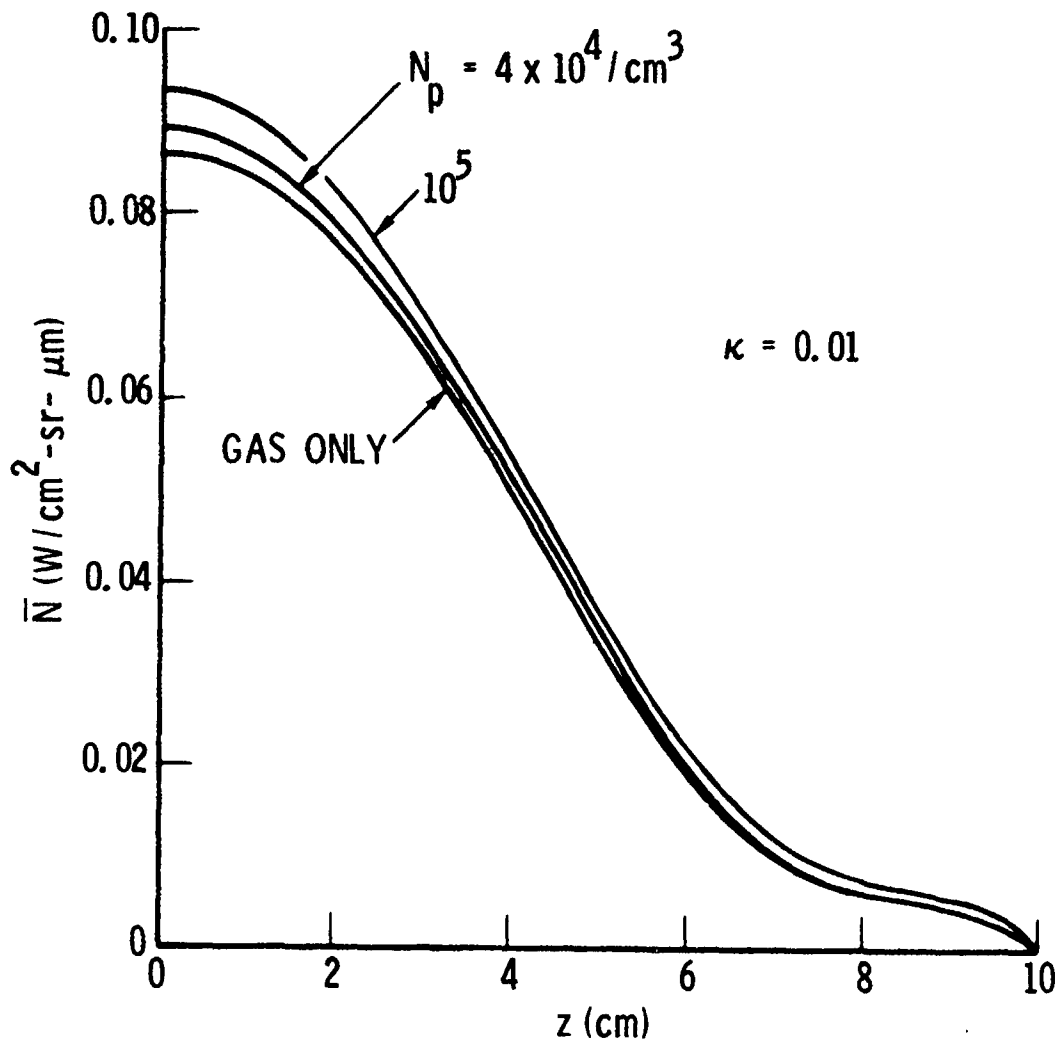


Fig. 24. Transverse Radiance Profiles for the MSP Plume Model.

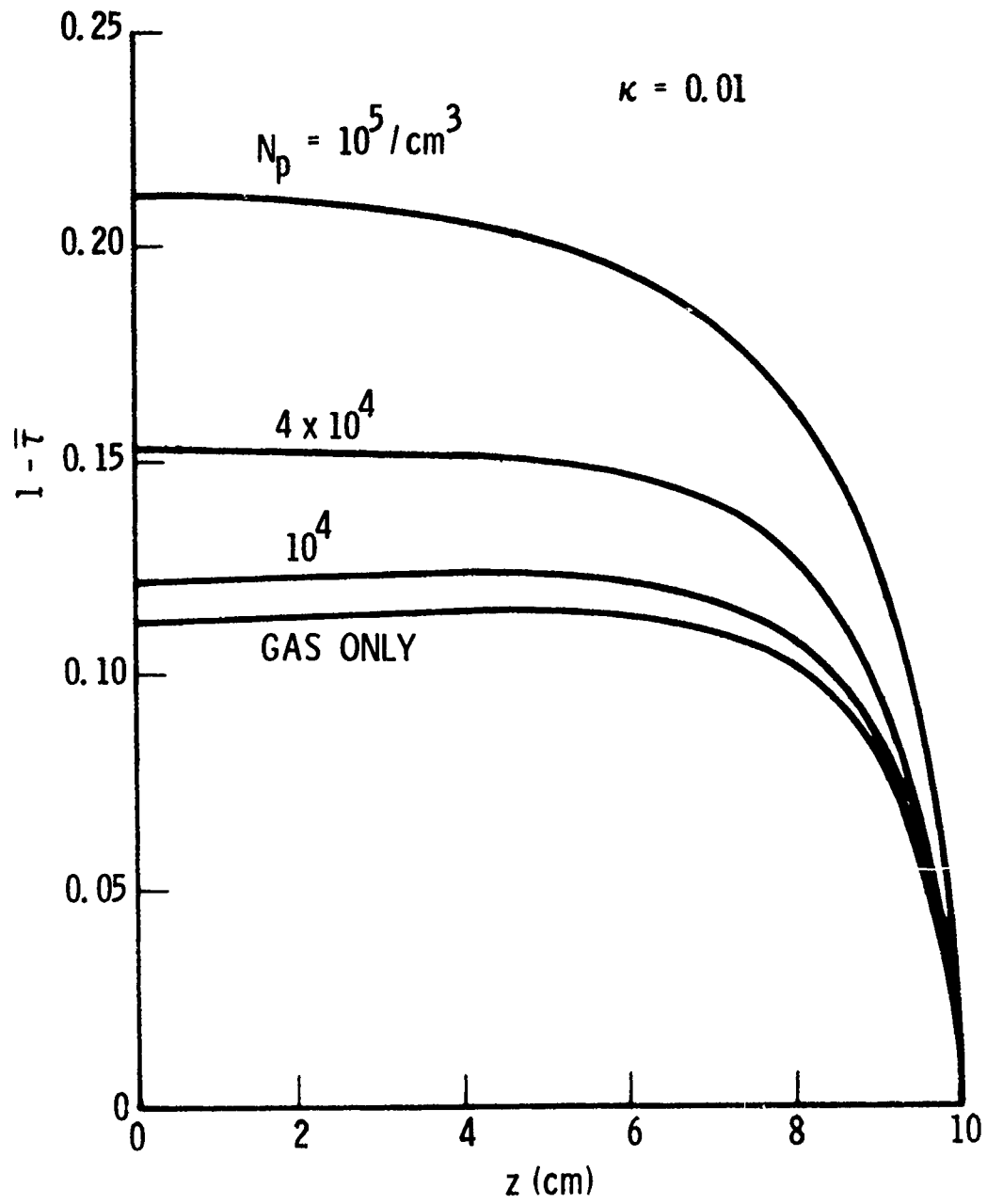


Fig. 25. Transverse Extinctance Profiles for the MSP Plume Model.

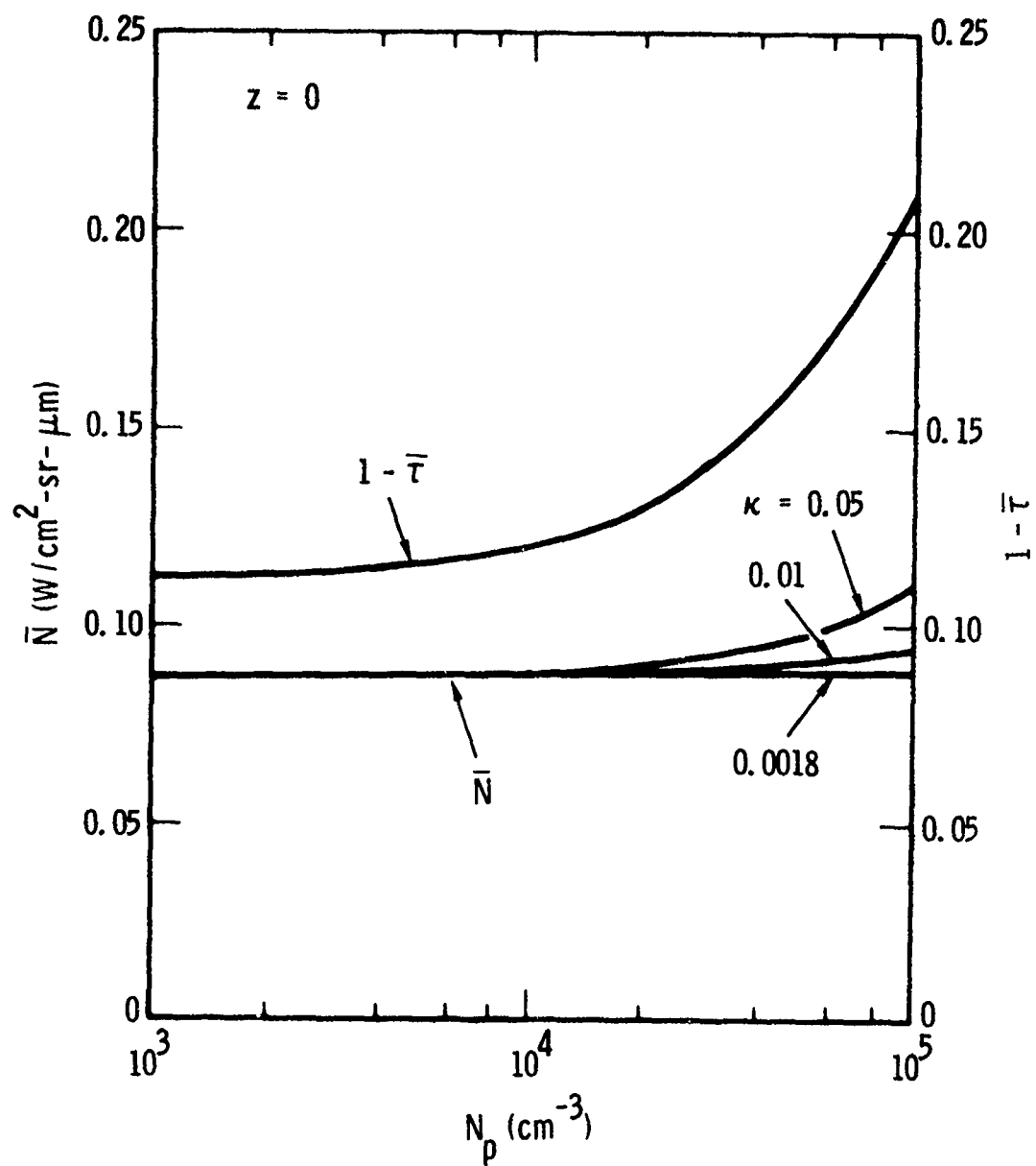


Fig. 26. Variation of Radiance and Extinctance at $z = 0$ with Particle Density for the MSP Plume Model.

Table 10. Variation of Radiance and Extinctance at $z=0$ with Particle Density for Minimum Smoke Propellant Plume Model.

N_p (cm^{-3})	$\bar{N}(W/\text{cm}^2\text{-sr-}\mu\text{m})$			$1 - \bar{\tau}$		
	$\kappa=0.0018$	$\kappa=0.01$	$\kappa=0.05$	$\kappa=0.0018$	$\kappa=0.01$	$\kappa=0.05$
0	.08726	.08726	.08726	.1120	.1120	.1120
100	.08727	.08727	.08729	.1121	.1121	.1121
400	.08727	.08729	.08736	.1125	.1124	.1124
1000	.08728	.08733	.08750	.1131	.1131	.1131
4000	.08734	.08754	.08820	.1162	.1162	.1161
10000	.08745	.08795	.08959	.1225	.1224	.1222
40000	.08801	.08999	.09649	.1531	.1530	.1522
100000	.08905	.09395	.1099	.2112	.2109	.2090

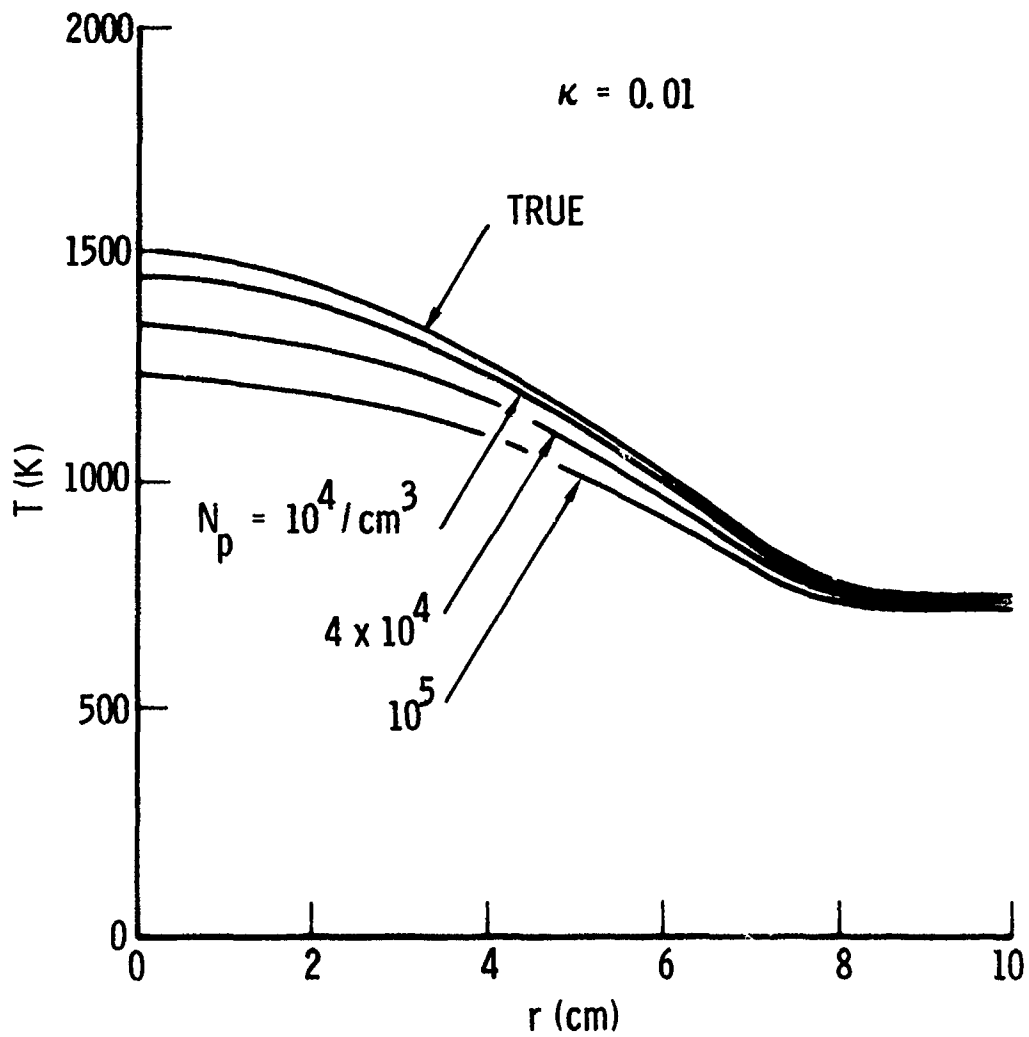


Fig. 27. Temperature Retrieval for the MSP Plume Model.

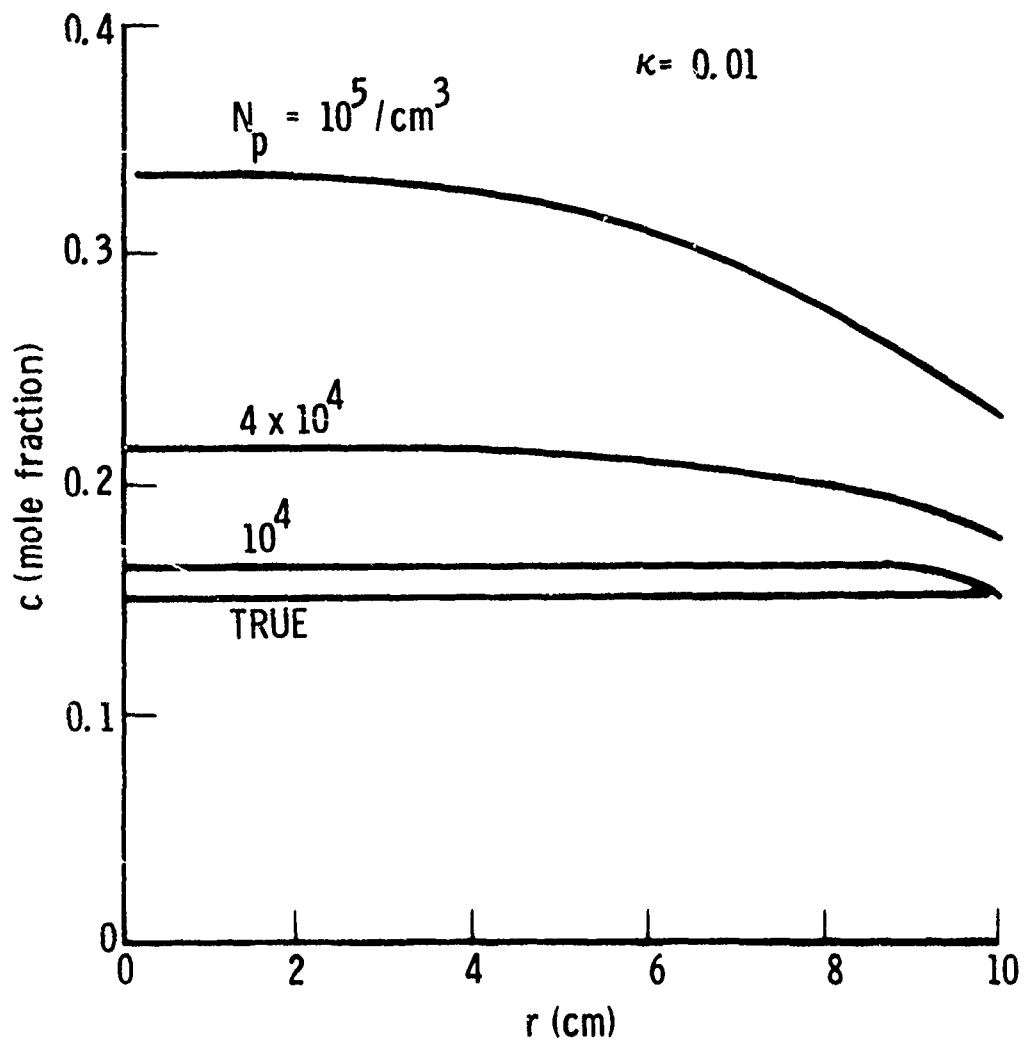


Fig. 28. Concentration Retrieval for the MSP Plume Model.

Table 11. Temperature and Gas Concentration Retrieval on Plume Axis for Minimum Smoke Propellant Plume Model.

N_p (cm^{-3})	$\kappa = 0.0018$		$\kappa = 0.01$		$\kappa = 0.05$	
	T($^{\circ}\text{K}$)	% Error	T($^{\circ}\text{K}$)	% Error	T($^{\circ}\text{K}$)	% Error
0	1506	0	1506	0	1506	0
100	1506	↓	1506	↓	1507	↓
400	1506	↓	1509	↓	1505	↓
1000	1503	↓	1503	↓	1504	↓
4000	1487	-1	1485	-1	1492	-0.5
10000	1451	-3	1454	-3	1463	-2.5
40000	1339	-11	1346	-10	1374	-8
100000	1218	-19	1235	-18	1289	-14

N_p (cm^{-3})	$\kappa = 0.0018$		$\kappa = 0.01$		$\kappa = 0.05$	
	c	% Error	c	% Error	c	% Error
0	.1501	0	.1501	0	.1501	0
100	.1501	↓	.1501	↓	.1501	↓
400	.1504	↓	.1494	↓	.1507	↓
1000	.1516	1	.1516	1	.1517	1
4000	.1558	4	.1562	4	.1567	4
10000	.1660	11	.1663	11	.1678	12
40000	.2175	45	.2202	47	.2253	50
1000000	.3306	120	.3354	124	.3473	132

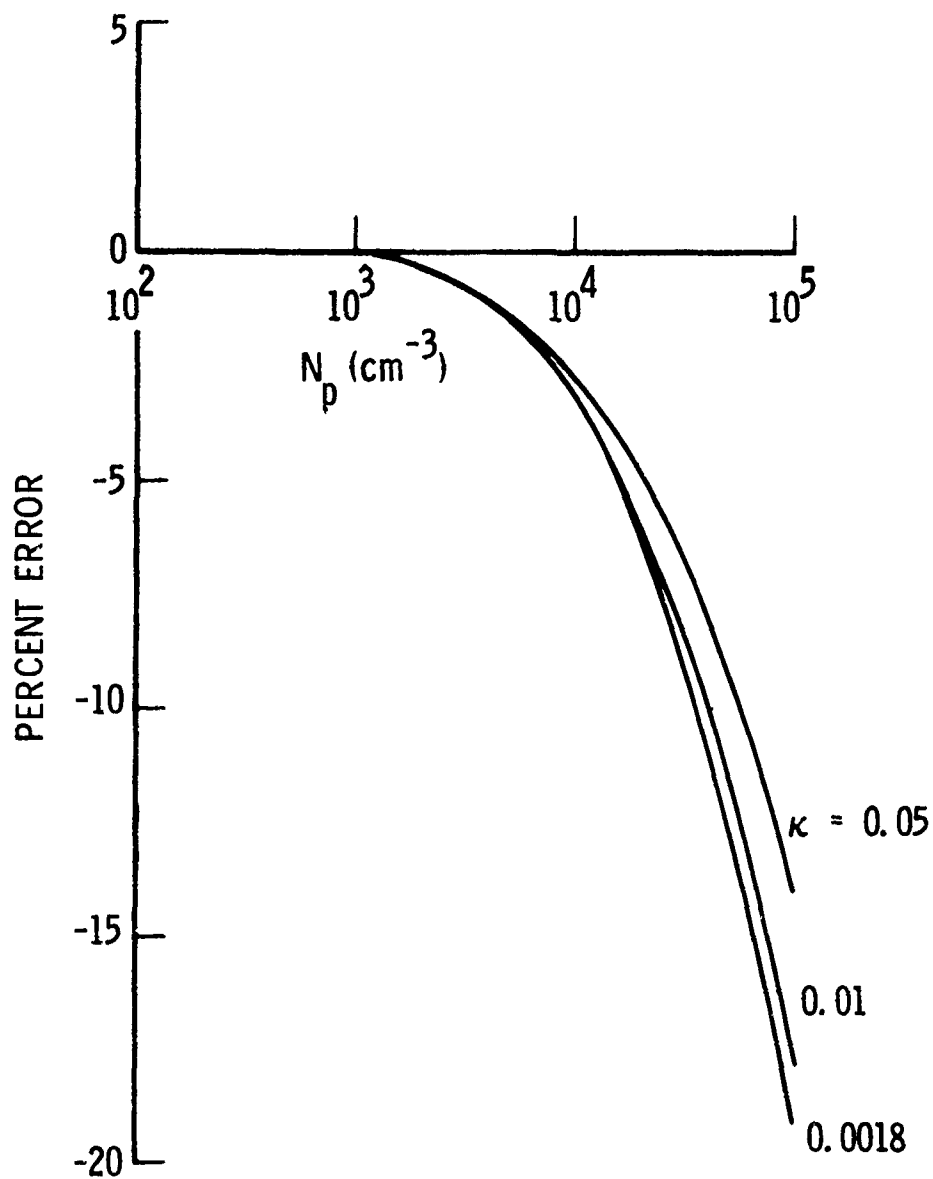


Fig. 29. Temperature Retrieval Error on the Plume Axis for the MSP Plume Model.

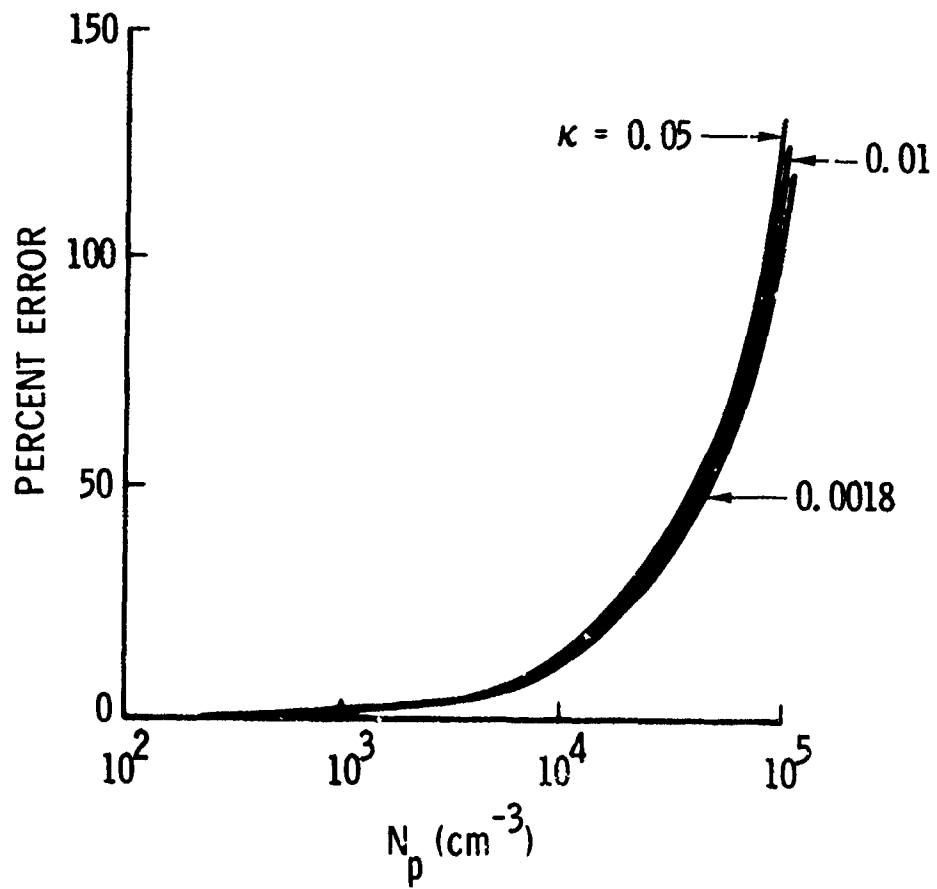


Fig. 30. Concentration Retrieval Error on the Plume Axis for the MSP Plume Model.

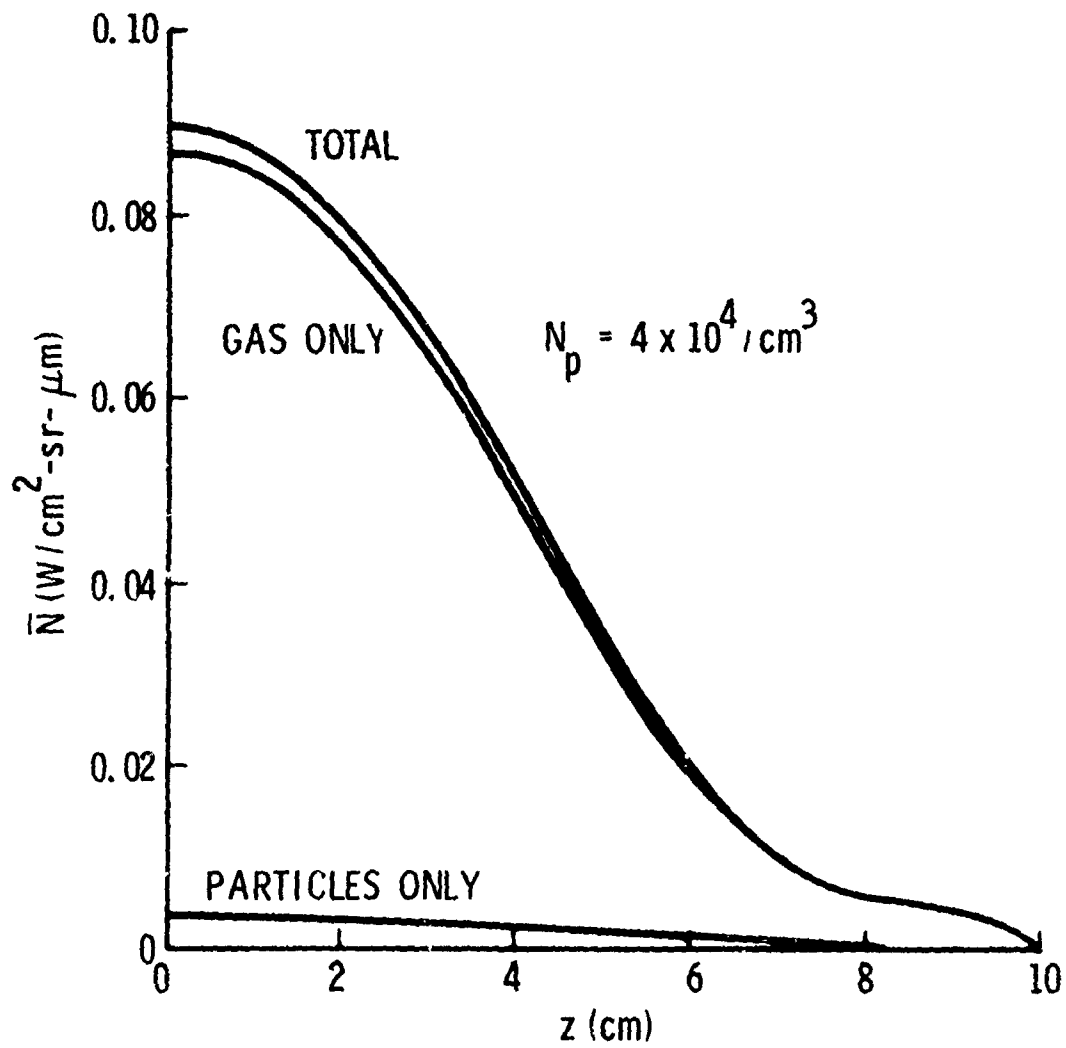


Fig. 31. Transverse Radiance Profiles for Gas and Particle Phases for the MSP Plume Model.

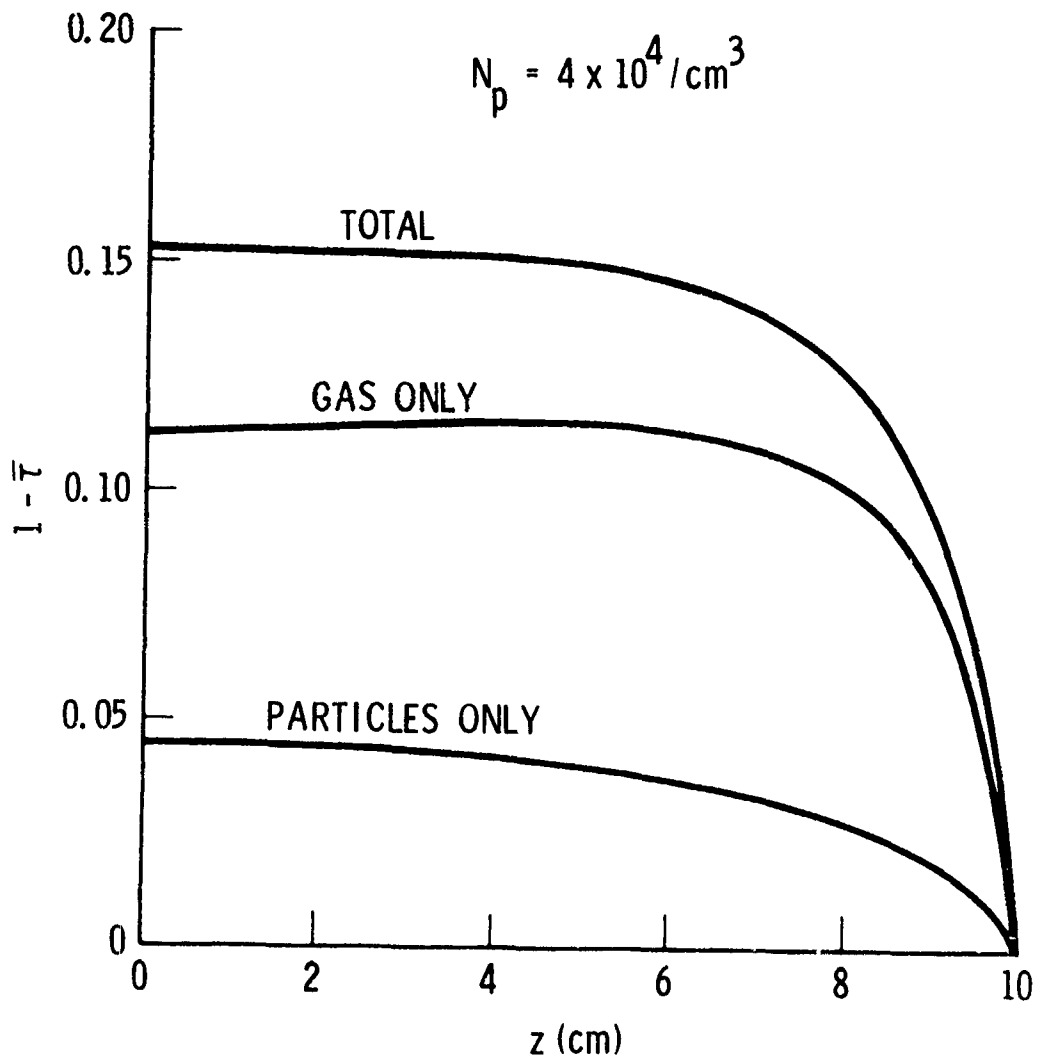


Fig. 32. Transverse Extintance Profiles for Gas and Particle Phases for the MSP Plume Model.

The errors in approximating gas-only radiance as the difference $\bar{N}_g = \bar{N} - \bar{N}_p$ are shown in Fig. 33. Figure 33a shows the errors as a function of z for the fixed particle density of $4 \times 10^4/\text{cm}^3$ while Fig. 33b shows the error at $z = 0$ for variable particle density. Since the loading level is low, the error of the approximation is not large. The error of approximating the gas-only transmittance by $\bar{\tau}_g = \bar{\tau}/\bar{\tau}_p$ is zero since this relation is exact in the single-scattering approximation.

The accuracy of retrieval using the off-band correction method is shown in Fig. 34 and Table 12. The figure shows the radial error profile for $N_p = 4 \times 10^4/\text{cm}^3$ and the table shows the centerline error as a function of particle density. For all concentrations up to $10^5/\text{cm}^3$ loading, the retrieval error of temperature and concentration was less than the convergence criteria $\Delta T = 10\text{K}$, $\Delta c = 0.001$. Much above this level, it is expected that even the off-band correction method will fail because both the gas and particle transmittances through the plume will be less than ~ 0.9 .

Particle loading levels for various retrieval and calculational conditions are given in Table 13. The conversions between the three measures of particle loading are described in the Appendix.

4.2 Advanced Liquid Propellant (ALP) (HCl/Carbon) Plume

An analysis was made of the radiation and inversion characteristics of a model two-phase plume containing gaseous HCl and carbon particles. The major gas species of the plume are HCl, HF, and N_2 of which HCl is considered as the diagnostic radiating species and the latter two as background gases. The plume composition is given in Table 14. The gas temperature profile (Fig. 35) is parabolic with values 2278 and 1500 K at the centerline and boundary, respectively. The plume radius is 7 cm. The pressure and HCl concentration profiles are flat with values $p = 1.18 \text{ atm}$ and $c = 0.117$.

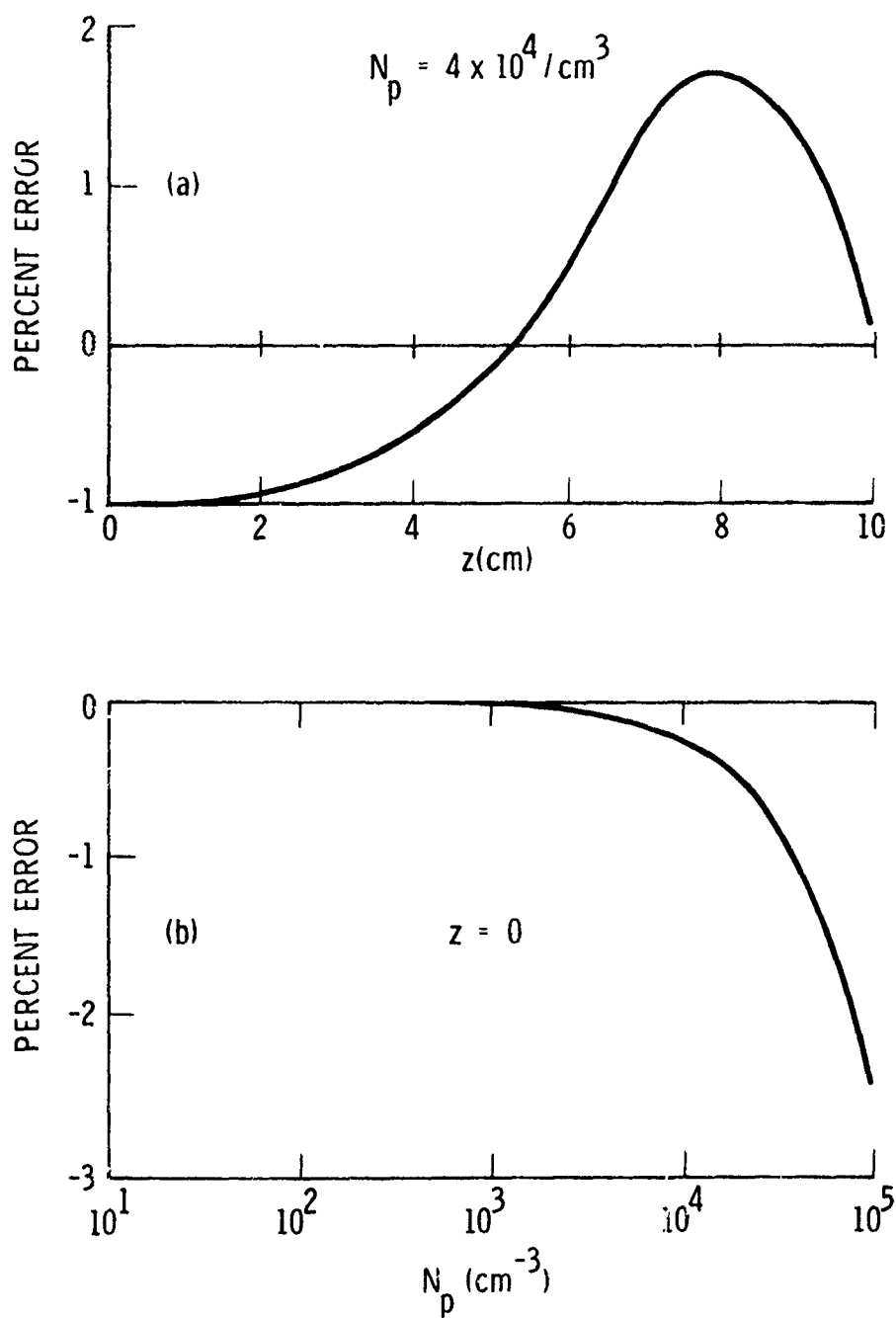


Fig. 33. Residual Errors in Radiance after First-Order, Off-Band Correction for the MSP Plume Model.
 (a) Transverse Profile Error for Fixed N_p ;
 (b) Centerline Error for Variable N_p .

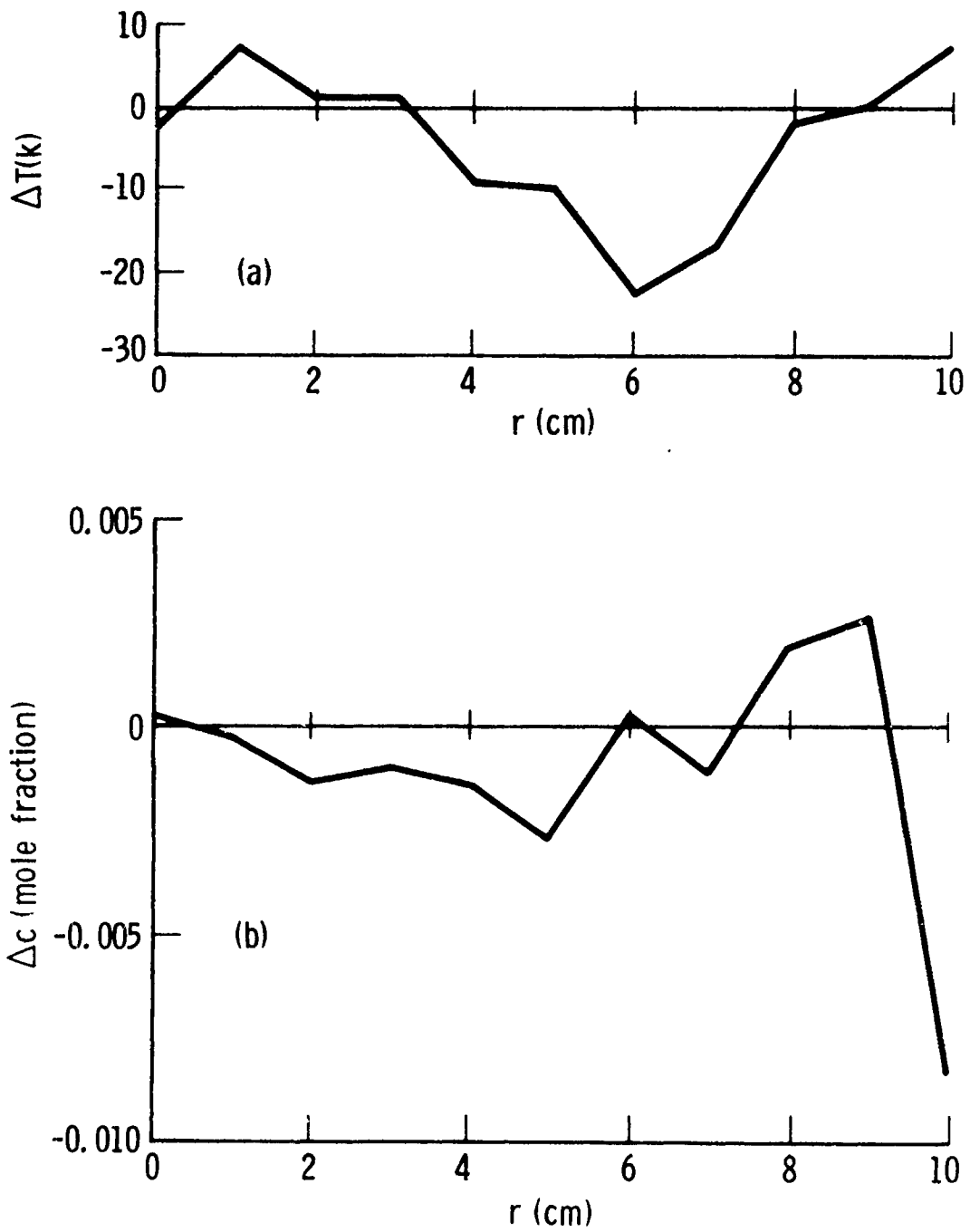


Fig. 34. Retrieval Error Profiles for the MSP Plume Model.
 (a) Temperature; (b) Gas Concentration.

Table 12. Temperature and Gas Concentration Retrieval on Plume Axis with and without First-Order, Off-Band Correction Procedure. Minimum Smoke Propellant Plume Model; $\kappa = 0.01$.

N_p (cm ⁻³)	Without Off-Band Correction			With Off-Band Correction		
	T(k)	% Error	c	T	% Error	c
0	1506	0	.1501	1506	0	.1501
100	1506		.1501	1507		.1500
400	1509		.1494	1511		.1487
1000	1503		.1516	1509		.1491
4000	1485	-1	.1562	1509		.1491
10000	1454	.3	.1663	1508		.1491
40000	1346	-10	.2202	1498		.1503
100000	1235	-18	.3354	1492		.1483

Table 13. Maximum Al_2O_3 Loading Levels for Various Retrieval and Calculation Conditions.

Condition	Loading Level		
	N_p (1/cm ³)	m_p (g/cm ³)	c_p (mole percent)
Error in c-retrieval < 10% at $r = 0$ without FO/OB*	10^4	8.5×10^{-9}	0.00074
Error in T-Retrieval < 10% at $r = 0$ without FO/OB	6×10^4	5.1×10^{-8}	0.0044
Single-scattering approximation and FO/OB valid	10^5	8.5×10^{-8}	0.0074

*FO/OB = first-order, off-band correction procedure

Table 14. Species Concentrations for Advanced Liquid Propellant Plume Model.

Species	Mole Fraction
HCl	0.117
HF	0.626
N ₂	0.149
Carbon	0.108

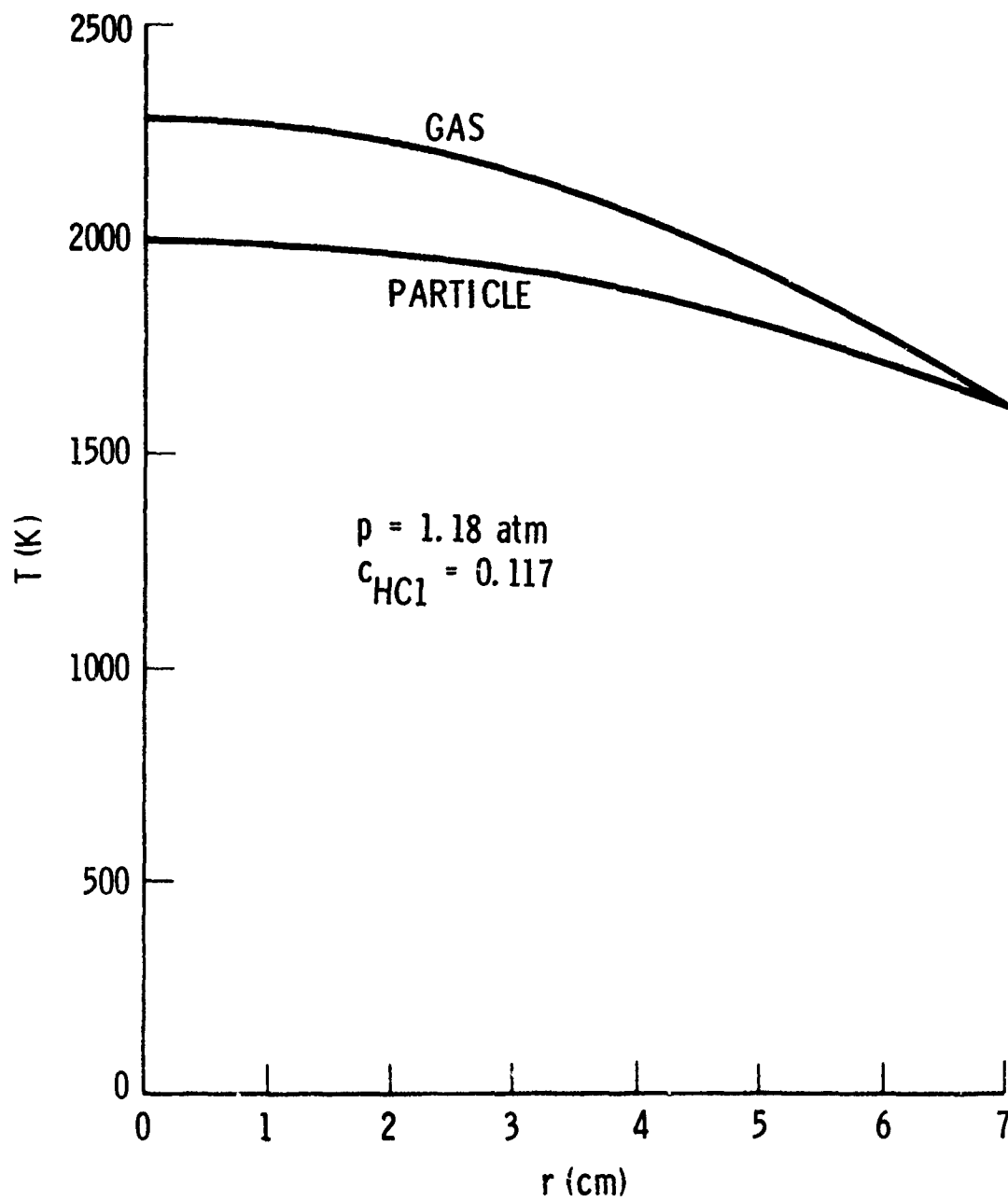


Fig. 35. Radial pTc Profiles for the ALP Plume Model.

The particle temperature profile (Fig. 35) is parabolic with values 2000 and 1600 K at the centerline and boundary, respectively. The centerline value reflects a 278 K lag in thermal equilibration between the particles and the gas. Particle concentration was assumed to be flat. The nominal concentration is $c_p = 0.108$, but this parameter was varied in the analysis.

The nozzle exit plane was modeled as a flat disc at $T = 1500$ K and $\epsilon = 0.25$. The scanning plane was placed 2.5 cm below the exit plane. Calculations were performed with the Lorentz line profile and CG approximation. The number of radial and transverse zones was seven. The $N_\theta = 11$ and $N_\phi = 16$ grid described in Section 4.1.1 was employed. Path integrations along scattering lines of sight were done with the path divided into ten equal-length segments.

The plume was assumed to be axially uniform and to extend 83 cm beyond the scanning plane. With this length, the body of the uniform plume beyond the scanning plane yields an axially directed (toward the nozzle) gas-only radiance equal to that emitted by a plume having a -8.57 K/cm linear fall-off in temperature along the axis.

The nominal mole fraction loading value of $c_p = 0.108$ converts (see Appendix) to a particle density loading of $N_p = 1.37 \times 10^8 / \text{cm}^3$. The transverse E/A profiles computed for this loading are shown in Figs. 36 and 37. The gas-only and particle-only profiles are also shown. Clearly, for this loading, the plume optical properties are particle dominated. The effects of particles are ~ 17 times those of the gas alone. The variations of the centerline ($z = 0$) radiance and extinctance with particle loading are shown in Fig. 38 and Table 15 for loading up to $4 \times 10^8 / \text{cm}^3$. Most of the effect of the particles owes to their emission and absorption, but a measurable amount is caused by scattering. This is illustrated in Figs. 39 and 40 where the radiance and extinctance are shown as computed at the nominal loading level with and without particle scattering (but with emission and absorption).

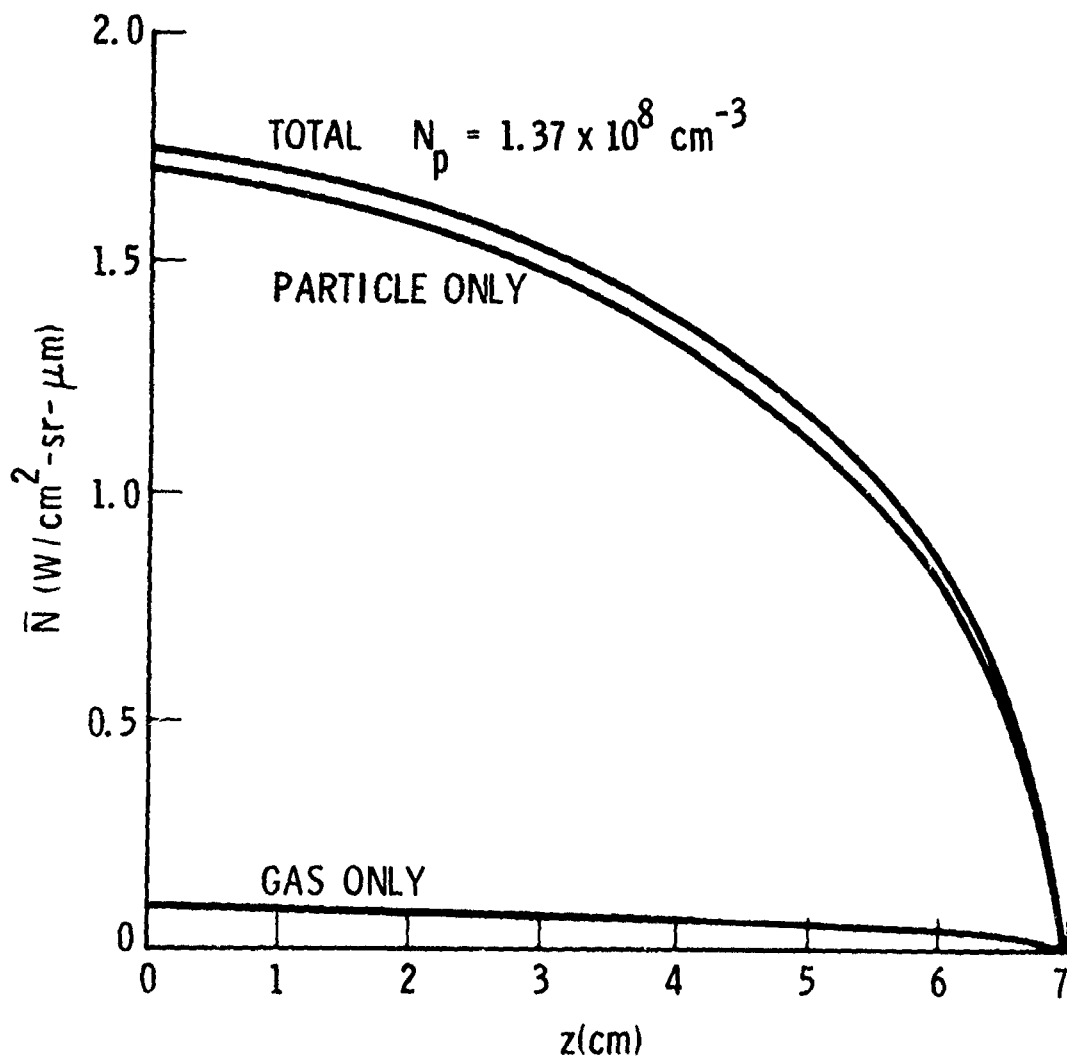


Fig. 36. Transverse Radiance Profiles for the ALP Plume Model.

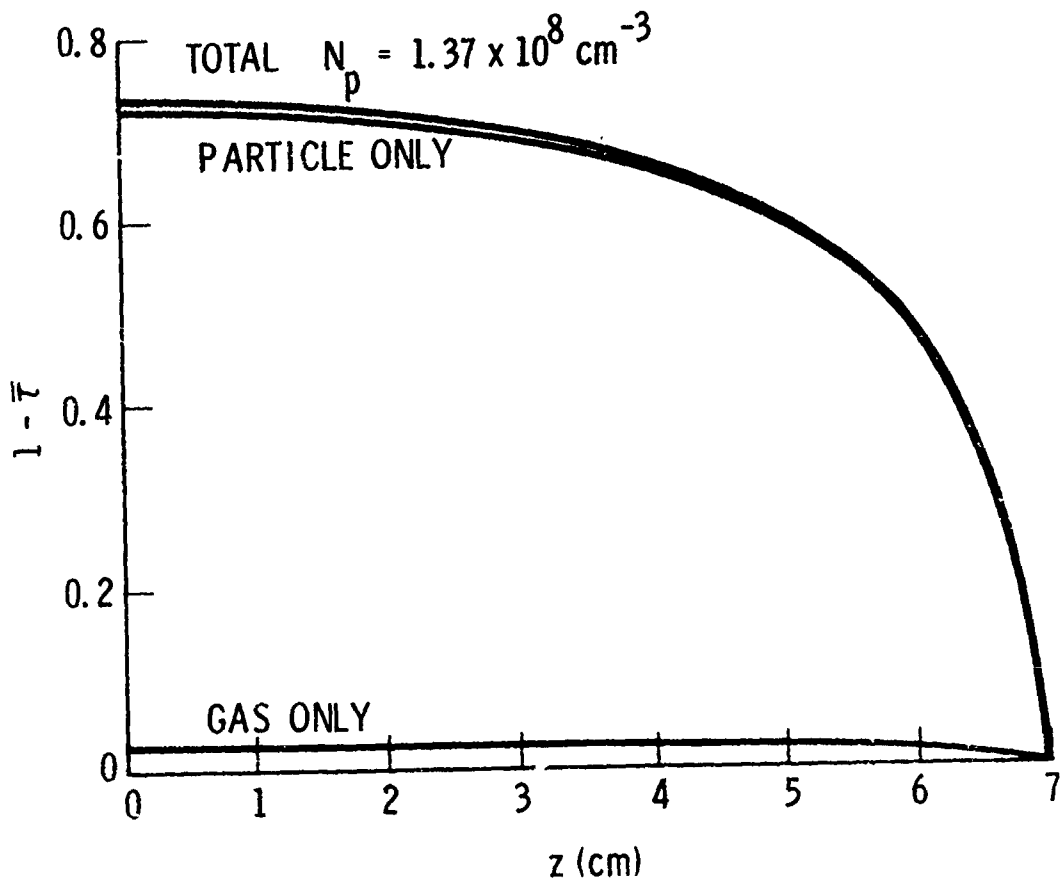


Fig. 37. Transverse Extinctance Profiles for the ALP Plume Model.

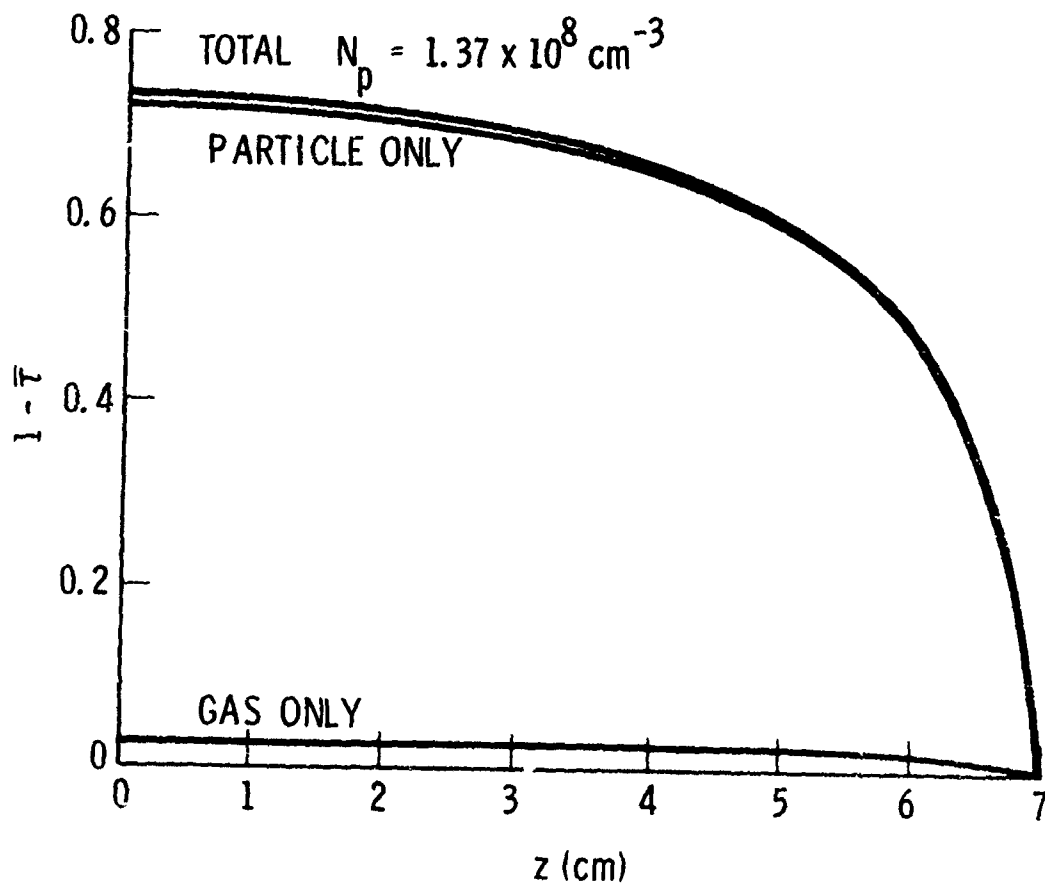


Fig. 37. Transverse Extinctance Profiles for the ALP Plume Model.

**THIS REPORT HAS BEEN DELIMITED
AND CLEARED FOR PUBLIC RELEASE
UNDER DOD DIRECTIVE 5200.20 AND
NO RESTRICTIONS ARE IMPOSED UPON
ITS USE AND DISCLOSURE.**

DISTRIBUTION STATEMENT A

**APPROVED FOR PUBLIC RELEASE,
DISTRIBUTION UNLIMITED.**

Table 15. Variation of Radiance and Extinctance at $z = 0$
with Particle Density for Advanced Liquid
Propellant Plume Model.

$N_p (\text{cm}^{-3})$	$\bar{N} (\text{W}/\text{cm}^2\text{-sr-}\mu\text{m})$	$1 - \bar{\tau}$
0	.09731	.02666
1(4)	.09750	.02674
4(4)	.09809	.02703
1(5)	.09926	.02758
4(5)	.1051	.03035
1(6)	.1168	.03587
4(6)	.1745	.06297
1(7)	.2863	.1149
4(7)	.7773	.3345
1(8)	1.463	.6238
4(8)	2.307	.9783

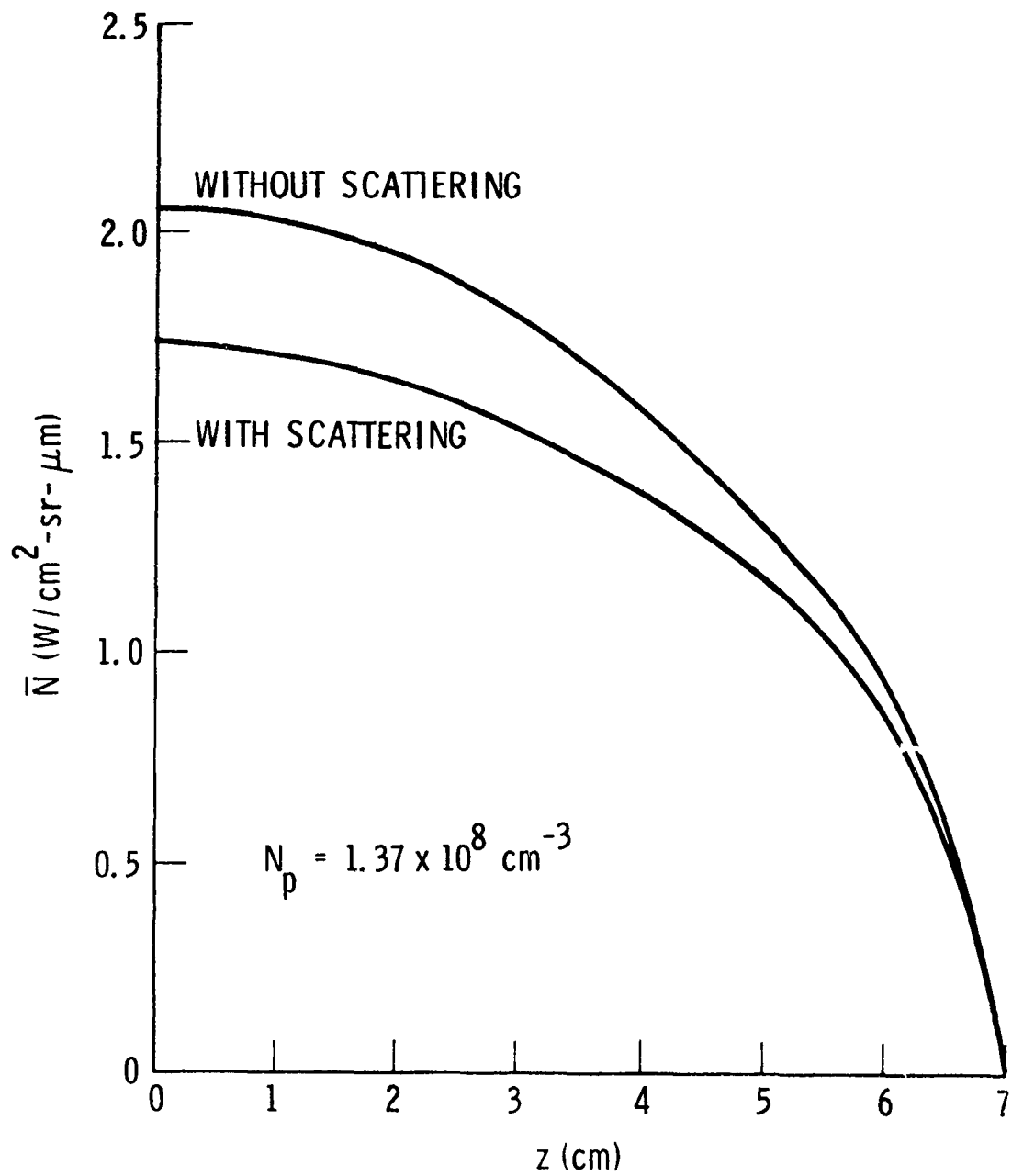


Fig. 39. Transverse Radiance Profiles for the ALP Plume Model Computed with and without Scattering.

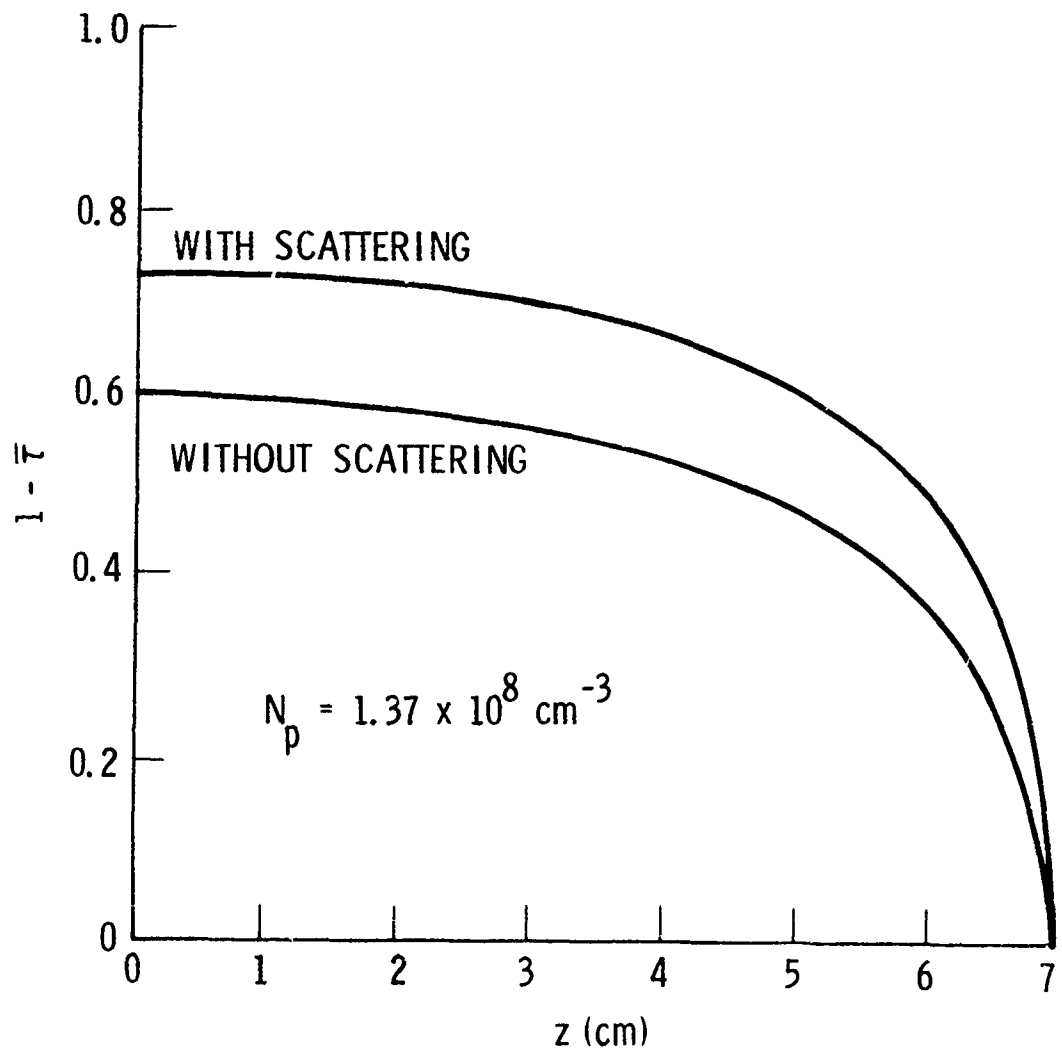


Fig. 40. Transverse Extinctance Profiles for the ALP Plume Model Computed with and without Scattering.

Inversion of the total (gas-plus) E/A profiles of Figs. 36 and 37 yields the temperature and concentration results shown in Figs. 41 and 42 (labeled Retrieved). The retrieved temperature profile is 300 to 500 K too low; the retrieved HCl concentration is two orders of magnitude too large. The variations of retrieval error at $r = 0$ for a range of loading levels are shown in Figs. 43 and 44 and Table 16.

The off-band correction procedure was applied using the particle-only profiles shown in Figs. 36 and 37. The inversion results are shown in Figs. 41 and 42. The temperature retrieval has been worsened (by up to 500 K at $r = 0$), but the concentration retrieval has been improved dramatically. This is in keeping with previous results where it has always been found that concentration retrieval error is much larger than temperature retrieval error and is the more improved with the application of the off-band procedure. However, the retrieved concentration is still a factor of two different from the true value. The conclusion is that the nominal carbon loading of

$$c_p = .108$$

$$m_p = 9.32 \times 10^{-6} \text{ g/cm}^3$$

$$N_p = 1.37 \times 10^8 / \text{cm}^3$$

is too large for application of the gas-only inversion diagnostic, even with the off-band correction procedure.

Actually, these poor results are to be expected for this case. In the first place, the nominal loading level is very much higher than the level at which the single-scattering approximation should be valid. This level is

$$c_p = .0298$$

$$m_p = 2.36 \times 10^{-6} \text{ g/cm}^3$$

$$N_p = 3.47 \times 10^7 / \text{cm}^3$$

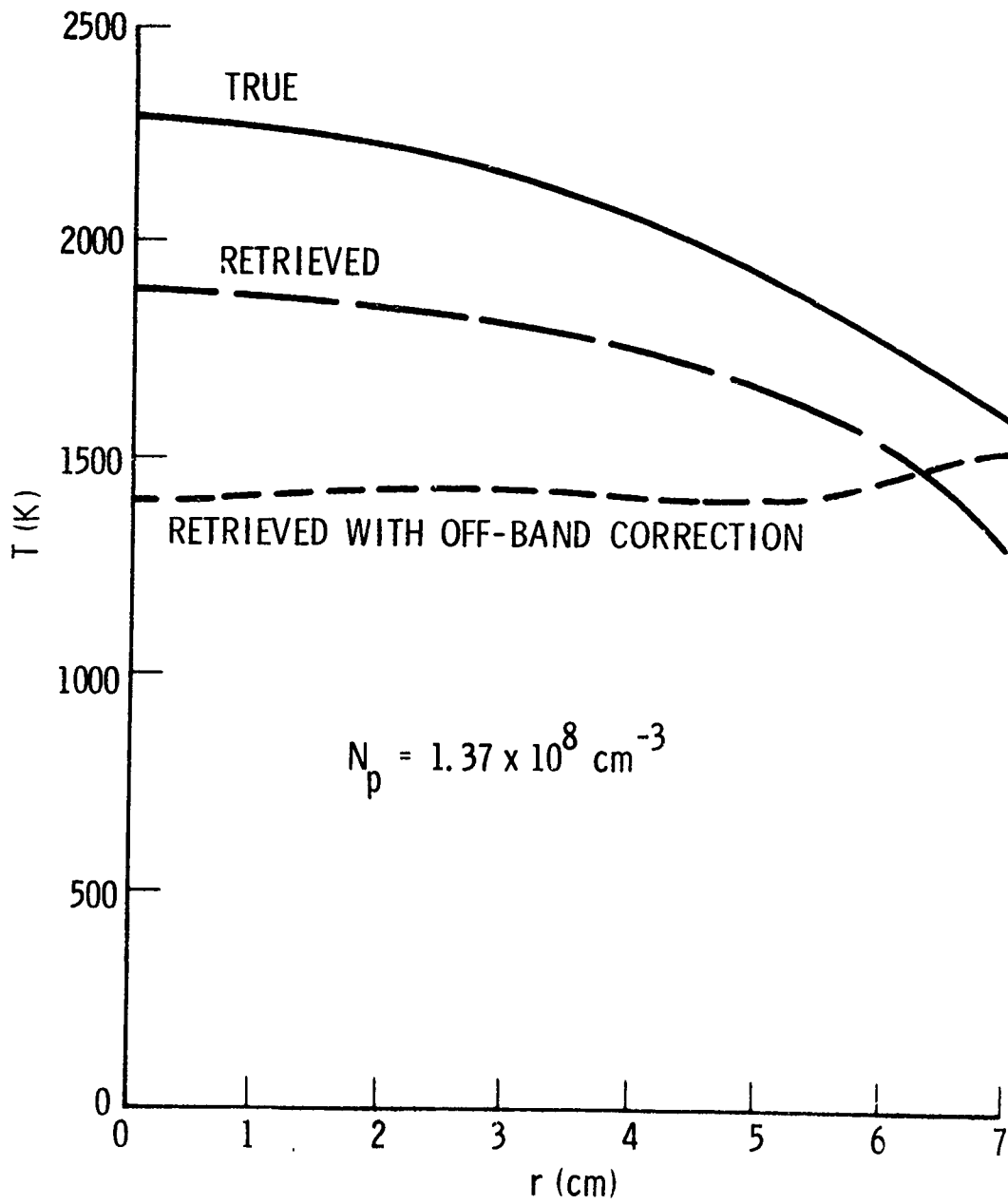


Fig. 41. Temperature Retrieval Results for the ALP Plume Model.

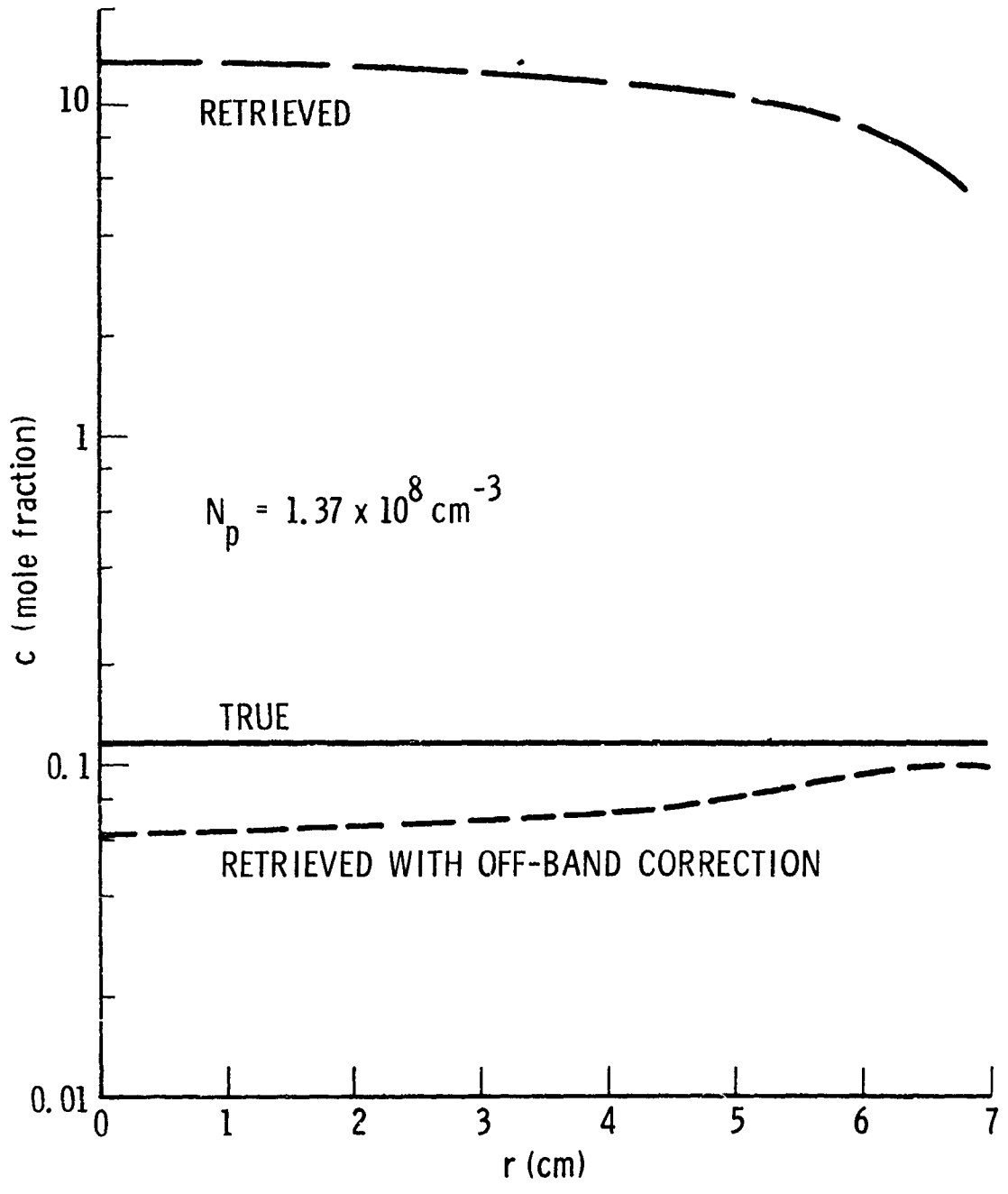


Fig. 42. Concentration Retrieval Results for the ALP Plume Model.

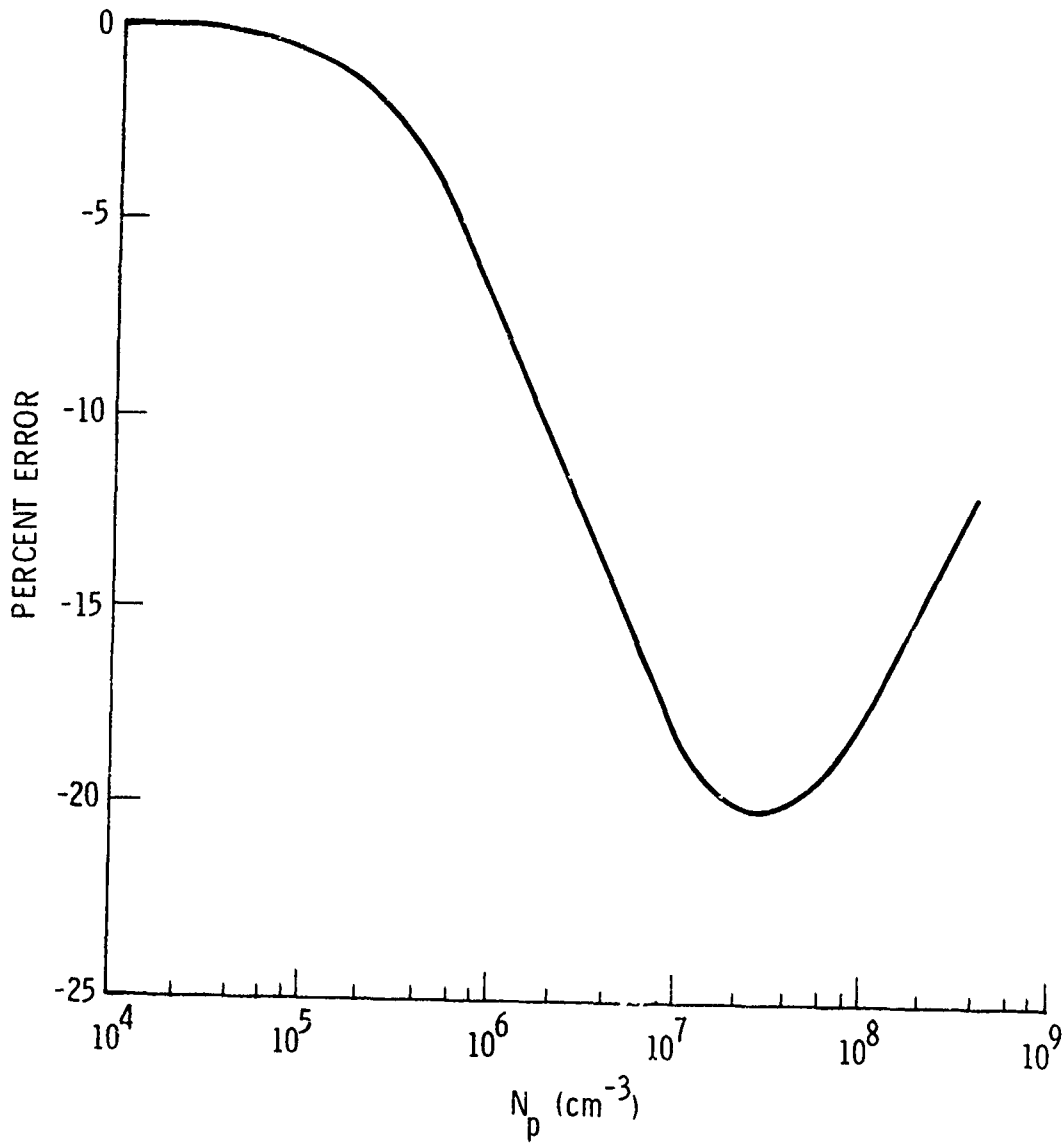


Fig. 43. Temperature Retrieval Error on the Plume Axis for the ALP Plume Model.

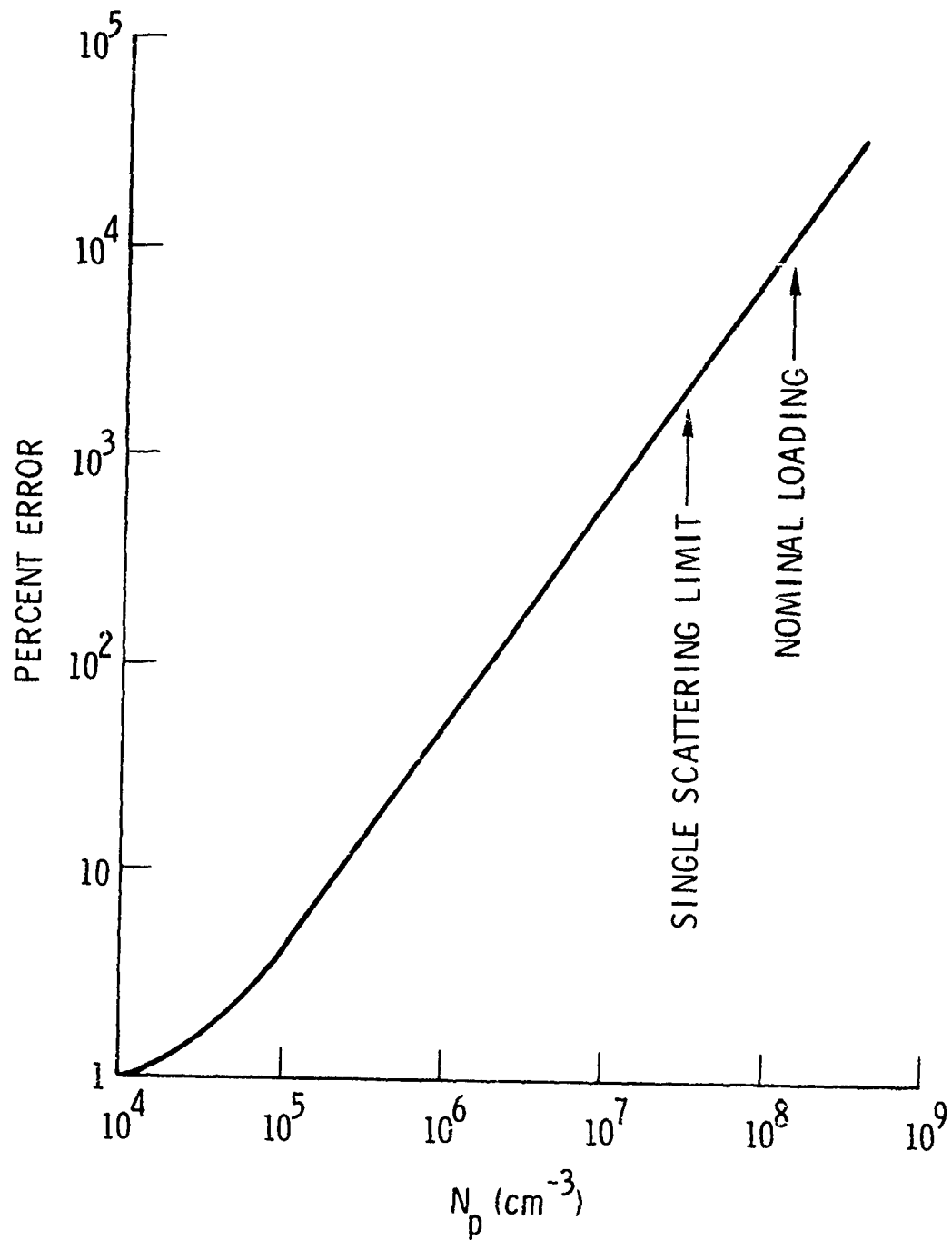


Fig. 44. Concentration Retrieval Error on the Plume Axis for the ALP Plume Model.

Table 16. Temperature and Gas Concentration Retrieval on Plume Axis for Advanced Liquid Propellant Plume Model.

N_p (cm^{-3})	c_p (%)	T(K)	% Error	c	% Error
0	0	2284	0.3	.1161	-0.8
1(4)	.0009	2288	0.4	.1150	-1.7
4(4)	.0035	2296	0.8	.1156	-1.2
1(5)	.0089	2263	-0.7	.1211	3.5
4(5)	.035	2215	-2.8	.1386	19
1(6)	.088	2120	-6.9	.1785	53
4(6)	.35	1962	-14	.4026	244
1(7)	.88	1871	-18	.9341	698
4(7)	3.4	1831	-20	3.836	3.18(3)
1(8)	8.1	1869	-18	9.952	8.41(3)
4(8)	26.1	1992	-12	42.38	3.61(4)

In the second place, the first-order off-band correction procedure should not necessarily provide much improvement (and it doesn't for temperature retrieval) because the requirement that both the gas and particle transmittances through the plume be ≥ 0.9 is violated. For the nominal loading level, the particle transmittance is ~ 0.3 (Fig. 37). The maximum loading level for which this procedure is valid is

$$c_p = .0092$$

$$m_p = 7.55 \times 10^{-7} \text{ g/cm}^3$$

$$N_p = 1.11 \times 10^7 / \text{cm}^3$$

4.3 Reduced Smoke Propellant (RSP) (H_2O , CO_2 , CO , HCl/ZrO_2) Plume

Analyses were made for two RSP plumes containing H_2O , CO_2 , CO , and HCl as the gas-phase species and ZrO_2 as the solid-phase species. The gas temperature and pressure profiles for the two cases are shown in Figs. 45 and 46. Unlike the previous plume models, temperature and pressure here increase with radial distance. The significant differences between the two cases is the lower overall temperature for the model of Fig. 45. This model will be referred to here as the "low-temperature" model. For both models, the plume radius is $R = 5.69$ cm. The gas concentration profiles were assumed to be flat, and their magnitudes are listed in Table 17. Note that the low temperature model does not include HCl as an active species.

Analyses were made only for the single loading level of $m_p = 2.28 \times 10^{-8} \text{ g/cm}^3$ for each model. Two spatial distributions were considered. The first is simply a uniform distribution (constant in r). The second is the Gaussian distribution

$$N(r) = N_0 e^{-\gamma(r/R)^2}$$

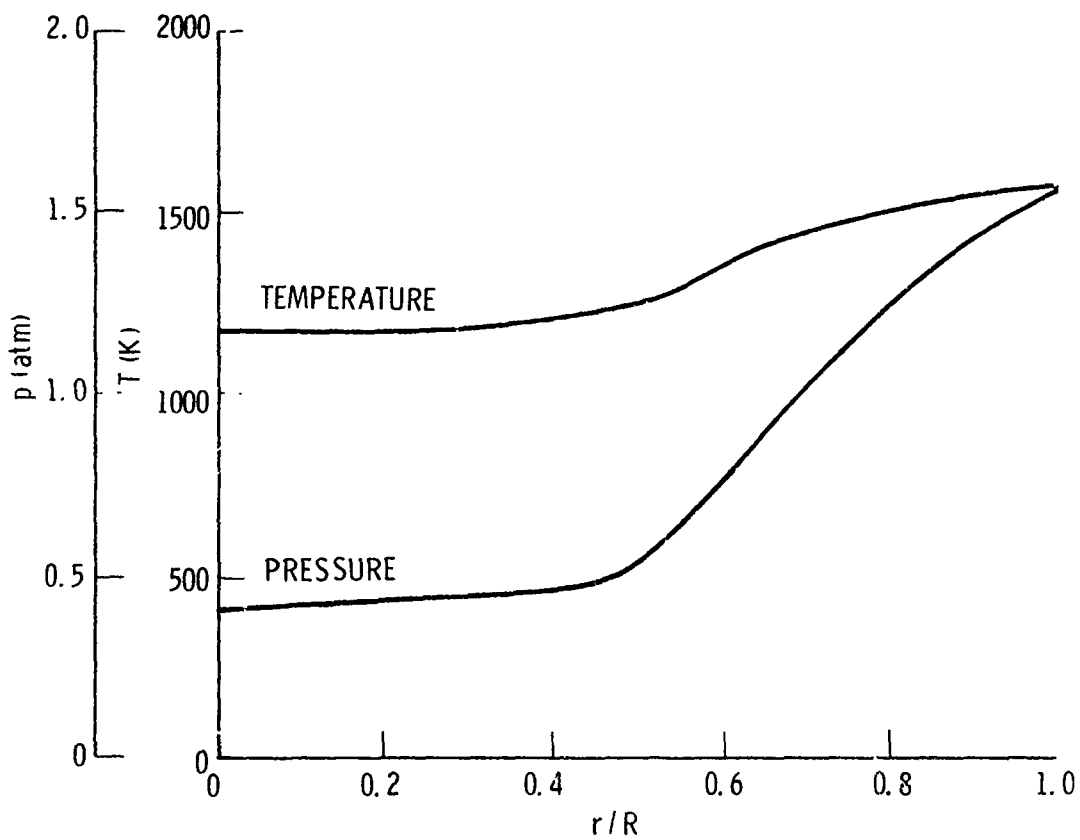


Fig. 45. Radial pTc Profiles for the Low-Temperature RSP Plume Model.

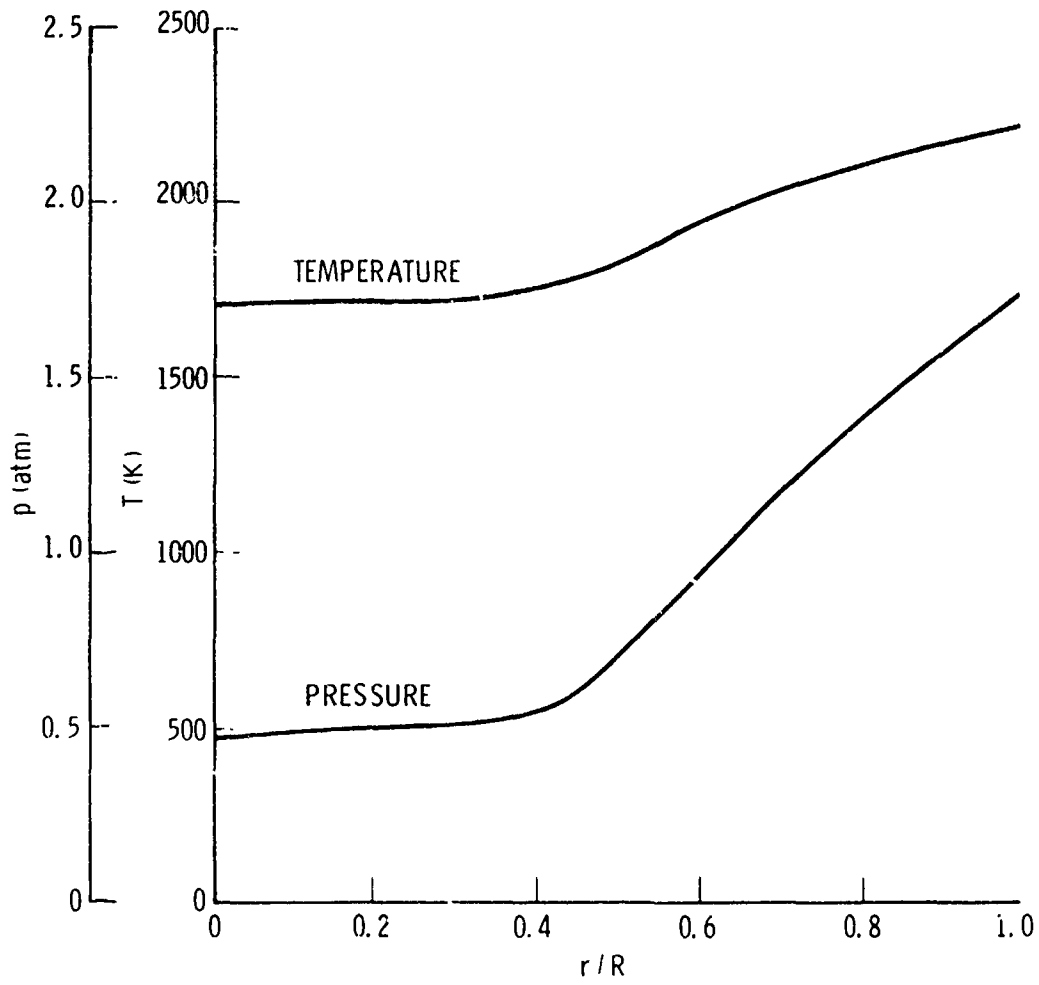


Fig. 46. Radial pTc Profiles for the High-Temperature RSP Plume Model.

Table 17. Species Concentrations for Reduced Smoke Propellant Plume Model.

Species	Low-Temperature Model	High-Temperature Model
H ₂ O	0.155	0.275
CO ₂	0.165	0.200
CO	0.370	0.140
HCl	—	0.245

This distribution is shown in Fig. 47. The value $\gamma = 9.212$ was selected to force the number density at $r = R/2$ to be one-tenth of its value at $r = 0$. The centerline value is related to the mean value over the cross section of the plume by $N_o = \gamma \bar{N} / (1 - e^{-\gamma})$.

For the uniform spatial distribution, the number densities are (see Appendix)

$$N_p = \begin{cases} 990/\text{cm}^3 & \text{(monodisperse)} \\ 18000/\text{cm}^3 & \text{(bimodal)} \end{cases}$$

for the monodisperse and bimodal size distributions (see Section 3.2.2).

For the Gaussian distribution, the centerline values are

$$N_o = \begin{cases} 9120/\text{cm}^3 & \text{(monodisperse)} \\ 1.66 \times 10^5/\text{cm}^3 & \text{(bimodal)} \end{cases}$$

The particle temperature profile was assumed to be the same as the gas temperature profile.

The nozzle exit plane was modeled as a flat disc at $T = 1460$ and 2080 K for the low- and high-temperature cases, respectively, and $e = 0.25$ for both cases. These temperature values are the gas temperatures at $r/R = 0.75$. The scanning plane was placed 3 cm below the nozzle exit plane. Calculations were performed for the Lorentz line profile and CG approximation. The number of radial and transverse grids was 10. The $N_\theta = 11$, $N_\phi = 16$ grid described in Section 4.1.1 was used. Path integrations along scattering lines of sight were done with the path divided into ten equal length segments.

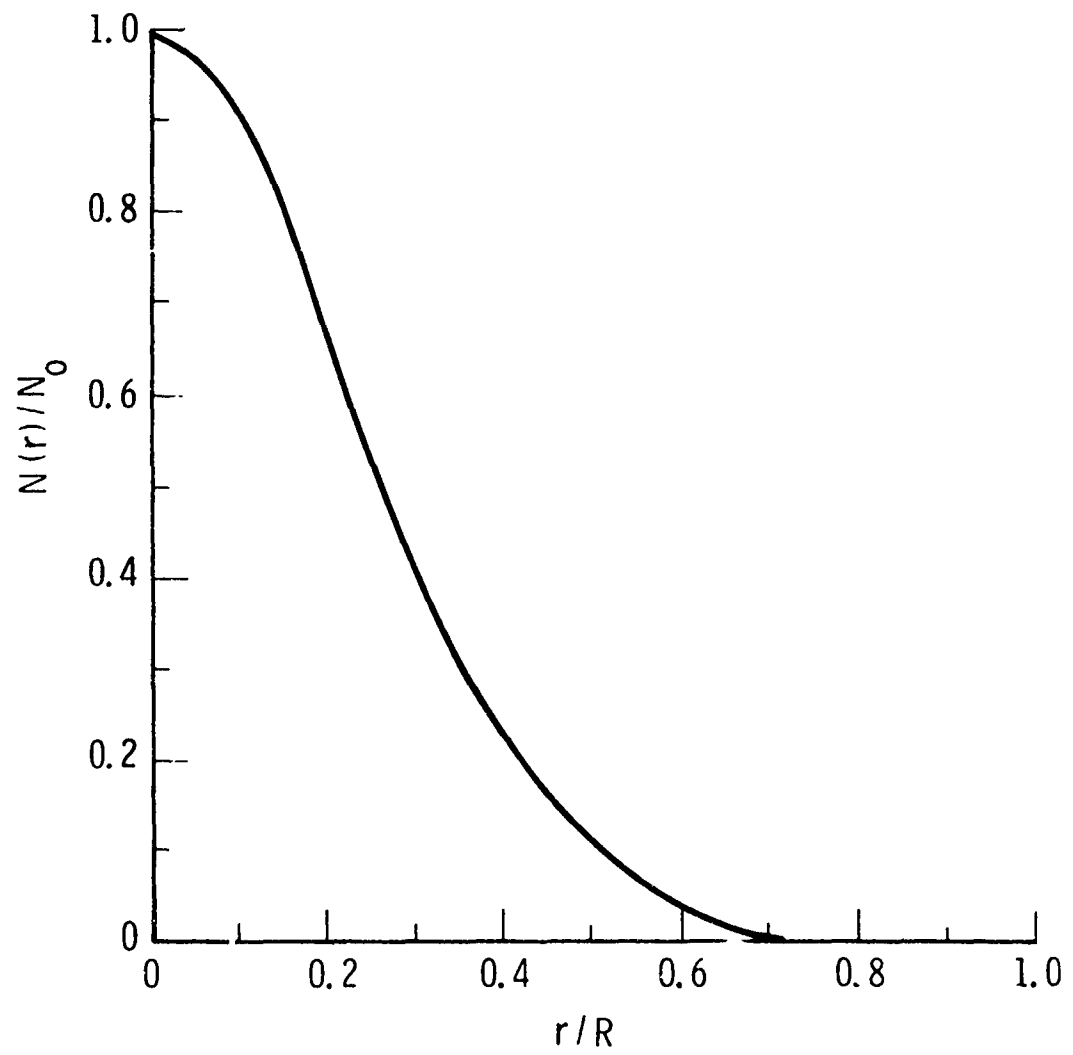


Fig. 47. Gaussian Spatial Distribution of Particle Concentration.

The plume was assumed to be axially uniform and to extend a distance L_2 beyond the scanning plane. The values employed are listed in Table 18. With these lengths, the body of the uniform plane beyond the scanning plane yields an axially directed gas-only radiance equal to that emitted by a realistic plume having a -5 K/cm linear fall-off along the axis and a linear pressure increase that restores the plume pressure to 1 atm at the point the temperature reaches 300 K.

The gas-only E/A profiles are shown in Figs. 48-51. The particle loading is so small that essentially these same profiles (with one exception) result for all combinations of spatial and size distributions. The centerline ($z = 0$) results for all conditions are given in Table 19. The one exception occurs for the bimodal size distribution and Gaussian spatial distribution for the H_2O bandpass in the low-temperature model. The gas-only, particle-only and total radiance/extinctance profiles for this case are shown in Figs. 52 and 53. The particle density and mole percent loading for this case are $N_p = 1.8 \times 10^4 / \text{cm}^3$ and $c_p = .0022\%$. These are mean values over the plume. The results of Fig. 52 and 53 demonstrate that this particle loading influences the gas-only E/A profiles only slightly and only near $z = 0$.

Retrieval analysis was made only for this one case. Inversion was performed on both the total radiance/extinctance profiles of Figs. 52 and 53 as well as the profiles resulting from the first-order, off-band correction procedure. The results are presented in Tables 20 and 21 and Fig. 54. The maximum temperature retrieval error is only $\sim 7\%$ even without the correction procedure. With correction, the maximum error is reduced to $\sim 3\%$. Without correction, the maximum H_2O concentration retrieval error is $\sim 60\%$. With correction, the error is reduced to $\sim 8\%$.

Since this retrieval case represents the worst case, the gas-only inversion diagnostic (with first-order, off-band correction) is applicable to all cases.

Table 18. Effective Plume Lengths for Reduced
Smoke Propellant Plume Models.

Case	Species	L(cm)
Low-Temperature Model	CO	57
	CO ₂	74
	H ₂ O	44
High-Temperature Model	CO	103
	CO ₂	161
	HCl	132
	H ₂ O	80

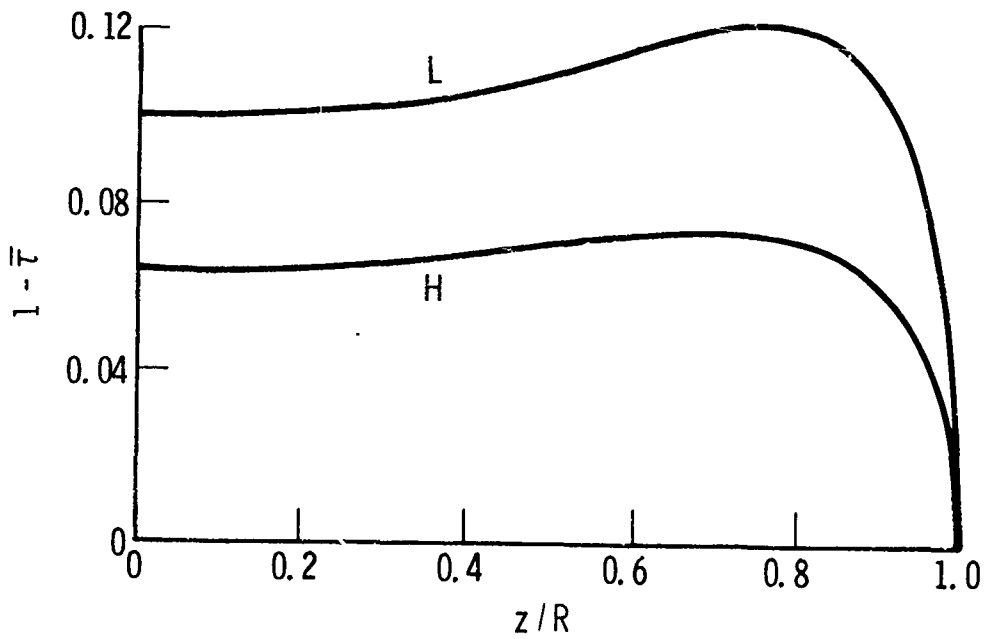
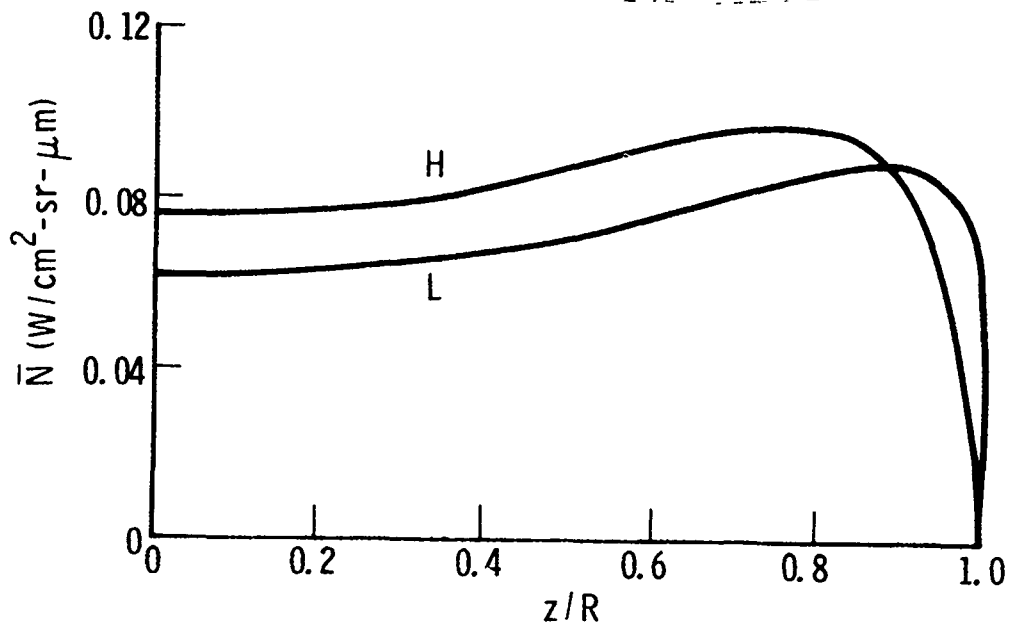


Fig. 48. Transverse E/A Profiles for CO. L = Low-Temperature Case, H = High-Temperature Case.

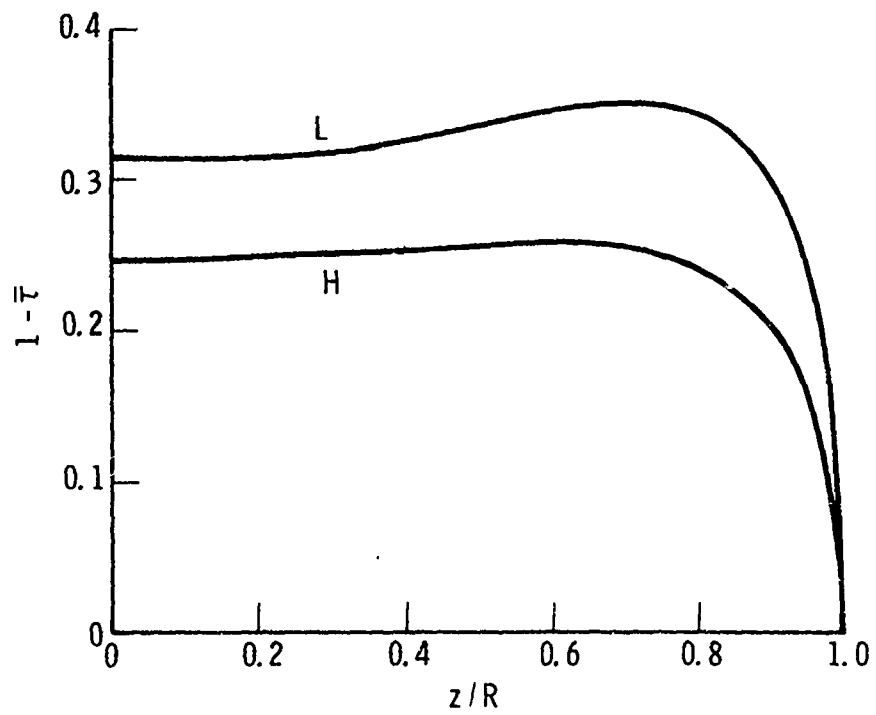
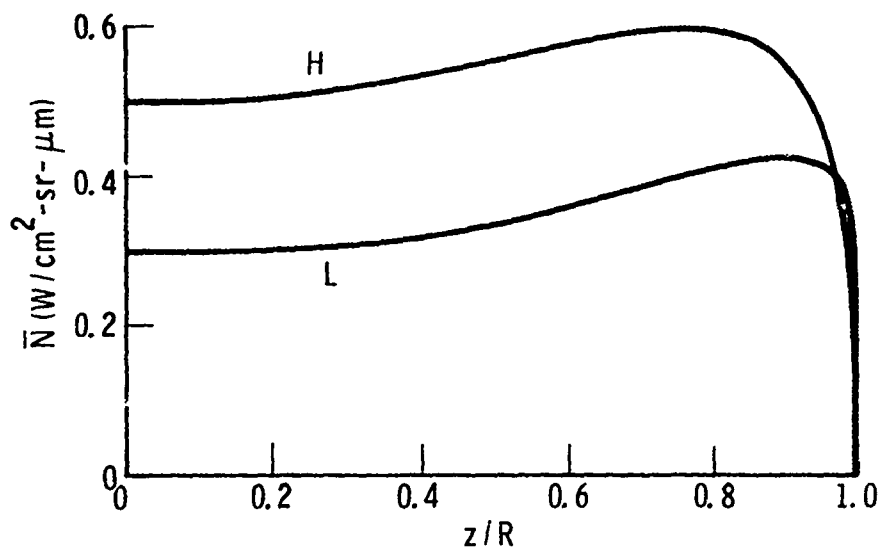


Fig. 49. Transverse E/A Profiles for CO_2 . L = Low-Temperature Case, H = High-Temperature Case.

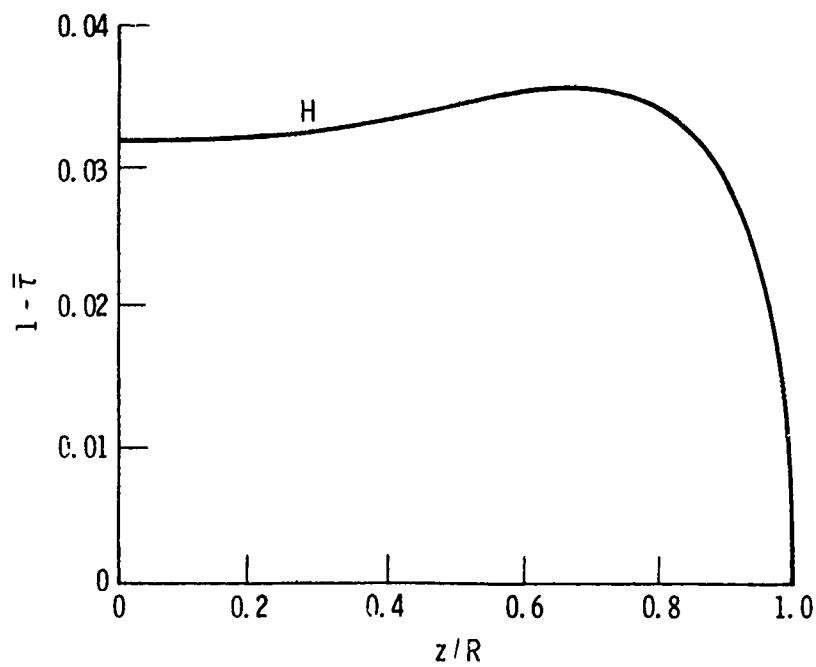
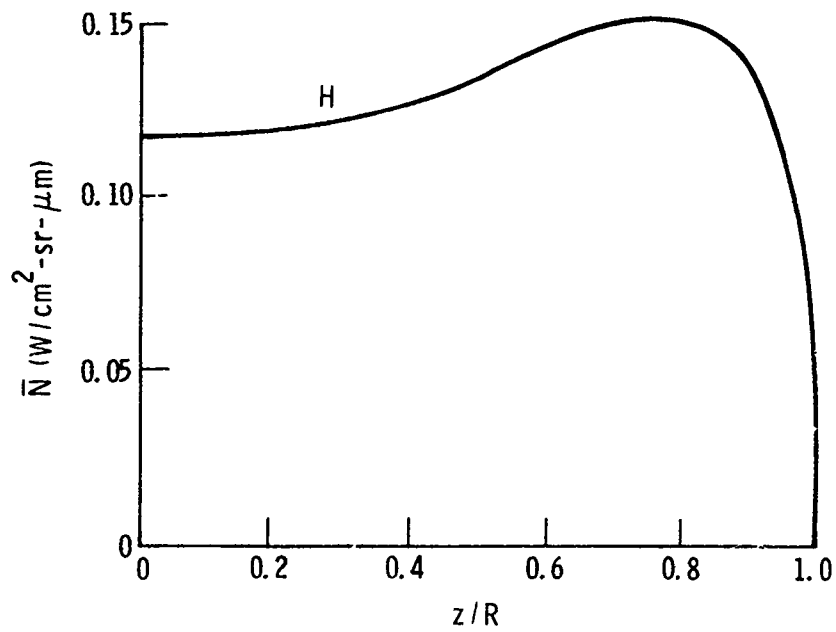


Fig. 50. Transverse E/A Profiles for HCl. L = Low-Temperature Case, H = High-Temperature Case.

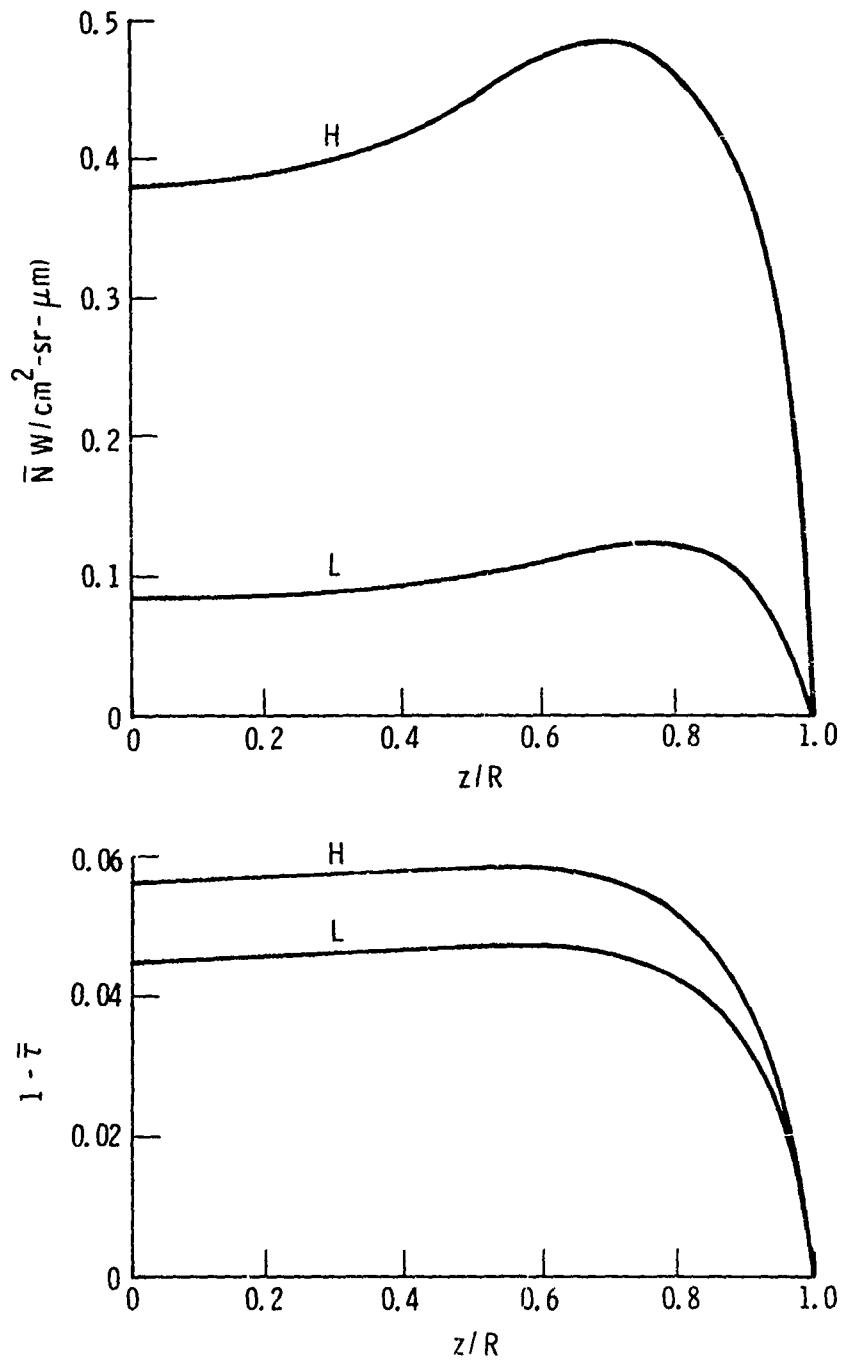


Fig. 51. Transverse E/A Profiles for H_2O . L = Low-Temperature Case, H = High-Temperature Case.

Table 19. E/A Results at $z = 0$ for Reduced Smoke Propellant Plume Models.

Case ⁽¹⁾	Particle Distribution		CO		CO ₂		HCl		H ₂ O	
	Spatial	Size ⁽²⁾	$\bar{N}^{(3)}$	$1-\bar{\tau}$	\bar{N}	$1-\bar{\tau}$	\bar{N}	$1-\bar{\tau}$	\bar{N}	$1-\bar{\tau}$
LO	(Gas only)		.06081	.1001	.2983	.3185	-	-	.08631	.04503
	Uniform	M	.06081	.1001	.2983	.3185	-	-	.08636	.04520
		B	.06087	.1005	.2984	.3189	-	-	.08687	.04695
	Gaussian	M	.06082	.1002	.2983	.3186	-	-	.08642	.04549
		B	.06095	.1012	.2984	.3197	-	-	.98734	.05019
HI	(Gas only)		.07679	.06416	.4977	.2456	.1170	.03198	.3842	.05648
	Uniform	M	.07679	.06416	.4977	.2456	.1170	.03199	.3842	.05649
		B	.07682	.06419	.4977	.2456	.1171	.03202	.3845	.05654
	Gaussian	M	.07680	.06417	.4977	.2456	.1170	.03199	.3842	.05650
		B	.07685	.06423	.4978	.2456	.1173	.03210	.3848	.05663

(1) LO = Low-Temperature model; HI = High-Temperature model

(2) M = Monodisperse size distribution; B = Bimodal size distribution

(3) Unit of \bar{N} is $W/cm^2-sr-\mu m$

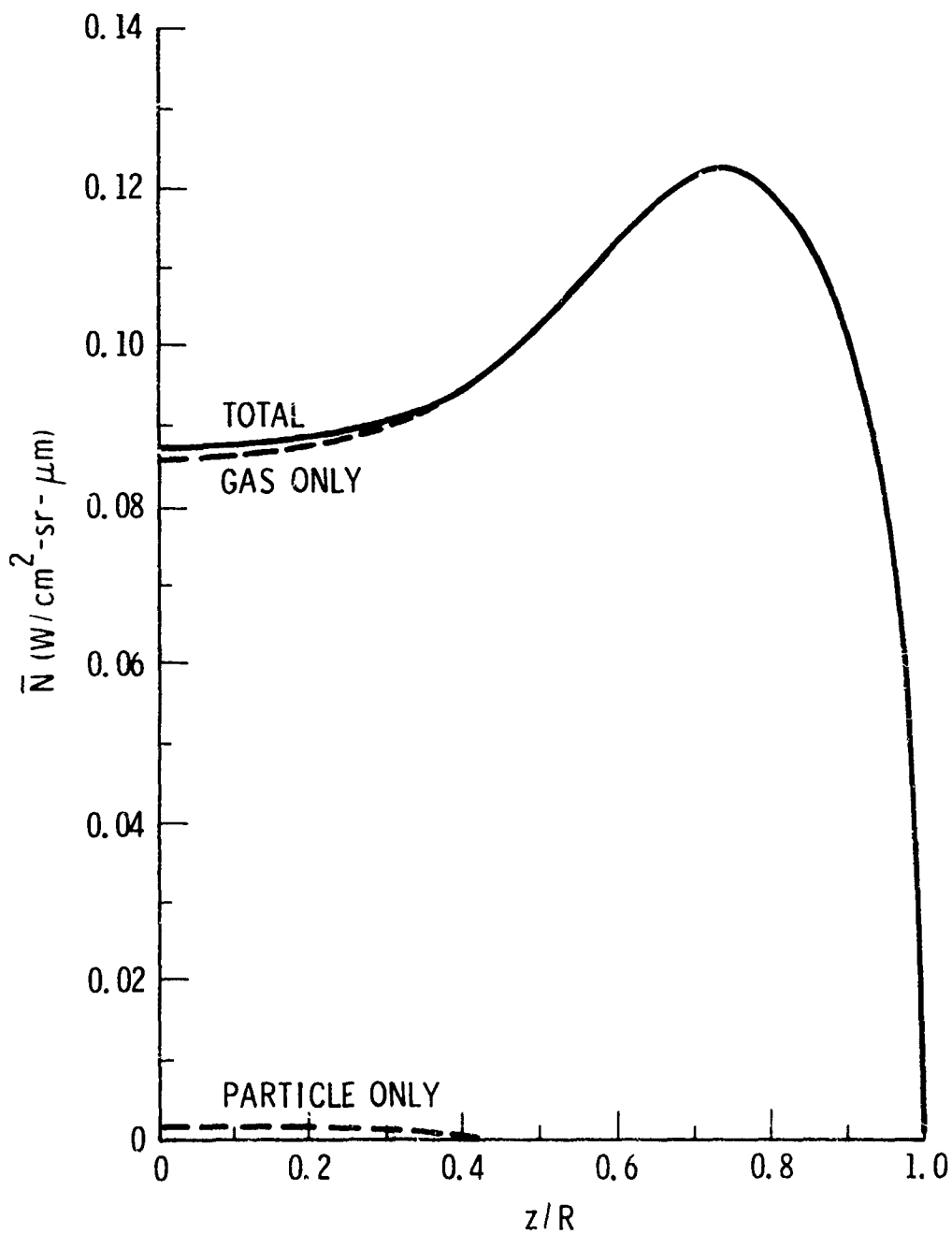


Fig. 52. Transverse Radiance Profiles for H_2O/ZrO_2 in the Low-Temperature RSP Plume Model with Bimodal Size and Gaussian Spatial Distributions.

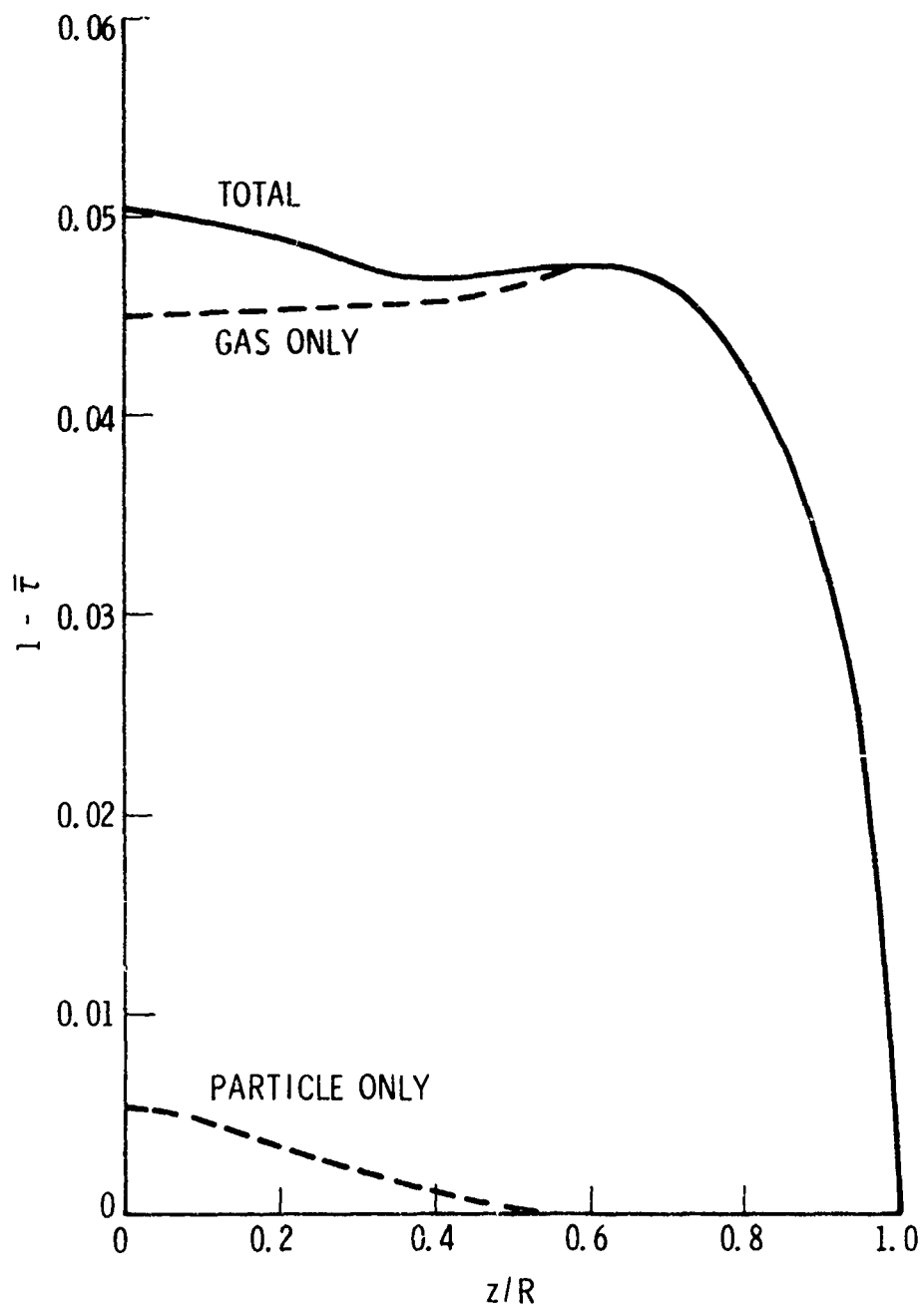


Fig. 53. Transverse Extinctance Profiles for H_2O/ZrO_2 in the Low-Temperature RSP Plume Model with Bimodal Size and Gaussian Spatial Distributions.

Table 20. Temperature Retrieval Results for Reduced Smoke Propellant Plume Model.

r/R	True *	Total Profiles			Off-band Correction		
		Retrieved *	Error *	% Error	Retrieved *	Error *	% Error
0	1183	1104	-79	-6.7	1172	-11	-.9
.1	1184	1109	-75	-6.3	1171	-13	-1.1
.2	1187	1124	-62	-5.2	1166	-21	-1.8
.3	1190	1138	-51	-4.3	1168	-22	-1.9
.4	1202	1154	-48	-4.0	1170	-32	-2.7
.5	1235	1213	-22	-1.8	1219	-16	-1.3
.6	1328	1334	-6	-.5	1337	9	.7
.7	1422	1426	4	.3	1428	6	.4
.8	1482	1484	2	.1	1484	2	.1
.9	1528	1540	12	.8	1539	11	.7
1.0	1567	1567	0	0	1568	1	.1

*Unit = K

Table 21. H₂O Concentration Retrieval for Reduced Smoke Propellant Plume Model.

r/R	True*	Total Profiles			Off-band Correction		
		Retrieved*	Error*	%Error	Retrieved*	Error*	% Error
0	1.55	.2465	.0915	59	.1451	-.0099	-6.4
.1		.2335	.0785	51	.1447	-.0103	-6.6
.2		.2092	.0542	35	.1514	-.0036	-2.3
.3		.1842	.0292	19	.1468	-.0062	-4.0
.4		.1603	.0053	3.4	.1430	-.0120	-7.7
.5		.1597	.0047	3.0	.1539	-.0011	-.7
.6		.1625	.0075	4.8	.1607	.0057	3.7
.7		.1571	.0021	1.4	.1566	.0016	1.0
.8		.1569	.0019	1.2	.1568	.0018	.2
.9		.1632	.0082	5.3	.1633	.0083	5.4
1.0		.1483	-.0067	-4.3	.1482	-.0068	-4.4

*Unit = mole fraction

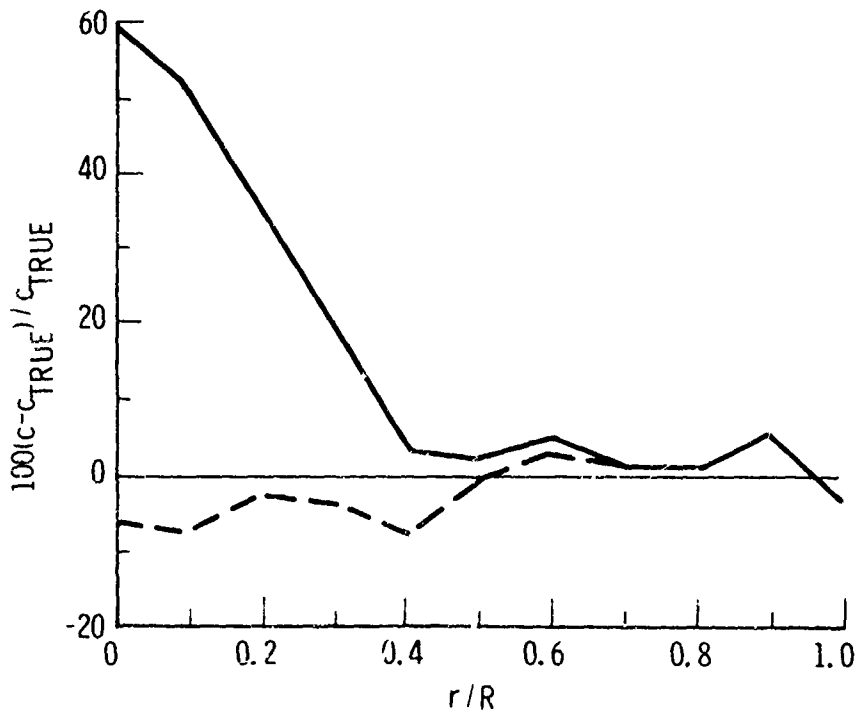
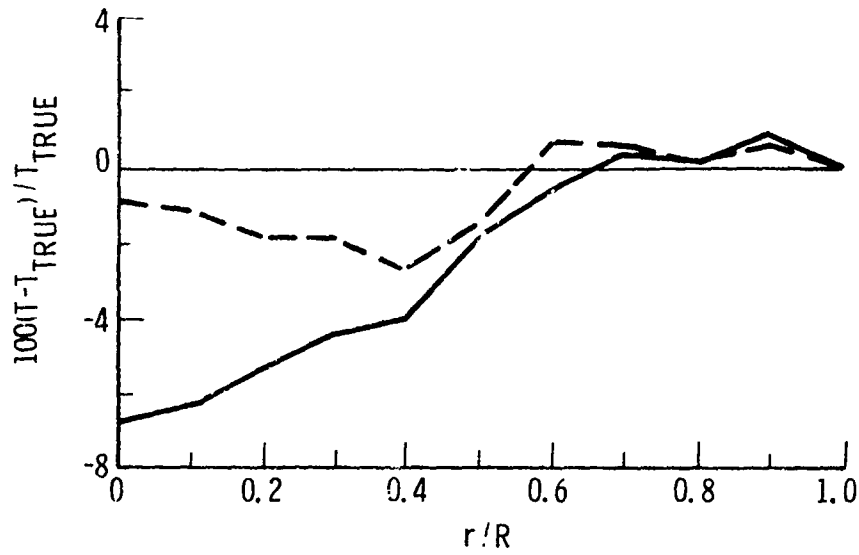


Fig. 54. Temperature and Concentration Retrieval Results for the Low-Temperature H_2O/ZrO_2 RSP Plume Model with Bimodal Size and Gaussian Spatial Distributions.

5. SUMMARY AND CONCLUSIONS

The primary goal of this work was to determine quantitative limits of particle loading in realistic tactical rocket motor plumes for which the gas properties of the plume could be retrieved with standard E/A inversion diagnostics without having to account for the radiation and absorption effects of the particles. The procedure was to assume flow-field properties for two-phase plumes of interest, generate E/A profiles with account of particles using a single-scattering plume radiation model, retrieve the gas properties from the E/A profiles with the gas-only inversion code EMABIC under the assumption that the profiles were caused by gas alone, and compare the retrieved gas properties with the assumed properties. Generally, the degree of particle loading was treated as a parameter.

Two important results were obtained. The first is that the limit of particle loading at which reasonable ($\leq 10\%$ error) retrieval results can be obtained is generally smaller than the nominal loading level for the plume. The important implication of this result is that, to the extent that the systems studied here are typical, E/A diagnostics on plumes generated by even low- and reduced-smoke type propellants requires some account of particle effects. The second result is that the maximum loading level for acceptable gas temperature retrieval is much higher (about an order of magnitude) than that for gas concentration retrieval. Consequently, in applications where temperature retrieval is of primary concern, the use of gas-only E/A diagnostics may be justified even though the total retrieval results may be substantially in error. These loading level results are summarized in Table 22 for the three systems studied here.

Analysis was also made of a correction procedure in which first-order corrections were made to the total gas/particle E/A profiles by using particle-only E/A profiles obtained outside the gas absorption band. The corrected profiles provide better estimates to the gas-only profiles needed

in the gas-only inversion. The particle loading limit for valid use of this procedure is the value for which the total extinction of radiation by particles over a full diameter of the plume is ~ 10 percent. (Note that if this condition is met, then the condition is also met that the attenuation by scattering alone over this path is less than ~ 10 percent. The latter condition is required by the single-scattering assumption used in this work.) For the two cases (MSP and RSP) where the nominal loading limit roughly satisfies this condition (see Table 22), the use of the procedure gave retrieved gas properties that were accurate to within the convergence criteria set on the inversion. For the ALP model, the nominal loading level was well above this limit, and the retrieval results were poor.

Table 22. Summary of Critical Loading Levels.

Model	Species	Loading Levels (cm^{-3})			
		$\tau_e > 0.9$	$\epsilon_c < 10\%$	$\epsilon_T < 10\%$	Nominal
MSP	$\text{Al}_2\text{O}_3/\text{H}_2\text{O}$ ⁽¹⁾	8.9 (4)	1.0 (4)	6.0 (4)	1.0 (5)
ALP	Carbon/HCl	1.1 (7)	1.0 (5)	1.0 (6)	1.4 (8)
RSP	$\text{ZrO}_2/\text{H}_2\text{O}$ ⁽²⁾	9.4 (5)	3.0 (3) ⁽³⁾	2.0 (4)	1.8 (4) ⁽⁴⁾

(1) $\kappa = 0.01$

(2) Bimodal size distribution, Gaussian spatial distribution, low-temperature model.

(3) Linear extrapolation from 60% error at $N_p = 1.8 \times 10^4 / \text{cm}^3$.

(4) Average over observation plane.

REFERENCES

1. S. J. Young, Inversion of Plume Radiance and Absorption Data for Temperature and Concentration, AFRPL-TR-78-60, U.S. Air Force Rocket Propulsion Laboratory, Edwards Air Force Base, Calif., 29 September 1978.
2. C. C. Limbaugh, W. T. Bertrand, E. L. Kiech and T. G. McRae, Nozzle Exit Plane Radiation Diagnostics Measurements of the Improved Transtage Liquid Rocket Injector Program, AEDC-TR-79-29, ARO Inc., Arnold Engineering Development Center, Arnold Air Force Station, Tenn., March 1980.
3. S. J. Young, Random Error Propagation Analysis in the Plume Diagnostic Code EMABIC, AFRPL Technical Report, to be published.
4. S. J. Young, Multicolor Inversion Diagnostic for Tactical Motor Plumes, AFRPL-TR-80-30, U.S. Air Force Rocket Propulsion Laboratory, Edwards Air Force Base, Calif., May 1980.
5. S. J. Young, User's Manual for the Plume Signature Code EAPROF, AFRPL-TR-81-08, U.S. Air Force Rocket Propulsion Laboratory, Edwards Air Force Base, Calif., January 1981.
6. C. B. Ludwig, W. Malkmus, J. E. Reardon, and J. A. L. Thompson, Handbook of Infrared Radiation from Combustion Gases, eds. R. Goulard and J. A. L. Thompson, NASA SP-3080, Marshall Space Flight Center, Huntsville, Ala., 1973.
7. S. J. Young, Band Model Parameters for the 2.7- μm Bands of H_2O and CO_2 in the 100-3000 K Temperature Range, TR-0076(6970)-4, The Aerospace Corporation, El Segundo, Calif., 31 July 1975.
8. S. J. Young, Band Model Parameters for the 4.3- μm Fundamental Band of CO_2 in the 100-3000 K Temperature Range, TR-0076(6754-03)-1, The Aerospace Corporation, El Segundo, Calif., 19 February 1976.
9. S. J. Young, "Evaluation of Nonisothermal Band Models for H_2O ," J. Quant. Spectrosc. Radiat. Transfer 18, 29-45 (1977).
10. S. J. Young, Description and Use of the Plume Radiation Code ATLES, TR-0077(2753-04)-3, The Aerospace Corporation, El Segundo, Calif., 13 May 1977.

11. A. B. Pluchino, S. S. Goldberg, J. M. Dowling and C. M. Randall, "Refractive Index Measurements of Single Micron-Sized Carbon Particles," Applied Optics 19, 3370-3372 (1980).
12. M. E. Whitson, Handbook of the Infrared Optical Properties of Al₂O₃, Carbon, MgO, and ZrO₂, TR-0075(5548)-2, The Aerospace Corporation, El Segundo, Calif., 4 June 1975.
13. T. D. McCay, U.S. Air Force Rocket Propulsion Laboratory, Edwards Air Force Base, Calif., private communication, 1980.
14. A. B. Pluchino, "Emissivity Spectra of Composite Microscopic Particles," Applied Optics, 20, 531-533 (1981).
15. G. N. Freeman, C. B. Ludwig, W. Malkmus, and R. Reed, Development and Validation of Standardized Infrared Radiation Model (SIRRM): Gas/Particle Radiation Transfer Model, AFRPL-TR-79-55, U.S. Air Force Rocket Propulsion Laboratory, Edwards Air Force Base, Calif., October 1979.
16. Particles of C, MgO, Al₂O₃, and ZrO₂ at Elevated Temperatures, AFRPL-TR-77-4, U.S. Air Force Rocket Propulsion, Edwards Air Force Base, Calif., April 1977.
17. R. Dawbarn, Aluminum Oxide Produced by Solid Rocket Motors, Proc. USAF/NASA Int. Spacecraft Contamination Conf., USAF Academy, Colorado Springs, March 1978.
18. T. D. McCay, W. C. Mundy, D. M. Mann, and G. S. Meserve, Laser Mie Scattering Measurements of Particle Size in Solid Rocket Motor Exhausts, JANNAF 12th Plume Technology Meeting, USAF Academy, Colorado Springs, 18-20 November 1980.
19. D. Deirmendjian, Electromagnetic Scattering on Spherical Polydispersions, Elsevier Publishing Co., Inc., New York, N. Y., 1969.

APPENDIX

CONVERSION BETWEEN NUMBER DENSITY, MASS LOADING, AND MOLE FRACTION

Several measures of particle loading in plumes are employed. In this appendix, the formulas are derived for conversions between loadings expressed as particle number density (cm^{-3}), mass loading (g/cm^3), and mole fraction or mole percent.

The conversion between number density and mass loading is the simplest and is independent of the plume gas properties. Let N_p be the particle number density, \bar{V} the mean volume of particles, and ρ the material density. Then, the mass loading is

$$m_p = N_p \bar{V} \rho. \quad (\text{A1})$$

For a monodisperse particle size distribution, the mean volume is simply $\bar{V} = 4\pi \bar{a}^3/3$ where \bar{a} is the particle radius. For a modified gamma distribution described by

$$f(a) = A a^\alpha e^{-\beta a^\gamma},$$

the mean volume is

$$\bar{V} = \int_0^\infty \frac{4}{3} \pi a^3 f(a) da = \frac{4\pi}{3} \frac{A}{\gamma \beta^{(\alpha+4)/\gamma}} \Gamma\left(\frac{\alpha+4}{\gamma}\right) \quad (\text{A2})$$

where Γ is the gamma function. If the loading is uniform over the cross-sectional area of the plume at a fixed axial station, Eq. (A1) can be applied directly to obtain the conversion formula. For the MSP, ALP, and one case of the RSP plume models, the loading was assumed to be uniform, and the resulting formulas are given in Table A1. The density, mass, and volume data required for the derivation are given in Table A2.

The RSP plume model was also analyzed with the Gaussian spatial distribution

$$N(r) = N_o e^{-\gamma(r/R)^2} \quad (A3)$$

$$\gamma = 9.212$$

In Eq. (A1), we assume that a given m_p is the mean value over a cross-sectional area and replace N_p on the right-hand side by its mean value over the area. In this case

$$\bar{N} = \frac{2N_o}{R^2} \int_0^R r e^{-\gamma(r/R)^2} dr = N_o \left(\frac{1 - e^{-\gamma}}{\gamma} \right) \quad (A4)$$

The conversion formula is then

$$m_p = \bar{V} \rho N_o \left(\frac{1 - e^{-\gamma}}{\gamma} \right) \quad (A5)$$

This result for the relationship between m_p and N_o for the RSP plume model with the Gaussian spatial distribution is given in Table A1.

Table A1. Particle Loading Conversion Formulas. Units are cm^{-3} for N_p or N_o , g/cm^3 for m_p , and mole fraction for c_p .

MSP Plume Model ($\text{Al}_2\text{O}_3/\text{H}_2\text{O}$)	
$c_p = \frac{1}{1 + \frac{1.16 \times 10^{-3}}{m_p}}$	$N_p = 1.17 \times 10^{12} m_p$
ALP Plume Model (C/HCl)	
$c_p = \frac{1}{1 + \frac{7.69 \times 10^{-5}}{m_p}}$	$N_p = 1.47 \times 10^{13} m_p$
RSP Plume Model ($\text{ZrO}_2/\text{H}_2\text{O}$)	
$c_p = \begin{cases} \frac{1}{1 + \frac{1.04 \times 10^{-3}}{m_p}} & \text{low-temperature} \\ \frac{1}{1 + \frac{8.49 \times 10^{-4}}{m_p}} & \text{high-temperature} \end{cases}$	
$N_p = \begin{cases} 4.34 \times 10^{10} m_p & \text{monodisperse size/uniform spatial} \\ 7.82 \times 10^{11} m_p & \text{bimodal size/uniform spatial} \end{cases}$	
$N_o = \begin{cases} 4.00 \times 10^{11} m_p & \text{monodisperse size/Gaussian spatial} \\ 7.27 \times 10^{12} m_p & \text{bimodal size/Gaussian spatial} \end{cases}$	

Table A2. Density, Mass, and Volume Parameters for Solid-Phase Species.

Species	$\rho(\text{g/cm}^3)$	w(amu)	$\bar{V}(\mu\text{m}^3)$
Al_2O_3	3.70	102	0.230
C	2.25	12	0.030
ZrO_2	5.5	123	0.230 bimodal
			4.19 monodisperse

The conversion from either particle density or mass loading to mole fraction requires the gas properties of the flow field. The number of gas molecules per unit volume for a gas at temperature T and pressure p is

$$n_g = Cp/T \quad (A6)$$

where $C = 7.34 \times 10^{21}$ molecules $K/atm\text{-}cm^3$. The number of particle molecules per unit volume is

$$n_p = \frac{N_p \bar{V} \rho}{wf} = \frac{m_p}{wf} \quad (A7)$$

where ρ is the particle mass density, w is the atomic weight of the molecules comprising the particle, and $f = 1.67 \times 10^{-24}$ g/amu. The particle mole fraction loading is thus

$$c_p = \frac{n_p}{n_p + n_g} = \frac{1}{1 + \frac{n_g wf}{m_p}} \quad (A8)$$

The measure of mole fraction loading used in this report refers to mean values over a cross-sectional area of the plume at a fixed axial station. The modification required to account for this is the replacement of n_g as given by Eq. (A6) by the average value

$$\bar{n}_g = \frac{2C}{R^2} \int_0^R \frac{p(r)}{T(r)} r dr \quad (A9)$$

For the MSP and ALP plume models considered in Section 4, pressure is constant in r and $T(r)$ is reasonably well approximated as the parabola

$$T(r) = T_o - (T_o - T_B) (r/R)^2$$

where T_o is the plume centerline temperature and T_B is the plume boundary temperature. Equation (A9) can then be integrated directly to give

$$\bar{n}_g = \frac{2Cp}{R^2} \int_0^R \frac{r dr}{T_o - (T_o - T_B)(r/R)^2} = \frac{Cp}{T_e} \quad (A10)$$

where T_e is the effective temperature

$$T_e = \frac{T_o - T_B}{\ln(T_o/T_B)} \quad (A11)$$

For the MSP model, $T_o = 1500$ K, $T_B \approx 750$ K and $T_e = 1082$ K. For the ALP model, $T_o = 2278$ K, $T_B = 1600$ K and $T_e = 1919$ K. The conversion formula resulting from these values of T_e in Eq. (A10) and the resulting \bar{n}_g in Eq. (A8) for the MSP and ALP models are given in Table A1. The same formulation was used to obtain the conversion formulas for the two RSP plume models except that \bar{n}_g was computed by numerical integration of Eq. (A9) since neither was $p(r)$ constant nor $T(r)$ representable as a parabola. The results are given in Table A1.

RESTRICTIONS

COPYRIGHT STATEMENT

AUTHORITY

APPROVED FOR
REPRODUCTION BY THE
OFFICE OF THE DIRECTOR OF
INTELLIGENCE INFORMATION
SYSTEMS AND SERVICES
IN ACCORDANCE WITH
POLICY 100-10
DATE 10/10/00

Approved for public release; distribution unlimited

FORM 1
10/00



END

DATE
FILMED

5-82

DTIC